Mass Transport Evaluation using consolidated VHF Radar and Acoustic Doppler Current Profiler Data

Thesis submitted by

Geoff Page BEng Qld

in November, 2007

for the degree of Master of Science

in the School of Mathematics, Physics and Information Technology

James Cook University

STATEMENT OF ACCESS

I, the undersigned, author of this work, understand that James Cook University will make this thesis available for use within the University Library and, via the Australian Digital Theses network, for use elsewhere.

I understand that, as an unpublished work, a thesis has significant protection under the Copyright Act and;

I do not wish to place any further restriction on access to this work.

Signature Date

STATEMENT OF SOURCES

I declare that this thesis is my own work and has not been submitted in any form for another degree or diploma at any university or other institution of tertiary education. Information derived from the published or unpublished work of others has been acknowledged in the text and a list of references is given.

____________________________ _______________

Signature Date

STATEMENT ON THE CONTRIBUTION OF OTHERS

Financial

Funding for the project was provided by the Italian Institute of Marine Science (CNR-ISMAR - Venice) and James Cook University.

Supervision

Professor Mal Heron collaborated with the design of the research and provided supervision, editorial and technical support.

Technical and Logistical

The transport and deployment of the radar stations to Venice was assisted by members of the Italian Institute of Marine Science (CNR-ISMAR - Venice) and in particular Andrea Mazzoldi and Simone Cosoli. They, together with Miro Gacic from the Italian National Institute of Oceanography and Applied Geophysics (OGS - Trieste) provided additional data from Weather Stations, Tide Gauges and the ADCP located in the channel.

Technical assistance with the testing and deployment of the PortMap radars was provided by Professor Mal Heron and Arnstein Prytz, together with Thomas Helzel and Matthias Kniephoff from Helzel Messtechnick GmbH, Germany. Technical assistance in the operation of the analysis software PMAP2DAT and in the development of additional algorithms was provided by Arnstein Prytz.

Editorial

Assistance with proof reading and editing was provided by Professor Mal Heron, Beth Heron and Naomi Page.

ACKNOWLEDGEMENTS

I would like to thank my supervisor, Professor Mal Heron for the once in a lifetime opportunity to be a part of this project. I have truly appreciated his help and encouragement, and also value his friendship.

Many thanks also go to Arnstein Prytz for his help with the radar system and data analysis algorithms. I could not comprehend how monumental the task of analysing the raw radar data would have been without the use of the PortMap analysis software.

The deployment of the PortMap radar to Venice would not have been possible without the approval by, and the assistance of the Italian Organisations, the National Institute of Oceanography and Applied Geophysics (OGS - Trieste), the Institute of Marine Science (CNR-ISMAR - Venice) and the Consortium for Co-ordination of Research Activities concerning the Venice Lagoon System (CORILA). In particular I would like to thank Andrea Mazzoldi, Simone Cosoli and Miroslav Gačić for their hospitality and assistance while we were in Venice, and for providing additional data to support the research.

Thanks also to Thomas Helzel and Matthias Kniephoff from Helzel Messtechnik GmbH for their development of the PortMap radar and their assistance in both trialling the radar and deploying the radar to Venice.

I would also like to thank my loving wife, Naomi for her patient support and encouragement throughout the time spent on this research.

Geoff Page

Abstract

In this study, a PortMap Ocean Surface Current Radar operating in the VHF band was used in conjunction with a seabed mounted Acoustic Doppler Current Profiler to obtain measurements of current velocity through the Lido channel to the Venice Lagoon. Current flow data were obtained over a six week period from both instruments. These data, together with additional data obtained from tide gauges and wind speed data from weather stations have been used to develop techniques for producing the measurements required to obtain the mass transport of water through the inlet.

The combination of data from these two different instruments was used to overcome the limitations of each technology in obtaining a complete estimation of mass transport through the inlet. Seabed mounted ADCPs only provide current measurements for a single geographical point, and are unable to measure the surface current due to side-lobe ringing within a few metres of the surface. It is for this reason that a second technology, the surface current radar was used to measure the current across the surface of the channel. For the PortMap Ocean Surface Current Radar operating in the VHF Band (152.2 MHz) this represents a depth weighted average measurement in the upper 15.7 cm of the water column.

The PortMap radar systems used in Venice produced data that were generally of a very poor signal-to-noise ratio. This was determined to be caused by a hardware fault present in the PortMap radar affecting the range resolution. Although this resulted in insufficient radar coverage of the channel required to produce an evaluation of mass transport, techniques were developed to produce the secondary data required for this purpose. The analysis software was modified to reflect the change in range resolution, enabling high resolution, short-range current vector maps to be produced for the regions surrounding each radar station.

During the deployment, a turbid water plume was observed entering on the Sabbioni side of the inlet while the tide continued to ebb on the Lido side of the inlet. The high resolution vector current maps produced were sufficient to

observe this interesting current dynamic. These measurements show that during an outgoing tide with a strong ebb tidal stream on the Lido side of the channel, water begins to flow into the channel on the Sabbioni side of the channel. This current dynamic has obvious implications for the transport of sediment from the neighbouring Cavallino beach into the inlet, and into the Venice Lagoon.

Contents

List of Tables

List of Figures

1. Introduction

To fully evaluate the mass transport (or volume transport) of a coastal ocean flow requires the measurement of current velocities throughout the horizontal and vertical dimensions of the flow. A variety of current measurement technologies exists for the measurement of ocean currents, such as Vector Averaging Current Meters, Acoustic Doppler Current Profilers, Electromagnetic Current Meters, and Ocean Surface Current Radar Systems. Each of these instruments has limitations as to its coverage of measurement, and each, used individually, cannot provide a complete set of current measurements for the purposes of estimating mass transport. With the exception of an Ocean Surface Current Radar system, these instruments obtain current measurements only at a single geographic location. Unless many sensors are deployed, single point measurements have no capability to measure currents across the width of a coastal flow or inlet, or of surface currents accurately. Although the radar system can provide current measurements over a larger geographic area, the measurements obtained are only of surface currents. In order to obtain the most complete evaluation of current velocities in an ocean flow, it is proposed that a combination of current sensing instruments be used.

The aim of this research is to establish a more complete method of evaluating mass transport through a coastal inlet using the combination of data from two of the most advanced current measurement technologies. The two instruments to be used are an Acoustic Doppler Current Profiler and the PortMap Ocean Surface Current Radar.

1.1 Overview of the Thesis

Starting with an investigation into evaluating mass transport, Chapter 2 examines the literature concerning the estimation of mass transport in a coastal flow. This includes an investigation into the measurements required for mass transport together with models for the analysis of surface boundary and bottom boundary regions of the flow. The measurement technologies considered most suitable for this purpose, the Acoustic Doppler Current Profiler and the Ocean

Surface Current Radar are also described with regards to their operation, advantages, limitations and measurement characteristics. Current research into the effective combination of ADCPs and Ocean Radar systems for the profiling of coastal currents is also presented.

Chapters 3 and 4 describe the experiment to be carried out, together with a detailed technical look at the instruments used and how they were deployed. Chapter 3 presents the design of the experiment to be carried out with a description of the site in Italy where these instruments were deployed at the Lido Channel entrance to the Venice Lagoon. The significance of why this particular site was chosen is discussed, together with an outline for the acquisition of additional data from existing local Tide, Wind and Meteorological instruments. The selection of ADCP used and the details of how it was deployed within the channel is also described. Chapter 4 presents a thorough investigation into the design and specifications of the PortMap Radar system and how the returned radio signals are analysed to produce surface current measurements using this system. Furthermore the deployment of each radar station at locations on the seawalls either side of the Lido Inlet is explained in detail.

Chapter 5 presents the data analysis methods used, and the results obtained using these methods. The chapter begins by investigating the quality of the data obtained by all the instrumentation used. This is followed by the process used to analyse raw radar data obtained by the PortMap Radar system, together with the techniques used to generate secondary current data. Two different techniques for obtaining radial current measurements from radar spectra are described together with the methods used to generate secondary current data and complete transect profiles. Following the discovery of a system fault, the final section in this chapter shows how the analysis method was modified to address this fault. The re-analysis produced higher resolution vector current maps, though at reduced range.

Chapter 6 details some key observations made during the data analysis process. The first of these was the observation of a tidal phase difference between the Sabbioni and Lido sides of the Lido Inlet. Also presented is the detection by the PortMap Radar of breaking wave backwash currents in the first range cell at the Lido station. Furthermore the effect of high velocity surface currents that could perceivably be out of the measurement range of the PortMap radar is investigated.

Chapter 7 provides an overview of the results obtained together with the major points highlighted in Chapter 6. Suggestions for how the techniques of evaluating mass transport using combined radar and ADCP data may be further developed are also given.

2. Literature Review

2.1 Mass Transport Estimation and Current Measurement

In estimating the mass transport of water, we are concerned with the total volume (or mass) of water that has passed through a given cross section area. In order to accurately estimate the mass transport of water through an estuarine inlet, the measurement and analysis of the current flow passing through the cross sectional area of the inlet are required.

2.1.1 Mass Transport Integral and Boundary Layer Velocity Distribution

The volume transport across the transect of a coastal inlet is simply the integral of the velocity over the cross sectional area. The units of this measurement are m^3/s. In order to calculate the mass transport through the same area, we integrate the product of density and velocity over this area, measured in kg/s. A further calculation regarding mass transport where the tidal current is dominant, is that of residual flow. This is obtained by averaging the current over many tidal periods. If the flow is averaged over weeks or months, residual currents in the form of wind-driven current, density-driven current or tide-induced current become apparent (Yanagi, 1999).

The difficulty in calculating mass transport with any degree of precision is in obtaining accurate knowledge of the water velocity throughout the entire cross sectional area of the inlet. River discharge, tidal forcing and wind each have an influence on the mass transport through an estuarine inlet, and the effect that these have can be influenced by bathymetry, coastal structures and sea floor characteristics. Friction between the water flow and the solid boundary of the sea floor causes the water velocity to be reduced. This velocity reduction is more pronounced near the sea bed than further up in the flow and this variation is characterised by a logarithmic boundary layer velocity profile (Dyer, 1986).

There are some variations to the profile depending on the stability of the density profile, but for a stable layer and assuming the mixing length is linear with z such that

$$l(z) = \kappa z \tag{2.1}$$

The logarithmic profile is then described by the von Karman-Prandtl equation

$$u = \frac{u*}{\kappa} \ln \frac{z}{z_0} \tag{2.2}$$

where $u*$ is the friction velocity of the flow estimated from a measured velocity profile, z is the height above the sea bed, κ is von Karman's constant (0.41) and z_0 is generally known as the roughness length and explicitly allows for varying roughness of the sea bed (Soulsby, 1983). Current velocity measurements obtained throughout a vertical column of water can be used to determine the parameters of this equation and to define the vertical structure of the current flow. In shallow water, this boundary layer velocity profile may be present across the entire depth of water or it may be limited by density layers, temperature layers or wind-driven currents within the water column.

2.1.2 Enhanced Surface Current Shear - Wind Effects and Density Layers

The effect of wind blowing across a surface of water causes a wind stress on the surface layer which in turn causes wind driven surface currents to form (Yanagi, 1999). The wind induced surface current causes shear stress on lower layers of water. This creates a logarithmic boundary layer velocity profile similar to that of the sea bed boundary layer. In an investigation into wind-driven surface currents, Fernandez et al (1996) characterised this by the following equation :-

$$\frac{U_s - U_x(z)}{u_w*} = \frac{1}{\kappa} \ln \frac{z}{z_0} + 8.5 \tag{2.3}$$

where $U_x(z)$ is the velocity of the water at some depth, z, U_s is the value of the current at the surface, u_w* is the friction velocity at the surface of the water, κ is von Karman's constant, and z_0 is the roughness length. In similarity to the sea-bed boundary layer profile, accurate velocity measurements of the surface current and within deeper layers are required to determine the parameters u_w*

and z_0. The constant given as 8.5 depends on drag coefficient, and is also determined experimentally for a given situation.

Density layers can also affect the current structure within the vertical column of water. River water entering an estuary can partially mix with the salt water and will eventually flow out to the open sea in a less dense top layer of water. Sea water will also flow into the estuary below this upper layer to balance this circulation. Although river flow into the estuary tends to reduce the salinity, a corresponding inflow of sea water tends to balance this to a point of equilibrium (Pickard, 1990). Currents in layers of unlike density will differ as a result of this process, and their presence will have some effect on the logarithmic boundary velocity profiles from the sea bed and the sea surface.

If any of these dynamic processes in the estuarine environment are to be clearly accounted for in the calculation of mass transport of water through an inlet, scientific tools are required to accurately measure the current velocity at points throughout the entire cross sectional area of the inlet. Acoustic Doppler Current Meters and Ocean Surface Current Radar systems are considered the two most modern and capable technologies that are available for this purpose.

2.2 Acoustic Doppler Current Meters

An Acoustic Doppler Current Profiler (ADCP) is an instrument for measuring current velocity that uses acoustic pulses and the Doppler effect to obtain velocity measurements throughout a column of water. This instrument was originally adapted from commercial speed logs used in ships as these tracked the ship’s speed over ground or speed through the water using sonar technology. The ADCP was developed from this sonar technology and was first commercially available in the latter half of the 1970s (Rowe and Young, 1979). The first commercially available ADCPs were designed to measure water velocity with greater accuracy and to allow the current to be measured in cells throughout the vertical column of water. Modern ADCPs are available in a variety of operating frequencies depending on operating circumstances and can be ship based, surface mounted or bottom mounted. The use of ADCPs in the measurement of geophysical current flow is now well established (e.g., Lee, 2002; Wewetzer, 1999). Research into the extraction of wave, wind and sediment concentration data from ADCP measurements has also been investigated by various researchers (e.g., Kostaschuk, 2005; Zedel, 1995; Schott, 1989). Of primary importance, the ADCP is able to provide measurements of the vertical structure of current flow. This structure can be clearly seen in the sequence of measurements depicted in Figure 2.1 from a study undertaken by Lueck and Lu (1997). This study investigated the logarithmic boundary layer in a tidal channel.

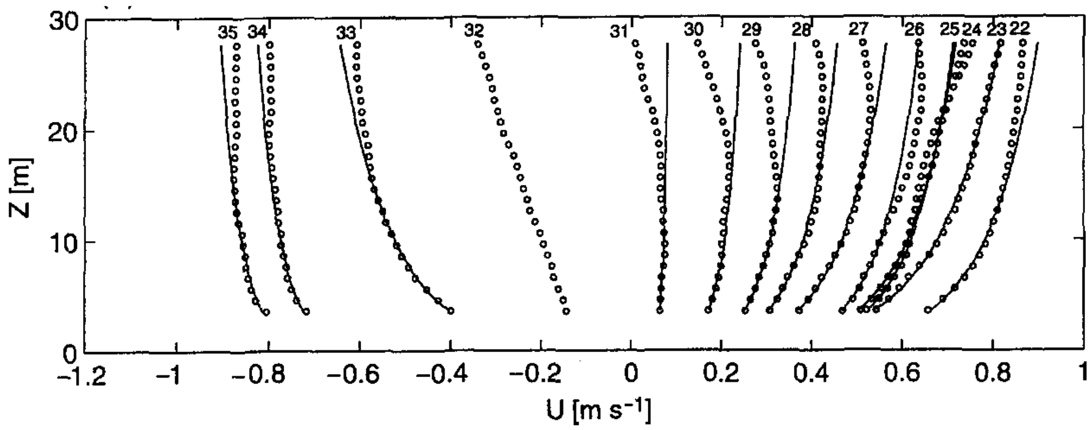

Figure 2.1 - Logarithmic Profiles obtained from ADCP Measurements
Sequence numbers identify each sequential 20 minute sampling period.
o - ADCP Measurement, Solid line - logarithmic profile model fit
(Lueck and Lu, 1997)

2.2.1 Principles of Operation

The Acoustic Doppler Current Profiler uses the Doppler effect to determine the velocity of suspended particles such as plankton and sediment in the water column. Critical assumptions in the use of ADCPs is that the scattering particles are presumed to be travelling at the same average velocity as the surrounding water and that the water velocity is constant within horizontal layers. The ADCP measures the velocity of the scattering particles by transmitting acoustic pulses and then analysing the signals of the subsequent reflections from these particles.

Velocity

The sound waves reflected from the scatterers are Doppler shifted in frequency relative to the particles' velocities. The velocity of the water can thus be determined from the following formula describing the Doppler effect, which describes the shift in sound frequency received from a moving scatterer:

$$F_d = 2 * F_s(V/c) \qquad (2.4)$$

where V is the relative velocity of the source and receiver, F_d is the resultant Doppler shift, F_s is the frequency of the transmitted pulse and c is the speed of sound.

Velocity Direction

To enable the instrument to determine the velocity of the water in three dimensions, three (120° horizontal spacing) or four (90° horizontal spacing) orthogonal transducers and corresponding sound beams are used to resolve measurements in all directions of motion. These beams are typically aligned between 20° to 30° from the vertical. If four orthogonal transducers are used, the fourth redundant measurement is used to produce a measurement of error velocity. The average of the vertical velocity from two opposing beam pairs is used to calculate the vertical water velocity. The difference between the two opposing beam pairs is known as the error velocity measurement and is used to investigate the error of the measurements obtained.

Range

In order to produce a vertical profile of current velocities, the water column under investigation is broken into regularly spaced depth cells, called bins. Time based range-gating is used to separate the returned echo data into their bins related to their distance from the instrument.

2.2.2 Advantages, Limitations and Sources of Error

The variety of deployment methods is a distinct advantage of the ADCP, as is their ability to provide multiple points of measurement within the water column.

Commonly deployed on the sea bed, moored at the surface or moored at some depth in between, ADCPs can be self-contained or directly linked to recording stations to monitor data in real-time. When self-contained, ADCPs are limited in their deployment period by battery capacity and data storage capacity. If they are linked to a recording station to overcome these issues or to provide real-time data, the duration of their deployment is then limited by the growth of fouling marine organisms (barnacles) on the transducers. ADCP mountings within a frame on the sea bed must be carefully designed to avoid obstruction of trawling vessels which can result in corruption of data or loss of instruments (Dessureault, 1991). If it is not possible to deploy a fixed ADCP in a given situation for an extended time, advances in Global Positioning Systems (GPS) and sea floor tracking have also allowed their accurate use aboard boats. This enables current profile measurements to be made along coastal transects, such as in the study conducted by Lee (2002). Similarly, a towed, surface-mounted ADCP was used by Cheng and Gartner (2003) to profile cross-sectional river flows.

Unlike single point measurement devices such as mechanical rotors or electromagnetic sensors, ADCPs have the advantage that they are able to obtain current measurements throughout the vertical column of water (Lane, 1999). The water column is divided into depth cells (or bins) with weighted average measurements obtained throughout the cell. This weighted average technique places greater importance on the measurements obtained closer to the centre of the depth bin than those toward the edges.

Unfortunately, ADCPs have the disadvantage that the results become unreliable at measurement boundaries such as the sea surface or sea bed (depending on deployment orientation). This is due to the contamination of faint signals from particle echoes by the stronger sound reflections from these reflective boundaries. This is known as side-lobe contamination, as it is the transmission and reception by the transducer's side-lobes that gives the acoustic reflections from the boundaries. The RD Instruments, Principles of Operation Primer (1996) details the -3dB beamwidth of a typical 1200 kHz ADCP to be 1.4˚, with a single direction side-lobe level of -42dB at approximately 30˚ from the axis. For an ADCP with beam angles of 30˚ from the vertical, this side-lobe is presented directly toward the surface or bottom boundary, as can be seen in Figure 2.2.

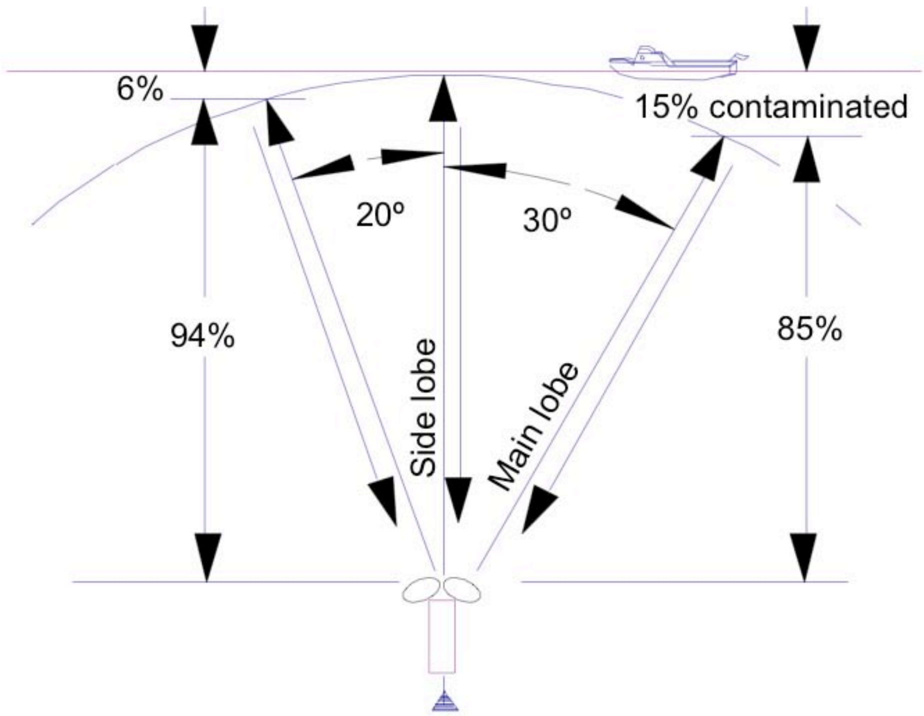

Figure 2.2 - The relationship between ADCP transducer beam angle and the thickness of the contaminated layer at the surface.
(RD Instruments, Principles of Operation Primer, 1996)

Any range with side-lobes presented to a boundary will cause measurements to be biased towards zero. This effect is well documented by Apell (1991) where a study investigated the use of various baffles to reduce unwanted effects from side-lobe contamination in ADCPs. The usable range of an ADCP deployment is characterised by the following equation where R_{max} is the usable range, D is the depth of deployment and θ is the beam angle relative to the vertical (RD Instruments, Principles of Operation Primer, 1996).

$$R_{max} = D\cos(\theta) \tag{2.5}$$

In a typical bottom mounted ADCP deployment in 20 m of water with 20° beams, this will result in side-lobe contamination in the top 1.21 m of water. Changes in depth and sea surface roughness caused by tidal variation and waves can cause further contamination of data to a bottom mounted ADCP looking toward the surface. Similarly, a surface or ship-mounted ADCP over rough seabed topography can produce the contamination of data for some of the lowest bins (Kostaschuk et al., 2005). Other causes of data contamination or discontinuities can exist in tidal regions where data bins are periodically out of the water. A new instrument in the measurement of river flow, a surface mounted BoogieDopp Current Profiler has been used in a study by Cheng and Gartner (2003) to provide current profiling to within 11cm of the surface. This particular instrument seemed to overcome some of the previous limitations in measuring velocities close to the surface in rivers.

Contamination of measurements can also be caused by acoustic ringing that occurs following the transmission of a sound pulse by the instrument. The source of this acoustic ringing can be attributed to receiving electronics, protective covers, bed frames or ships' hulls and can generate a zero bias of measurements, as the received signal is not Doppler shifted. Extensive errors in measurements in the first data bin close to the sea floor were discarded in a study by Tang (1994) due to ringing of a protective cover. It was also discovered in the subsequent data analysis that data in bins 2 and 3 were of lowered accuracy for this same reason. Also in this study by Tang, the furthest bin within the usable range was rejected due to the reflection of side-lobe energy from the bottom of waves.

Aside from the above limitations leading to the severe corruption of data, error and uncertainties exist in the recorded data due to random error and measurement bias. Bias is typically found to be less than 10^{-2} $m.s^{-1}$ and is dependent on many environmental factors and internal operating specifications (RD Instruments, Principles of Operation Primer, 1996). The magnitude of random error depends on internal attributes such as sound frequency, bin size and beam pattern or it may be influenced by environmental factors such as turbulence, internal waves or from movement of the ADCP itself. In modern broadband ADCPs, random error can be reduced by averaging the returned data over a number of ping cycles to the point where its effect becomes less than the effect of measurement bias. The amount of random error can be estimated by calculating the standard deviation of the velocity error measurement, obtained through the use of four measuring beams. The velocity error measurement is also used to reliably test whether the water velocity is constant within horizontal layers, i.e. is of horizontal homogeneity. In-homogeneous flows tend to cause large error velocities and unreliable data. Turbulent coastal flows do not generally satisfy the assumption of homogeneous flow as the velocity is never homogenous over the span of the beams, and further data processing is required to obtain useful velocity profiles (Lu and Lueck, 1999).

Errors can also be caused by the lack of sufficient reflecting particles in the water. Lane (1999) found that these can occur on a seasonal time scale where there are not enough biological scatterers present in portions of the water column to obtain accurate measurements.

2.2.3 Obtainable Measurements and their Characteristics

The primary results obtained from ADCPs are temporally averaged velocity measurements that are weighted over a range cell for various points throughout the column of water. Parameters obtained from these ADCP measurements are those relating to the distribution of velocity within this vertical column. Mass transport can be directly estimated from such velocity distributions and can be related to logarithmic profiles to obtain boundary layer parameters (Smith, 2002; and Lueck and Lu ,1997). Other research using vessel mounted ADCPs to investigate mean river flows has suggested that average velocities and turbulence intensities can also be accurately estimated (Muste, 2004).

It has been shown that surface parameters such as wave particle velocity (Apell, 1991) and significant wave height (Rowsell, 2002) can be determined from ADCP data. Additionally, bottom tracking capabilities and returned back-scatter signal strength have been used in sediment dynamics studies to estimate parameters such as bed load and suspended load (Kostaschuk, 2005). Furthermore, Schott (1989) reported a correlation between returned echo amplitude from the surface and wind strength. This has again been revisited by studies in monitoring sea surface conditions using ADCPs by Visbeck and Fischer (1995) and Zedel et al. (1995).

2.2.4 Application to a coastal inlet for the estimation of mass transport

For an ADCP instrument to be deployed over a month long time period on the sea bed of a shallow channel, it is of key concern how the instrument should be best configured to give the most accurate data over the greatest range of depth. Primary factors affecting the usable range of measurements are ringing distance and the amount of side-lobe contamination from boundary layers. The effect of ringing is reduced by the blanking of measurements in short ranges near to the instrument. To reduce the ringing distance to a minimum proportion of the depth in a shallow channel, a ping frequency of 600 kHz or 1200 kHz should be used (Table 1, RD Instruments, Principles of Operation Primer, 1996). To reduce the amount of contamination from side-lobes an ADCP with beam angles of 20˚ should be used . RD Instruments specifies the 1200 kHz ADCP as having a range of 25 m and power consumption of 15 W (Table 2, RD Instruments, Principles of Operation Primer, 1996). Studies of currents in shallow regions to have used an ADCP operating at a frequency of 1200 kHz and 20˚ beam angles include those performed by Cheng et al. (2003) and Rowsell et al. (2002).

Frequency	Ringing distance
75 kHz	6 m
150 kHz	4 m
300 kHz	2 m
600 kHz	1 m
1200 kHz	0.5 m

Table 1.1 Typical ringing times expressed as distances from the transducers. Speed of sound approx. 1467 $m.s^{-1}$ (at 4˚C, 35‰ salinity and at sea level) (RD Instruments, Principles of Operation Primer, 1996)

Frequency (kHz)	α(dB/m)	Nominal Range (m)	@ Power (W)
76.8	0.022-0.028	700	250
153.6	0.039-0.050	400	250
307.2	0.062-0.084	120	80
614.4	0.14-0.20	60	30
1228.8	0.44-0.66	25	15

Table 1.2 Sound absorption (At 4˚C, 35‰ salinity and at sea level) and nominal profiling range of a Broadband ADCP. The transmit power listed is the maximum power that can be transmitted subject to limitations caused by shock formation. (RD Instruments, Principles of Operation Primer, 1996)

2.3 VHF / HF Coastal Ocean Surface Current Radar

Coastal Radar systems provide a remote sensing alternative to the measurement of ocean surface currents. Unlike in-situ current meters such as ADCPs, Coastal Radar can provide vector maps representing surface currents over large areas of ocean, or high spatial resolution current mapping over smaller areas such as coastal inlets or channels. Coastal Radar systems exist that operate in the High Frequency (HF) band between 3 - 30 MHz and the Very High Frequency (VHF) band between 30 - 300 Mhz.

2.3.1 Principles of Operation

Doppler Radar Systems were originally developed for military use as a means of aircraft detection whereby a transmitted electromagnetic signal would be reflected by a moving aircraft. This reflected radar signal would be Doppler shifted in frequency relative to the radial velocity of the aircraft. Although not clearly understood at the time, high levels of noise or back-scatter related to sea state were often observed with the use of these systems over coastal seas such as the English Channel. Structure in this "sea clutter" was first identified and characterised by Crombie (1955) where he correctly related this back-scatter to ocean waves of half the wavelength of the transmitted radar signal. His analysis of the returned spectrum identified a Doppler shift related to the phase velocity of these waves toward or away from the observing radar. Theoretical first order verification of this observed back-scatter determined to be "Bragg Scatter" was later performed by Barrick (1972a) who further proposed its usefulness in the implementation of wave sensing and sea state sensing (Barrick et al., 1972b). The application of Doppler radar to the measurement of surface current was not realised until Stewart and Joy (1974) detailed a method of extracting surface current data from the observed back-scatter spectrum. From a comparison between observed phase velocity of the scattering waves and the theoretical phase velocity these deep water waves would have in still water, they were able to deduce the underlying surface current at the observed point. Experimental comparisons with drifting drogues verified the accuracies of their results to within a few centimetres per second. This technique of measuring surface current was further developed by Barrick (1977) in the use of two observing High Frequency (HF) radar units to produce current vector maps covering an area of over 2000 km^2 and to a distance 70 km offshore. As each individual radar unit provides only the radial component of the current velocity toward or away from the observing radar, two radar stations located a few tens of kilometres apart are used to resolve the two-dimensional current velocity vector. His use of this technique provided two dimensional surface current maps for the region under investigation.

Radial Component of Current Velocity

As described earlier, the total Doppler shift of the observed back-scatter is a result of the Doppler shift from the scattering waves' phase velocity and the underlying surface current. As detailed by Barrick et al. (1977), this total Doppler shift, f_D can be represented as the sum of a component due to Bragg wave phase velocity, f_B and an additional component,
Δf as follows :-

$$f_D = f_B + \Delta f \tag{2.6}$$

$$f_D = \pm\sqrt{\frac{gf_0}{\pi c}} - 2\ f_0\frac{v}{c} \tag{2.7}$$

where g is the gravitational constant of acceleration, f_0 is the operating frequency of the radar, c is the vacuum speed of electromagnetic waves and v represents the component of the surface layer water velocity parallel to the direction of the radar beam. In Figure 2.3 presented by Heron and Prytz (2003), the recorded back-scatter spectrum reveals two first-order spectral peaks, positively and negatively Doppler shifted from the radar frequency. Positively and negatively shifted spectral lines are observed due to scattering from waves propagating toward and away from the observing radar. An additional offset due to the surface current component, Δf *(df)* is seen to deflect the spectral peaks from the theoretical Doppler shift due to Bragg waves alone (positions of the dashed lines).

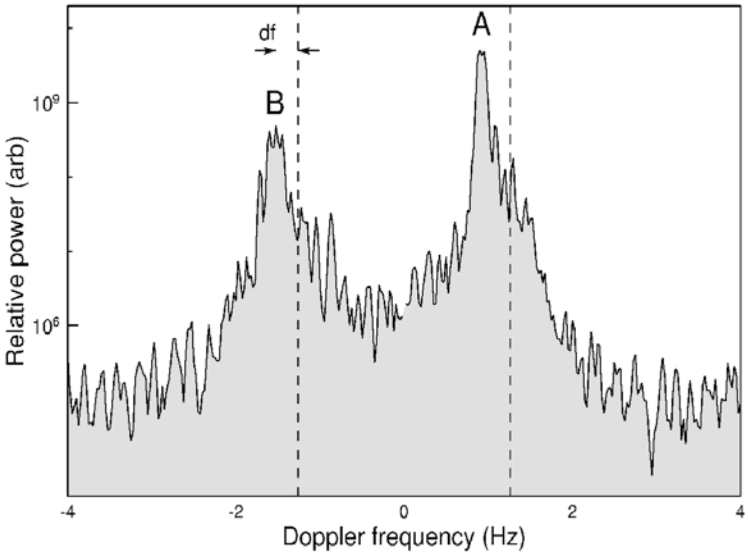

Figure 2.3 - Typical Spectrum for the VHF COSRAD Radar, Heron and Prytz (2003)

Range

In common with all radar operations, the scattering source or portion of ocean is identified by determining its azimuth (or direction) and distance from the observing station. Two main techniques exist among commercial coastal radar systems for determining the position of this target cell. Common to both techniques is the use of the properties of electromagnetic propagation speed to determine the range to target.

Range to target cell is essentially determined using the knowledge of the phase velocity of the transmitted electromagnetic waves. It is simply characterised by the equation :-

$$Range = \frac{c\ t}{2} \qquad (2.8)$$

Where *c* is the velocity of electromagnetic waves and *t* is the propagation delay from the time of transmission to the time of reception.

The first ocean radar system to enter commercial use, the CODAR (Coastal Ocean Dynamics Application Radar) was originally developed at the National Oceanic and Atmospheric Administration (NOAA) by a team led by Barrick (1977). Of simple design, this system transmitted 20 µs long radar pulses and simply determined the range to target cell by time gating the received signals.

The range resolution of this system is proportional to the duration of the transmitted pulse. The disadvantages of this technique are the high peak transmission power required and a blind range in front of the radar related to the length of the transmitted bursts (Gurgel, 1999a).

A continuously transmitting radar system such as the Wellen Radar (WERA) described by Gurgel (1999a) uses a frequency modulated transmitted signal to determine the range to target cell. As described by Gurgel (1999a), Frequency Modulated Continuous Wave (FMCW) systems of this kind vary the transmitted frequency linearly over a period T, and use this transmitted sweep (or chirp) to phase coherently demodulate the returned radar echos. The range resolution of the radar is determined by the bandwidth, *b* of the frequency chirp over the time period, *T*. As shown by Gurgel (1999a), where the resolution of frequency is Δf, the range resolution is determined thus :-

$$\Delta\tau = \frac{T\Delta f}{b} = \frac{1}{b}\ , \quad \Delta r = \frac{c}{2}\Delta\tau = \frac{c}{2b} \qquad (2.9)$$

Because of this, these systems have the ability to select a desired range resolution by varying the bandwidth of the chirp. Other advantages of the FMCW systems are that they are more robust against radio interference (Gurgel, 1999b) and that there is no blind range in front of the radar. They do however require that the transmitter and receiver possess extremely high dynamic range and linearity, and also require that the transmit and receive antennae be placed to minimise coupling between them.

Direction

As with the determination of range to the cell, two different methods exist for determining the azimuth (direction) of the target cell. These are, direction finding techniques and beam forming techniques.

The original CODAR system (Barrick, 1977) and its commercial successor, the Seasonde as evaluated by Emery (2004), both use direction finding techniques to determine the azimuth to the target. The CODAR system developed by Barrick, initially used a phase direction finding technique using signals obtained from a linear three element antenna array. This was later modified to a four element configuration (arranged in a square) to enable the determination of azimuth from all directions.

The Seasonde system uses the directional characteristics of a pair of crossed loop antennas (representing the x and y axis) and a monopole antenna (for normalisation of the loops) together with the MUSIC (Multiple Signal Classification) direction finding algorithm to locate the angular origin of received signals. As reported by Emery (2004) this is a relatively robust system. However, gaps can appear in the coverage which may result from the direction finding technique by the MUSIC algorithm. This is most likely because the technique or algorithm is unable to resolve more than two signals, at all times within a given range anulus. The main advantage of the Seasonde system is the small physical space required for the placement of its antennas.

As used by the WERA system (Gurgel, 1999a), beam-forming techniques produce a relatively narrow, steerable radar beam from a linear array of antennae arranged broadside to the region under investigation. The process of beam-forming is achieved in the time domain by summing the weighted and phase shifted signals from each antenna. Weighting reduces the side-lobes of the antenna array whereas the beam is steered through phase shifting. A WERA system operating in the High-Frequency Band will typically use 16 antennae in an array, with optimum spacing between individual antennae of a little less than half the radar wavelength (0.45 λ). This will achieve a beamwidth of approximately λ/D radians where λ is the radar wavelength and D is the overall length of the array.

2.3.2 Advantages, Limitations and Sources of Error

The ability of Ocean Surface Radar systems to provide high resolution spatial and temporal measurements over a wide surface area is seen to be their greatest advantage over single point current meters. These systems make it possible to obtain finely detailed information about the structure of surface currents, making it possible to identify eddies and fronts (Lane, 1999). These structures cannot be measured with the same time resolution by any other means. The radar systems are also safer to deploy than moored current meters, especially in areas where it may be hazardous to lay moorings or in channels with heavy ship traffic. Their deployment also does not require the use of an expensive research vessel. Other advantages are that they can be remotely monitored or provide real-time data via communication links, and that they are not generally affected by poor weather or high sea conditions.

The limitation of usable range is dependant on the amount of attenuation between transmission, reflection and return of the propagating radio wave (Gurgel, 1999b). The amount of signal attenuation and the amount of signal reflection from scatterers determines the level of signal return achieved. This, coupled with the effects of atmospheric noise and other external short-range and long-range radio interference determine the Signal-to-Noise Ratio (SNR) of the system. This Signal-to-Noise Ratio is a primary indicator in determining the usable range of the system and the amount of error. As presented by Gurgel (1999b) on the physical limitations of HF radar systems, the attenuation of the propagating radar wave depends on frequency, the salinity of the sea surface, sea surface roughness and distance. Higher frequencies are attenuated more than lower frequencies. Lower salinity also leads to higher attenuation. Since interference is more prevalent while using lower HF frequencies, a trade-off is often involved in choosing an operating frequency to carefully maximise SNR and therefore range, Barrick (1977). Similarly, the amount of returned echo is dependant on the presence of significant scattering waves having a wavelength of half the radar. Barrick (1977) selected frequencies within a range of 25 MHz to 26 MHz as these were rarely affected by ionospherically propagated interference and were back-scattered from often present ocean waves of wavelength, 6 m. Gurgel (1999b) states that although VHF frequencies are highly attenuated and possess very limited working ranges, they are not affected by interference from long-range radio sources, only local sources. Working with a radar frequency of 152.2 MHz, Heron and Prytz (2003) have successfully used a VHF radar system to obtain high spatial resolution (100 m) current maps to a limited range of 1.5 km. This has proven highly successful in the investigation of near shore ocean surface currents.

Signal-to-Noise Ratio is also affected by sea state (Paduan, 1996) and is reportedly related to the accuracy of measurements where it causes spectral line broadening (Graber, 1997). The addition of noise and the broadening of the spectral line has been seen in some systems to make it difficult to determine the centre of the spectral peak (Graber, 1997). The study in obtaining current measurements in a surf break zone using a VHF Radar by Heron and Prytz (2003) determined that although the location of the spectral peak may be degraded by line-broadening, it was still possible to accurately determine the spectral peak and its frequency under these conditions. Subsequently, the broadening of peaks did not significantly affect the ability of the VHF system to measure surface currents in these conditions.

Other errors may exist as a result of beam forming misalignment, spatial inaccuracies and the contamination from side-lobes (Fernandez, 1996).

Further limitations in the use of HF / VHF Ocean Radar systems are related to the physical aspects of deploying the observing stations. Particularly with HF WERA Systems, the siting of large antenna arrays can be limiting in the choice of deployment sites. Other factors to consider for all radar systems is the supply of power and communications requirements for the deployment site, and the licensing and allocation of operating frequencies and bandwidth.

2.3.3 Obtainable Measurements and their Characteristics

As already described, the main product obtained from an Ocean Surface Radar is a high-resolution vector map of surface current velocities for areas of the ocean surface. The Ocean Surface Radar is unique in this regard. Although well designed surface drifters can be used to accurately measure surface currents they are very limited in their space scales and time-scale sampling (Paduan, 1996). Throughout the development of the Ocean Radar there have been numerous comparisons of HF Radar measurements with established single point methods of current measurements, such as those performed by Teague (2001), Graber (1997), Stewart and Joy (1974) and Barrick (1977). Graber (1997) specifically identifies a single point measurement as representing a fixed-length temporal average at a point, while a radar observation represents a short-duration spatial average of a fixed area.

The radar measurements observed at the centre of an observation cell are in fact spatially averaged current measurements for this cell. This is due to the back-scatter and therefore Doppler shift resulting from the average surface current within the entire range cell. Variability of the measurements obtained can also be reduced by averaging over longer time periods (Emery, 2004). Another aspect of the measurements obtained is that they represent a weighted average over a depth from the surface. As investigated by Stewart and Joy (1974), this depth is dependent upon the radar frequency used. The scattering ocean waves corresponding to the radar wavelength are affected by a current to a depth proportional to their wavelength. Assuming a linear current profile near the surface, it has been defined thus :-

$$\text{Effective Depth} = \frac{\lambda}{4\pi} = \frac{1}{2k} \qquad (2.10)$$

where λ is the radar wavelength and k is the radar wavenumber. This was found to be consistent with an experiment using Multifrequency Coastal Radar (MCR) by Teague (2001). However, better agreement was suggested in some situations using *Effective Depth* $= 1.4\,(2k)^{-1}$. In this study by Teague (2001) and an earlier study by Vesecky and Teague et al. (1998) it was shown that multifrequency radar provided the ability to observe near-surface currents at varying depths. With the range of frequencies used, current measurements were obtained for effective depths of 0.5 m to 2.5 m, though these were insufficient to generate surface layer current velocity profiles. The combination of results from the Multifrequency Radar and ADCP measurements for bins 2 - 14 m below the surface did however provide a more complete evaluation of the vertical structure within the water column.

2.3.4 Application to a coastal inlet for the estimation of mass transport

Coastal Ocean Radar using HF Frequencies to map current velocities off coastal regions to distances of up to 80 km offshore has been well documented by various authors such as Paduan (1996), Fernandez (1996) and Barrick (1974). The use of these systems has also been used in investigating large scale coastal channels such as the North Channel between England and Ireland (Knight and Howarth, 1999). While the use of HF Coastal Ocean Radar is quite well developed, the application of this technology to small scale coastal inlets and channels of the order a few kilometres across is not well researched. To provide adequate range resolution for such an application, the use of VHF frequencies is required. Although such VHF frequencies are highly attenuated and subsequently systems have very limited ranges of only a few kilometres, this is sufficient to map the currents in ports and coastal inlets. As mentioned earlier, the COSRAD system used by Heron and Prytz (2003) provided a range resolution of 100 m over a limited range of 1.5 km. This system provided high spatial resolution current measurements for a near-shore region. According to the effective depth analysis of Stewart and Joy (1974), these results would have represented a depth weighted average measurement of the upper 15.7 cm of the water column.

Other important aspects of the deployment of Coastal Ocean Radars are the physical locations of the observing stations. With only a limited system range and a specific region of investigation, the positioning of the radar systems is critical to obtaining the required measurements. The Radar Observing Stations must be located to ensure that the angle of intersection of both radar station beams is at least 30° for the region of interest (Graber, 1997). Regions with any intersection angle less than 30° are generally discarded because the errors involved in computing vector current become unacceptable.

2.4 Measuring the complete velocity profile

2.4.1 The need for a combination of measurement systems

Each of the measurement technologies presented in the previous two sections have individual shortcomings in their ability to profile the entire cross-sectional area of a coastal inlet. An ADCP mounted on the sea bed is able to provide accurate velocity measurements throughout most of the vertical water column but only for a single geographical point. It also lacks the ability to accurately profile currents close to the surface. Conversely, an Ocean Current Surface Radar operating at a fixed frequency cannot provide current measurements for anything except the surface layer. It can, however, provide these measurements across a wide area to a high degree of accuracy and high spatial resolution. A combination of these two technologies will extend the measurements of water current velocities across an Inlet.

Both the Broadband ADCP and Ocean Radar current measurement technologies have developed to the point where they are accepted and valued as useful tools for coastal oceanographic purposes (Graber et al, 1997 and Rowsell, 2002). In many studies using both these tools, the combined use has been limited to verifying the data acquired by HF Radar systems (Teague, 2001; Lane, 1999 and Graber et al, 1997). Now that the Ocean Radar technology is established, its use in conjunction with ADCP data should be able to provide a more detailed analysis in applications of coastal oceanographic research.

2.4.2 Examples of the use of combined measurement strategies

There is a very limited number of research activities where both Acoustic Doppler Current Profilers and Ocean Surface Current Radars have been used in an integrated measurement approach. A single study of particular key interest was performed by Howarth et al. (1995) and Knight et al. (1999). This experiment referred to in both publications investigated the net flow through the North Channel between Scotland and Ireland using measurements obtained from both ADCPs and the Ocean Surface Current Radar (OSCR) HF Radar system. The ADCP was mounted on the sea bed in a low-profile frame at position E as shown in Figure 2.4, whereas the two Ocean Radar observing stations were positioned at Portpatrick and Crammag Head. The 150 kHz, 20° ADCP was deployed on the sea bed at a depth of 142 m and provided current measurements from 12.5 m above the sea bed to within 15 m of the surface. The OSCR Radar system provided surface current measurements across the entire channel except for an area of measurements close to the Irish Coast, which were beyond the limit of the system's usable range. The data from this area were discarded due to poor signal return and interference. However, they were not considered vital in the calculation of mass transport due to the shallow depth in this region.

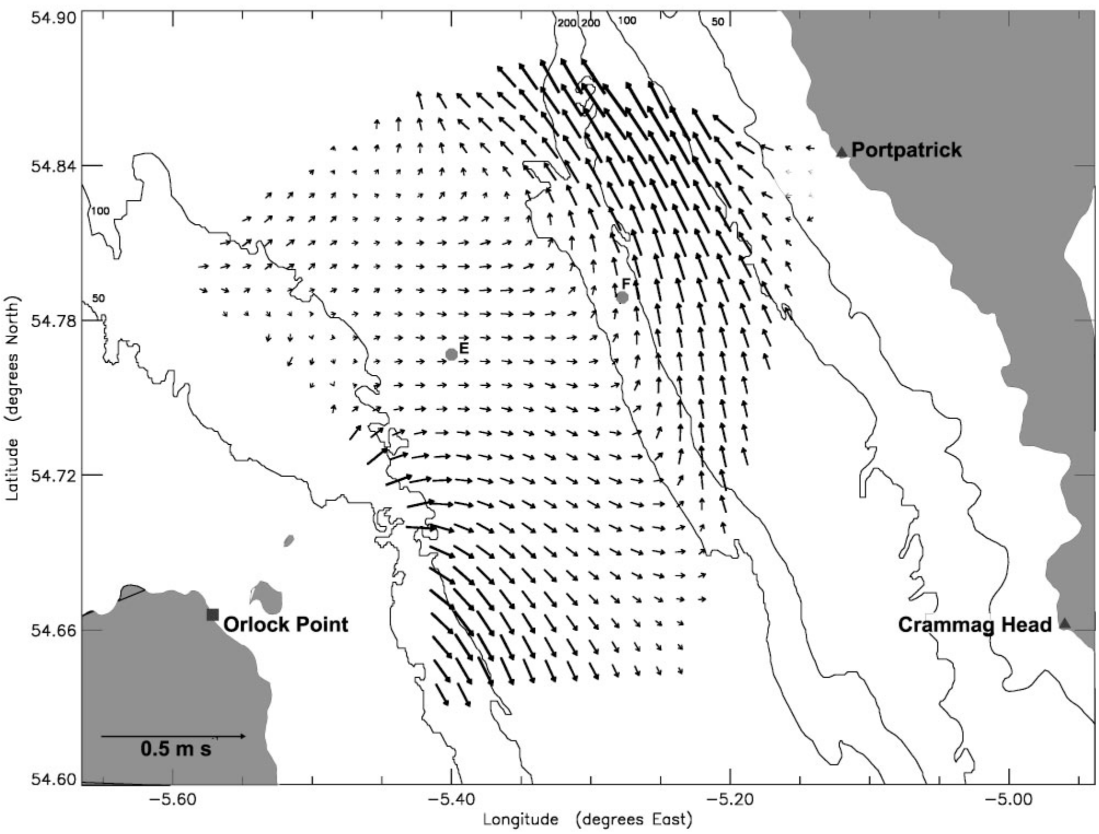

Figure 2.4 - Surface mean flows obtained from OSCR HF Radar
E - Seabed Mounted ADCP
F - S4 and RCM-7 Current meter mooring
▲ - OSCR Radar Stations

(Knight et al. ,1999)

The study of the North Channel focused on the residual flow caused by atmospheric pressure-systems and wind-stress on the ocean surface. Once the tidal effects were removed, the analysis revealed quite complex residual flows. With the use of a simple residual current and wind stress correlation model it was suggested that large wind stresses were significant for residual flow. It was discovered that even on daily time scales, wind stresses could induce southward flows as well as northward flows within the channel.

A strong variation in the surface current was observed across the channel with complex flows present on the western side of the channel and strong currents close to the Scottish Coast directed towards the North-West. The ADCP data also showed complex current patterns within the vertical structure. At the ADCP Point E, a mean current near the sea bed was directed North-Westerly out of the Irish Sea while near the surface the current was directed into the Irish Sea.

Through the combined use of ADCPs and Ocean Radar systems, this study was able to provide a detailed investigation into the complex effects of wind stress on residual currents. In particular, this provided the means to estimate the mass transport taking into account both the horizontal and vertical variations of the current flow through the channel. The use of a single measurement technology alone would not have revealed the complexity of these currents in the North Channel.

2.5 Conclusion

The estimation of mass transport relies on successfully obtaining current measurements throughout the entire cross-sectional area of the flow, or transect of investigation. Measurements of both surface current and currents throughout a depth of water are not possible using one measurement tool alone. It has been shown that Acoustic Doppler Current Profilers provide accurate current flow measurements throughout the vertical column of water at a single point. This is useful in deriving vertical velocity distribution profiles near to the sea bed. Due to the inability of a sea bed mounted ADCP to profile currents in the surface layer plus its limitation to a single geographical point, an additional instrument such as an Ocean Surface Current Radar is required to provide surface current measurements.

Although the combined use of ADCPs and HF Ocean Radar systems has previously been used to determine mass transport through the North Channel between Ireland and Scotland by Howarth and Knight et al. (1995 and 1999), generally this technique remains undeveloped. To date there have been no publications regarding the use of both ADCPs and VHF Ocean Radars to evaluate mass transport through shallow coastal inlets. It is apparent that this area of knowledge would be significantly added to by a study involving the deployment of Acoustic Doppler Current Profilers and a VHF Ocean Radar system to evaluate mass transport and residual currents.

3 Research Design

3.1 Introduction

An experiment was proposed to accurately measure current velocities through a shallow coastal inlet using a current measuring scheme similar to those discussed in the previous chapter. An Acoustic Doppler Current Profiler was used together with the PortMap Surface Current Radar operating in the VHF band. It is expected that the combination of data from these two technologies would provide the most comprehensive means for estimating mass transport through the channel.

This research was conducted as part of an international project involving a partnership between James Cook University, Queensland Science and Engineering Consultants Pty. Ltd. (QSEC), and a greater consortium consisting of the Italian Organisations, the Italian National Institute of Oceanography and Applied Geophysics (OGS - Trieste), the Italian Institute of Marine Science (CNR-ISMAR - Venice) and the Consortium for Co-ordination of Research Activities concerning the Venice Lagoon System (CORILA). The main purpose of this collaborative project was to deploy the PortMap VHF Radar system to observe the surface currents in the Lido Channel entrance to the Venice Lagoon. This surface current data is to supplement the data from existing instruments already deployed to observe the current dynamics within the Lido channel. This will complement research already being undertaken by the Italian organisations regarding marine coastal circulation and water exchanges between the Venice Lagoon and the open sea. The combination of these data will provide detail of the surface current structure that is not possible with the existing instrumentation. The various sources of data and their contributors for the project are presented in Table 3.1.

Instrument	Contributor
Seabed ADCP - Lido Channel	OGS - Trieste, Italy
Tide Gauge - Lido	CNR-ISMAR - Venice, Italy
Meteorology Station Data	CNR-ISMAR - Venice, Italy
PortMap VHF Radar System	JCU / QSEC - Townsville, Australia

Table 3.1 Data Sources and Contributors

The next section will describe the chosen experimental site and surrounding environment. Following this, an overview of the various scientific instruments provided by the Italian organisations will be described. The VHF PortMap Radar and its deployment is detailed separately in the following chapter.

3.2 Experiment Location

Surrounding the City of Venice in Italy is the Venice Lagoon. This is the largest lagoon in the region of the Adriatic Sea, having a surface area of 550 km^2.

Figure 3.1 - The Venice Lagoon
(Image courtesy of Nasa Earth Observatory)

The Venice Lagoon is mostly quite shallow consisting of 80% mud flats and salt marshes and having an average depth of only 0.5 m. Three inlets connect the lagoon to the Adriatic Sea. These are the Lido Inlet, the Malamocco Inlet and the Chioggia Inlet (Figure 3.1). The Lido Inlet is situated in the Northern section of the Lagoon, the Malamocco Inlet is a little further south of this and the Chioggia Inlet lies at the southern most end of the Lagoon.

The Lido Inlet is a shallow, tidal inlet having a maximum width of 900 m across, an average depth of approximately 12 m and a typical tidal range of between 0.3 m - 1 m. As can be seen in Figures 3.1 and 3.2, Venice is the largest island in the centre of the Lagoon, with the Lido Channel closely situated directly to the east. The peninsula directly north of the Lido channel is called Punta Sabbioni whereas the narrow island to the south is known as the Lido.

Figure 3.2 - Venice and the Lido Channel
(Image courtesy of Nasa Earth Observatory)

Artificial breakwaters constructed of rock, concrete and concrete tetrapods extend out into the Adriatic Sea from both the Punta Sabbioni and the Lido sides of the channel. Lighthouses have been constructed at the end of these breakwaters to aid shipping navigation. The Lido channel is navigable by shipping and is the primary entrance used by Cruise Liners and Passenger and

Car Ferries to gain access to the Port of Venice. A network of deep shipping channels and smaller canals have been dredged and maintained throughout the lagoon to facilitate access for shipping. The mainland Commercial Port, located on the western side of the Lagoon at Marghera is accessed via the Malamocco Inlet to the south.

The investigation of mass transport and small-scale dynamics through the Lido Inlet is of particular interest due the occurrence of flooding events which affect the City of Venice. These floods known locally as "acque alte" (High Waters) are caused by the combination of astronomical high tides and various meteorological conditions. The meteorological effects can include a combination of heavy rainfall, periods of strong winds from the Bora or Sirocco winds and the presence of low pressure weather systems. These flooding events cause significant damage to the historic architecture and present an economic and social cost to the city. To protect the city from these flooding events, the construction of a barrage gate system known as the "M.O.S.E. Project" has begun at all three inlets to the Venice Lagoon. M.O.S.E., standing for Modulo Sperimentale Elettromeccanico is a flood-gate system consisting of 79 hollow, hinged floodgates that are normally housed within the seabed. When a flooding event is predicted, the system is activated to protect the city. Compressed air is forced into each gate causing the expulsion of water and therefore making the floodgate buoyant with one end rising to the surface (Figure 3.3). Once deployed, these floodgates effectively separate the Lagoon from the Adriatic Sea thereby protecting the City of Venice from the

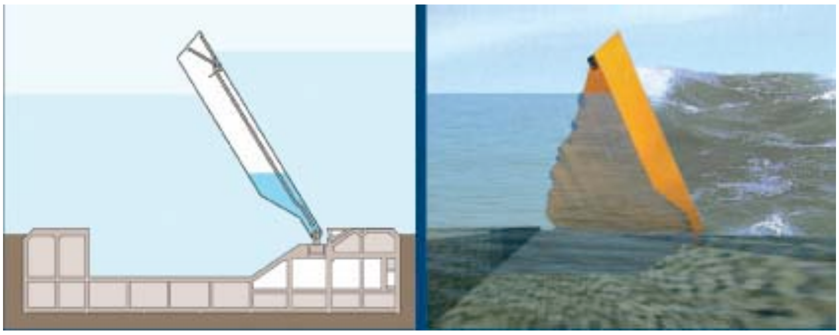

Figure 3.3 - M.O.S.E. Flood-gate deployed
(Image courtesy of Venice Water Authority)

damaging high waters. There has been much controversy surrounding the construction of the M.O.S.E. Project and concern exists about the effectiveness of this system and the impact that periodic closures of the inlet channels will have on the Lagoon environment. As such, particular importance has been placed on investigating the dynamics of the Venice Lagoon and its inlets by the Italian research organisations involved. Some of the previous studies conducted by these organisations have emphasised the investigation of water flow between the Venice Lagoon and the Adriatic Sea (Gacic, M. et al, 2004, 2005).

To complement this ongoing research, the Lido Inlet was selected as the most suitable inlet for the deployment of the PortMap Radar. The two stations of the radar system were set up at the lighthouses at the end of the Punta Sabbioni and Lido breakwaters. The lighthouse positions at each of the seawalls provided convenient access to a power source, security and protection from the elements for the electronic equipment. The geographical and physical positioning of the transmit and receive antennas was also optimal to provide radar coverage of the channel and surrounding sea areas. Furthermore, it was possible to obtain convenient access for monitoring the stations and collecting data files from the station computers during the deployment.

3.3 Deployment Period

The deployment of the PortMap VHF Radar system at the Lido Inlet was undertaken from the 1st October, 2005 until the 11th November, 2005. This would provide continuous data of the surface currents within the channel and outside of the channel for a total duration of 6 weeks. As “acque alte” flooding events in Venice commonly occur during the months of October and November, it was expected that the observation period would encompass a flooding event.

3.4 Acoustic Doppler Current Profiler

To provide subsurface measurements of the current through the channel, an upward looking Acoustic Doppler Current Profiler (ADCP) was deployed on the sea floor within the Lido Channel entrance to the Venice Lagoon. Other similar instruments were also placed in the Malamocco and Chioggia Inlets. These instruments were successfully used in previous studies to record current flow measurements in the channels between the Venetian Lagoon and the open sea (Gacic et al., 2004).

The placement of the ADCP in the channel was determined by Gacic et al. (2004) in previous studies. A process was undertaken for positioning the single ADCP in the channel where the measurements obtained would be most representative of the total water flux through the channel. Initially, current profiles for a channel transect were obtained using a ship-borne ADCP. On average, 100 transect profiles were taken at each inlet, at various phases of flood, ebb and slack tides. From the profiles, the water flux through each inlet was obtained using the proprietary ADCP post-processing software, WinRiver by RD Instruments. Using a linear regression calculation, the resultant value for water flux at various states of the tide was compared to corresponding vertically averaged currents for various points across the transect. The selected location for the ADCP was at a point on the transect where the linear correlation between these was a maximum, thereby making the single point location measurements indicative of the inlet water transport rate.

The chosen location for the ADCP in the Lido Inlet is at position 45°25'21.00"N, 12°25'35.60"E as shown in Figure 3.4. This position is closest to the Lido side of the channel and within the deepest portion of the channel. Mounted on the sea floor, the self-contained ADCP requires regular inspections by CNR-ISMAR staff to retrieve data and for maintenance and cleaning. The ADCP continuously acquired data during the six weeks of the PortMap Radar deployment, except for a short duration on the 12th October when it was retrieved for data collection and maintenance. As can also be seen in Figure

3.4, the location of the ADCP is within the estimated range of the PortMap Radar system.

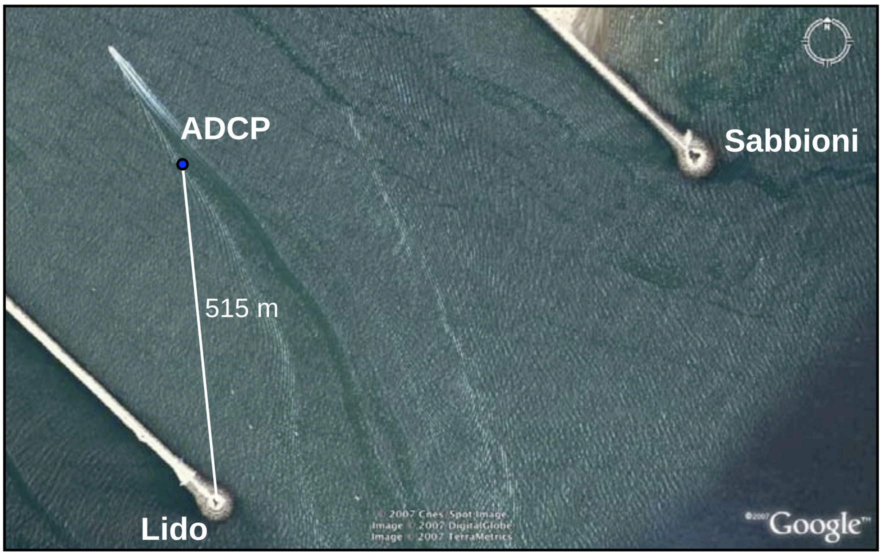

Figure 3.4 - ADCP Location, Lido Channel
(Image map courtesy of Cnes/Spot, DigitalGlobe, TerraMetrics and GoogleEarth)

The ADCP used in the Lido channel is an RD Instruments Workhorse Sentinel operating with an acoustic frequency of 600 kHz. It has been set at a vertical profiling resolution of 1 m depth cell size. At this operating frequency and depth cell size, the Workhorse Sentinel model is capable of a maximum range of 43 m which is more than adequate for its deployment in this channel which is no more than 14 m deep. Current speed and direction are recorded onto an internal memory card every 10 minutes as an average of 60 pings. The Workhorse Sentinel ADCP features four transducer beams with 20° beam angles. In its position on the sea floor at a depth of 13 m, the ADCP will theoretically only experience sidelobe interference within the upper 0.78 m of the water column, based on the formula given in Section 2.2. The four transducer design provides good data reliability with a redundant data source for resolving three dimensional current velocities. In the case of a blocked beam or failure of one of the transducers, current measurements are still obtained with the remaining three transducers. With all four transducers operational, however, an error velocity measurement is provided that can be used to evaluate horizontal homogeneity within the flow and subsequently, the accuracy of the measurements obtained.

3.5 Additional Instrumentation

Through the Italian partners to the project, additional data from tide gauges and meteorological instruments have been made available for the duration that the PortMap Radar was deployed.

Tide data from stations at the Lido, Malamocco and Chioggia Inlets have been provided. Additional data have been provided from a station at Punta della Salute in the City of Venice, and a tide gauge at the oceanographic tower situated approximately 7 NM SSE of the Lido Lighthouse. Tide level data from all these tide stations have been recorded at 5 minute intervals.
A Meteorology station, also situated on the oceanographic tower has provided the measurement of :-

- atmospheric pressure
- air temperature
- water temperature
- relative humidity
- solar insolation
- average windspeed
- maximum windspeed
- average wind direction
- rainfall

The anemometer used to record wind speed and direction measurements is at a height of 15 m above the average sea level. All the meteorological data have also been recorded at 5 minute intervals. These data sources will be sufficient to validate and to supplement the data provided by the PortMap Ocean Surface Current Radar.

4 PortMap Radar and Deployment

This chapter presents a brief overview of the historical development of the PortMap radar, followed by a detailed description of its range and azimuth resolving methods, hardware design, and data acquisition and control software. Also covered are the test deployments undertaken in Townsville and the deployment of the system to measure surface currents within the Lido Inlet, Venice.

4.1 Development of the PortMap Radar

The Portmap Ocean Surface Current Radar (PortMap) is a further development on the well published James Cook University's COSRAD system referred to in Chapter 2 (Heron and Prytz, 2003). The COSRAD system is a pulsed Ocean Surface Current Radar similar to the original CODAR system presented in the first chapter, however it operates in the VHF band. This system has been successfully used to investigate fine-scale structure in surface flow for a number of coastal settings and experiments. These include deployments to investigate the interaction of tidal flow from the Barra Nova Inlet in Ria Formosa (Portugal), the mapping of coastal currents for the placement of Coffs Harbour sewage outfalls, and measurements for coastal engineering planning for Cairns Port Authority and Geraldton Harbour board. An example of the current mapping capability for the Coffs Harbour deployment is depicted by the current map shown in Figure 4.1.

This system was capable of producing surface current maps with a range resolution of 100 m up to a range of 1.5 km. The system used a steerable, rotating pedestal with a 4-element linear antenna array that was used for both transmission and reception. It achieved this by transmitting 670 ns long radio wave pulses on a frequency of 152.2 MHz through the antenna array. These pulses were spaced 2 ms apart. Since this system spends the majority of the transmit/receive duty cycle in receive mode, its overall range was limited by the high peak power required within the short transmit time. A further limitation is the blind range in front of the radar that is not observable because the system is still transmitting while return signals would be observed from the near range. For a 670 ns pulse, this corresponds to a blind range of 201 m in front of the radar with an additional distance to allow for transients in the Transmit/Receive switch to settle down.

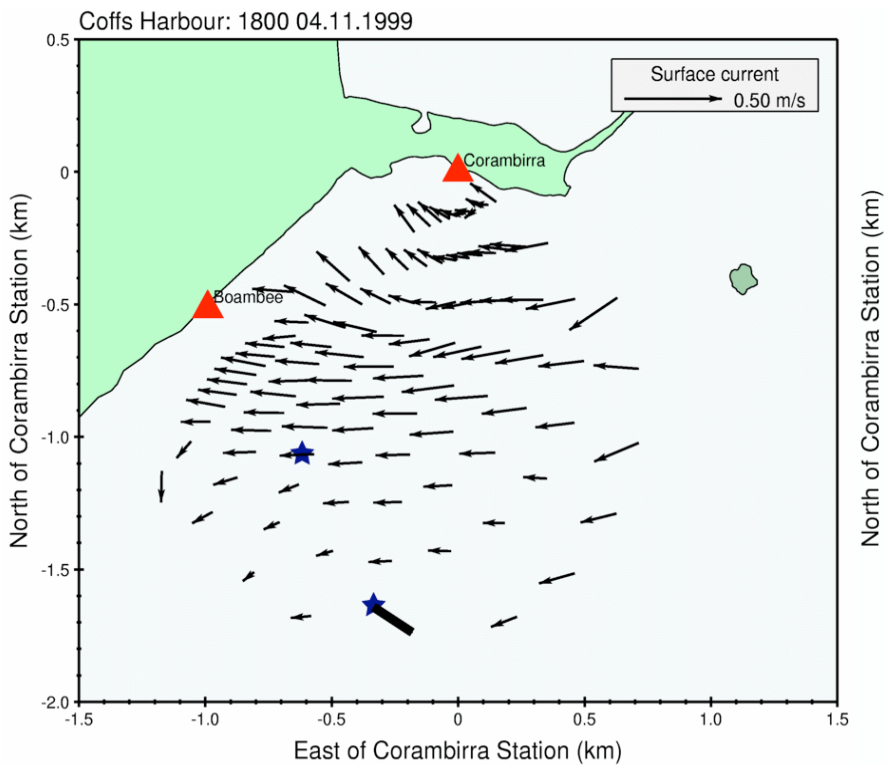

Figure 4.1 - COSRAD Current Map (Heron and Prytz, 2003)

The PortMap radar, produced by a group led by Helzel Messtechnik GmbH is aimed at overcoming some of the limitations inherent in the COSRAD system. The technology of the established WERA HF Ocean Surface Current Radar has been adapted to operate in the VHF band to provide short-range, high spatial resolution measurements. As such, both PortMap and WERA are continuously transmitting, chirped frequency-modulated continuous wave (FMCW) radars. The primary advantage of using a continuously transmitting scheme over the existing COSRAD pulsed system is that a greater maximum operating range should be achievable with a lower peak output power required. This will be with the same 100 m spatial resolution as the COSRAD system. Similar to the COSRAD system, the PortMap radar uses a steerable, pedestal mounted receive antenna array, but with a separate transmit antenna mounted on a central pole. The PortMap system retains the advantages of the COSRAD system in being easily deployable with a compact antenna system.

4.2 PortMap Radar, Frequency Modulated Continuous Wave Operation

The PortMap radar uses linear FMCW chirps to continuously transmit and receive radio wave signals to and from the ocean surface under investigation. The details of the operation of this continuously transmitting FMCW system presented here for the PortMap radar are as outlined by Gurgel (1999b) for the Wellen Radar (WERA).

4.2.1 Range Determination

As with all radar systems, range determination is derived as a function of the propagation time delay between transmission and reception and the speed of light, as presented in Chapter 2 by Equation 2.8.

As time gating cannot be used in a continuously transmitting system to determine range to target cell, another technique is used. The PortMap system transmits linear frequency chirps as represented by

$$s(t) = \sin\left[2\pi\left(f_o + \frac{b}{2T}t\right)t\right] \tag{4.1}$$

where the frequency of the transmitted signal varies linearly from f_o to $f_o + b$ over the chirp period, *T.* The system repeats the transmission of this signal. Continuing with the analysis presented by Gurgel (1999b), the received signal is comprised of the superposition of HF waves backscattered from all ranges, as represented by

$$r(t) = \int \alpha\ (\tau)\ \sin\ [2\pi\ (f_o + \frac{b}{2T}(t-\tau)\ (t-\tau)\ + \phi]\ d\tau \qquad (4.2)$$

where τ is the propagation time between transmission, scattering and receiving. The amplitude $\alpha(\tau)$ and phase $\varphi(\tau)$ vary with time due to the scattering surface waves (assumed to be constant during chirp period, *T)*. After phase-coherent demodulation, the received signal is comprised of the in-phase and quadrature time series representation

$$z(t) = \int \frac{\alpha\ (\tau)}{2}\ exp\ \left[i \left(-2\pi \frac{b\tau}{T} t + \phi(\tau) + \varphi(\tau) \right) \right]\ d\tau \qquad (4.3)$$

Resolving this signal into ranges is achieved from the Fourier transform of each single chirp. From this, the resolution of the frequency $f = b\tau / T$, is determined by the length *T* of the chirp, i.e. $\Delta f = 1 / T$. This therefore dictates the resolution of both propagation time and range resolution as

$$\Delta\tau = \frac{T\Delta f}{b} = \frac{1}{b}\ , \quad \Delta r = \frac{c}{2}\Delta\tau = \frac{c}{2b} \qquad (4.4)$$

Using this relation, the Portmap Radar operating with a bandwidth, *b* of 1.5 MHz and speed of light, *c* has a range resolution of 100 m.

The next step is the Fourier transformation of each chirp. This must be implemented with a windowing function to prevent any leakage problems associated with the spectral analysis (Gurgel, 1999b). This leakage can cause high energy signals from near ranges to mask low energy signals from more distant range cells. After the application of the Fourier transform to each chirp, the resulting amplitudes represent the slowly varying modulation of the backscattered signal from the scattering surface waves.

Once sorted into range cells, this result becomes

$$v(n\Delta r, t) = \alpha(n\Delta\tau, t)\, \exp\left[i\ \varphi(n\Delta\tau, t)\right] \qquad (4.5)$$

where n is the range cell number. The resulting time series data for the sample period is equivalent to the results achieved with a pulsed radar such as the COSRAD or CODAR systems, but with continuous transmission and reception. For each receiver (antenna element), the time series data collected for the various range cells is a superposition of all backscattered signals from all directions within that annular range cell.

4.2.2 Azimuth Determination

The PortMap radar uses a four element, linear antenna array for the receiving of signals. The signal from each antenna element signal is received and processed as above to provide Fourier transformed I and Q channel time-series data for each range cell. As amplitude and phase information is recorded for each channel, either beam forming or direction finding techniques can be used to determine the azimuth to the target area. This will be covered in further detail in section 4.4 Radar Antenna System, of this chapter.

4.3 Electronic Hardware and Operation

The PortMap system uses a combination of electronic hardware for the radio frequency sub-system and real-time embedded computers to perform the various control and processing tasks. These are all contained in a portable 6 unit 19” rack case, as shown in Figure 4.2. An additional workstation computer running the SuSE Linux operating system provides a user’s console for configuring and operating the system, and is also used for the storage of acquired data.

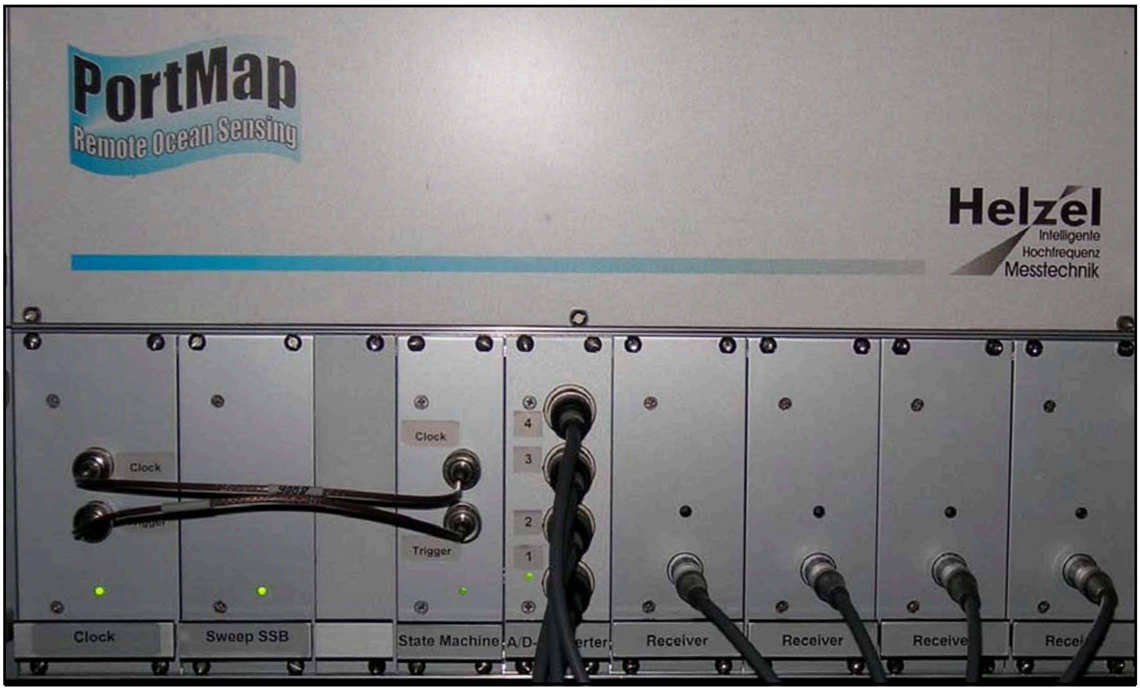

Figure 4.2 PortMap Rack Electronics

The most critical aspect of the operation of the FMCW design, is the linearity and phase stability of the generated chirps. This is achieved in PortMap by using a highly stable synthesiser as a master system clock. This system clock provides stable timing pulses for the State Machine and a Direct Digital Synthesiser (DDS) which are used for generating the FMCW linear chirps with low phase noise. The use of a DDS in the system provides an ideal method for generating linear chirps, with the added flexibility provided by software control. A block diagram of the hardware contained within the PortMap system is shown in Figure 4.3. The DDS generated chirp signal output by the Sweep Single Sideband (Sweep SSB) unit is split into five channels. The signal from one channel is used to drive the transmit amplifier where it is amplified to 16 dBm before feeding the transmit antenna.

Signals received at each of the receive array elements are bandpass filtered before passing to the receivers. The remaining four chirp channels are used by

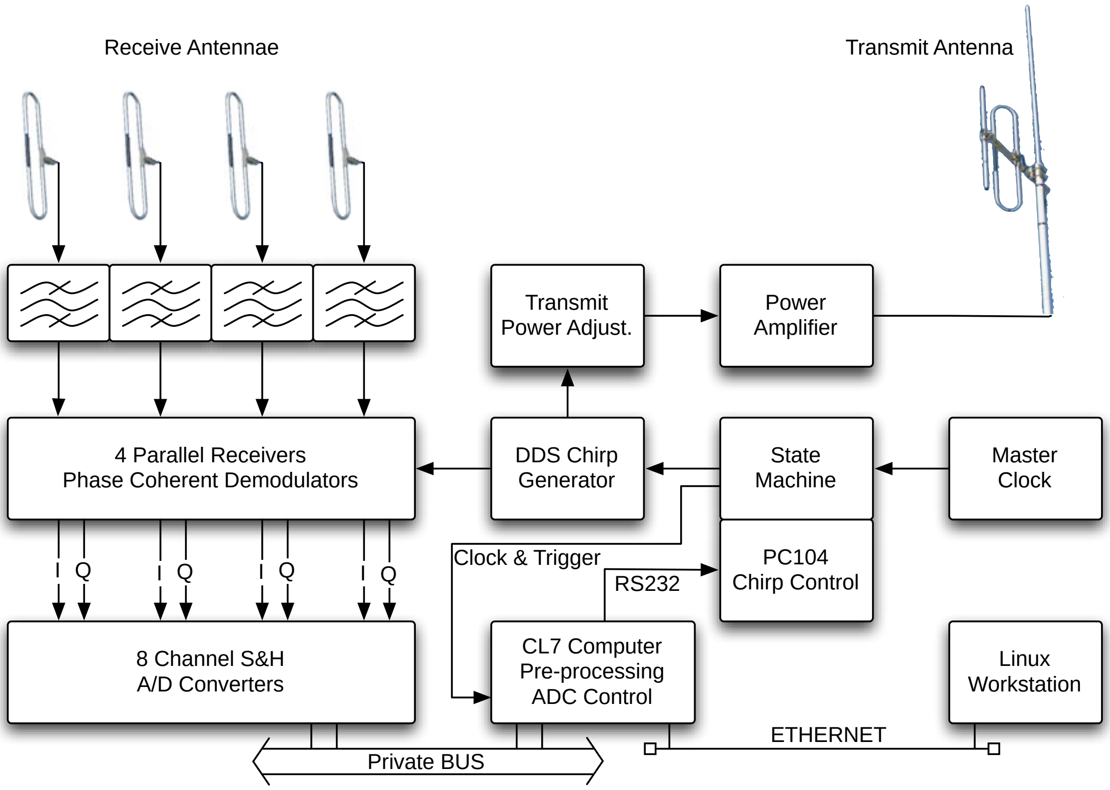

Figure 4.3 PortMap Hardware Block Diagram
(Adapted from WERA Diagram - Gurgel, 1999b)

the four direct-conversion receivers for phase-coherent demodulation. The demodulated I and Q channel signals are low pass filtered to prevent aliasing, before being sampled by the analog to digital converters (ADCs).

The ADCs are controlled by the CL7 Real-time computer. This unit receives commands from the Linux workstation at the commencement of a measurement run and initiates the chirp generation and the ADCs. Data acquired by the ADCs is buffered and transferred to the CL7 computer via a private bus. In real-time, the data are then resolved into ranges as per the FMCW range-resolving method using Fast Fourier Transforms. This range-resolved time-series of I and Q values is then stored in binary files on the Linux workstation by means of Network File Storage (NFS) protocols over the ethernet connection. The PC 104 computer also shown in Figure 4.3 is used to control the settings and sequences for the chirp generation. Parameters of these are configured on the Linux workstation and transferred via ethernet to the CL7 computer.

4.4 Radar Antenna System

The antenna system for the PortMap radar contains both transmitting and receiving elements in the same unit, along with motor control for the physical steering of the array. Physical steering of the array provides the ability to acquire data over a single sample period from one direction, before re-positioning the antenna to observe a different area of ocean. In addition to the physical steering, electronic steering is used to steer the receive array with +/-30° of the boresight direction. In this way, it is possible to cover a greater measurement area with more precise beam-forming or direction finding accuracy than would be possible with a fixed antenna. Even with this capability, the PortMap antenna system is designed to be lightweight, portable and easily deployed in the field.

Figure 4.4 PortMap Antenna System

Construction

The heavy steering motor and gearbox, and control unit are positioned at the base of the antenna to keep the centre of gravity low. To this motor base, a lightweight PVC housing is fixed. This housing shrouds the antenna cables and drive shaft and acts as a stable platform and bearing edge for the receive array bar. The receive array bar is fixed to a top cap which rests on this bearing edge. The drive shaft consists of shorter segments and is connected to the gearbox fitting, the top cap, and continues further up to the single transmit antenna mounted above. These three physical elements then rotate together under the control of the motor. The antenna cables within the PVC housing are allowed to move freely before exiting through the rotating top cap. The bar that the receive antenna array elements attach to is 3 m long corresponding to three half-wavelength (98.6 cm) sections which separate the four receive elements.

Unlike Ocean Radar systems operating at High Frequencies (HF), PortMap is operating in the Very High Frequency (VHF) band so the physical size of the antenna elements is quite compact. Small elements and the small cross section of structural elements help to limit the amount of wind-loading exhibited by the entire antenna. To keep the antenna stable, guy ropes are attached to the top of the PVC column and taken out to either fixed or temporary anchor points while the unit is deployed. As the unit is to be deployed in coastal areas where strong winds are likely, it is important that the structure is made secure.

Steering Control

The antenna rotation motor is controlled by a programmable logic controller (PLC) also housed within the motor base. This is remotely controlled from the PortMap workstation computer via an RS-232 or RS-485 communications link. The PortMap workstation computer sends an ASCII command string to move the antenna. This command string contains the integer value for the desired antenna angle (0° to 359° from start position). The PLC processes this command string and controls the motor such that the antenna only rotates +/- 270° from the start position. This is to prevent the cables inside the PVC housing from twisting too tightly.

On the PortMap workstation, a configuration file permits the user to define the desired antenna start position, the number of times to change, and the angle of change each time the antenna is rotated. A background program running on the workstation then advances the antenna to the next antenna angle in the sequence, one minute prior to data acquisition from that direction. The boresight angle of the antenna is recorded as meta-data in the acquisition file obtained for that direction.

Transmit Antenna

Since the receive antenna array elements are omnidirectional dipoles, the transmit antenna needs as high a front-to-back ratio as is possible. A Deep Null, 2-element Yagi antenna is used to achieve this on the PortMap system. According to the manufacturer's specifications, a nominal front-to-back ratio of 14 dB is achievable with a small forward gain of 6 dBi.

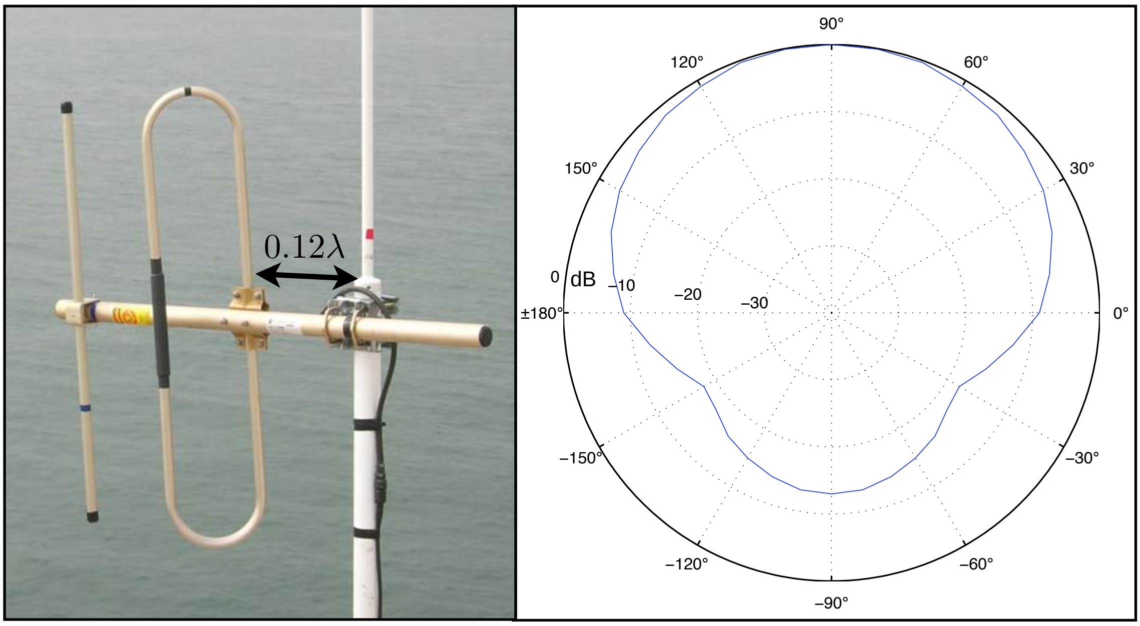

Figure 4.5 Deep Null Yagi Transmit Antenna and Polar Response

The Deep Null Yagi antenna achieves its very high front-to-back ratio by using the mounting structure (centre shaft) to act as a reflector for the antenna. This requires the mounting shaft to be spaced 0.12 wavelengths from the edge of the dipole (as shown in Figure 4.5). This distance is 23.7 cm for the operating frequency of 152.2 MHz.

Of particular note with this transmit antenna is the wide horizontal beamwidth of 130˚. As shown in the next section, this angle is significantly more than the beam forming acceptance angle of 60 degrees.

Specification	Value
Impedance	50 Ohm
VSWR	14 dB
Front / Back Ratio	14 dB
Horizontal Beamwidth	130˚
Vertical Beamwidth	70˚

Table 4.1 Transmit Antenna - Other Specifications

Phased Array Receiving Antenna

The azimuthal resolution of the PortMap system highly depends on the receive antenna array, and more specifically its beamformed radiation pattern and beamwidth. The receive antenna is a linear phased array of identical omnidirectional dipoles. The far field radiation pattern of this array is a direct result of the geometric arrangement, and the relative amplitudes and phases of the array elements, as well as the single element radiation pattern. This far field radiation pattern is because of the introduction of relative phase shifts in the radiation vectors, adding constructively in some directions while destructively in other directions. As our single element radiation pattern is isotropic, the array exhibits a radiation pattern dictated by the array pattern multiplication property where the total radiation vector is given by

$$\boldsymbol{F}_{tot}(\boldsymbol{k}) = A(\boldsymbol{k})\ \boldsymbol{F}(\boldsymbol{k}) \tag{4.6}$$

where ***F (k)*** is the factor due to a single element and

$$A(\boldsymbol{k}) = a_0 e^{j\boldsymbol{k}.\boldsymbol{d}_0} + a_1 e^{j\boldsymbol{k}.\boldsymbol{d}_1} + a_2 e^{j\boldsymbol{k}.\boldsymbol{d}_2} + \ldots \tag{4.7}$$

is the array factor.

Since $\boldsymbol{k} = k\,\hat{\mathbf{r}}$, the array factor may also be denoted as $A\,(\hat{\mathbf{r}})$ or $A\,(\theta, \phi)$.

For the 4-element PortMap array, the array factor can be written as

$$A(\phi) = a_0 + a_1 e^{jkd\cos\phi} + a_2 e^{2jkd\cos\phi} + a_3 e^{3jkd\cos\phi} \tag{4.8}$$

where k is the wave number, d is the antenna separation and ϕ is the steering angle. The PortMap array antenna dipoles are horizontally spaced along the array mounting bar with a half-wavelength separation distance of 98.5 cm. The operating wavelength is 1.97 m (f = 152.2 MHz). With this half-wavelength element spacing, unity amplitudes and no phase shift between the elements, the array pattern results in a directional beam broadside to the linear array, as shown in Figure 4.6. This pattern also shows that the linear array exhibits an equal response behind the array. This clearly shows the importance of the high front-to-back ratio of the transmit antenna presented in the section above. By constraining most of the transmitted power to the forward direction we are able to 'steer' the phased array through the radiated area to receive signals from the forward direction. The rear lobe is then not considered significant, as very little signal is received from this direction.

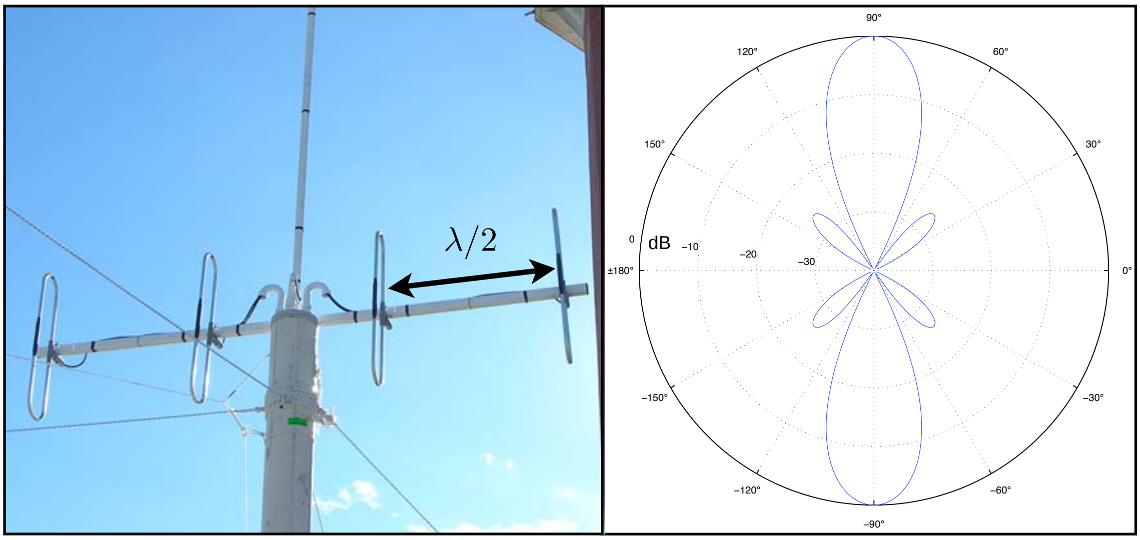

Figure 4.6 PortMap Receive Antenna Array and Polar Response

At this broadside steering position with no additional phase shift between the elements, we can evaluate the 3-dB beamwidth, $\Delta\phi_{3dB}$ by differentiating the equation $\psi = kd\cos\phi$, that is

$$d\psi = \frac{\partial\psi}{\partial\phi}d\phi = (-kd\sin\phi)d\phi \qquad (4.9).$$

If this derivative is evaluated at broadside (ϕ = 90˚) and assume a relatively narrow mainlobe, this becomes

$$\Delta\psi_{3dB} = \left|\frac{\partial\psi}{\partial\phi}\right| \Delta\phi_{3dB} = kd\ \Delta\phi_{3dB} \tag{4.10}$$

and solving for $\Delta\phi_{3dB}$, we obtain :-

$$\Delta\phi_{3dB} = 0.886\frac{\lambda}{Nd} \tag{4.11}$$

For the PortMap array, this calculates to a 3dB beamwidth of 25˚. This beamwidth applies only at broadside ϕ = 90˚. Beam steering is achieved by modifying the steering angle ϕ by introducing additional phase shift between the elements of the array. The pattern of the beam and the corresponding beamwidth varies as it is steered through various angles from ϕ = 0˚ to 90˚. This is seen in Figure 4.7 where additional phase shift between elements is incremented by $\pi/6$ radians for each subsequent polar plot.

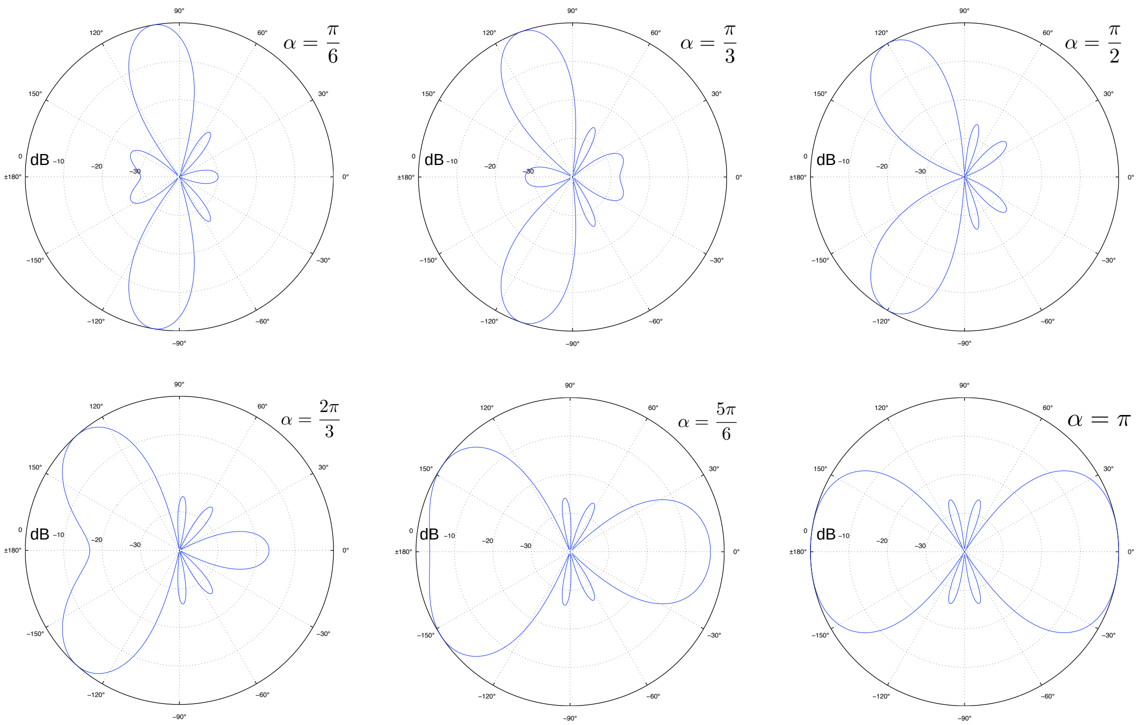

Figure 4.7 Steered Array Normalised Polar Plots (Element Phase Shift, α in radians)

The antenna pattern significantly broadens for angles, ϕ > 30˚ as seen in the last three subplots. Therefore, the practical physical limit that the beam can be steered with the phased array is +/-30˚ from the broadside direction. This corresponds to a phase angle, $\alpha < \pi/2$ radians.

In practice, the application of phase shift between the antenna elements is typically performed in the time domain. Since in the PortMap system each of the signals received by the individual elements are separately demodulated and have their I and Q time-series values recorded, this can be performed in software on either the time-series data or on Fourier transformed spectrum data.

4.5 PortMap Radar Control and Data Acquisition

User Control of the PortMap radar is via the Linux workstation running the SuSe Linux operating system. On this platform, a web based interface is used to control the radar parameters and timing of data acquisition. This interface communicates configuration settings to the other real-time computers in the system via the WeraDesk CGI binary. The real-time computers communicate back to the workstation by writing status information directly back to the workstation system drive, together with the acquisition data. The user interface for the PortMap workstation is shown in Figure 4.8 with the settings used for the Sabbioni Lighthouse deployment.

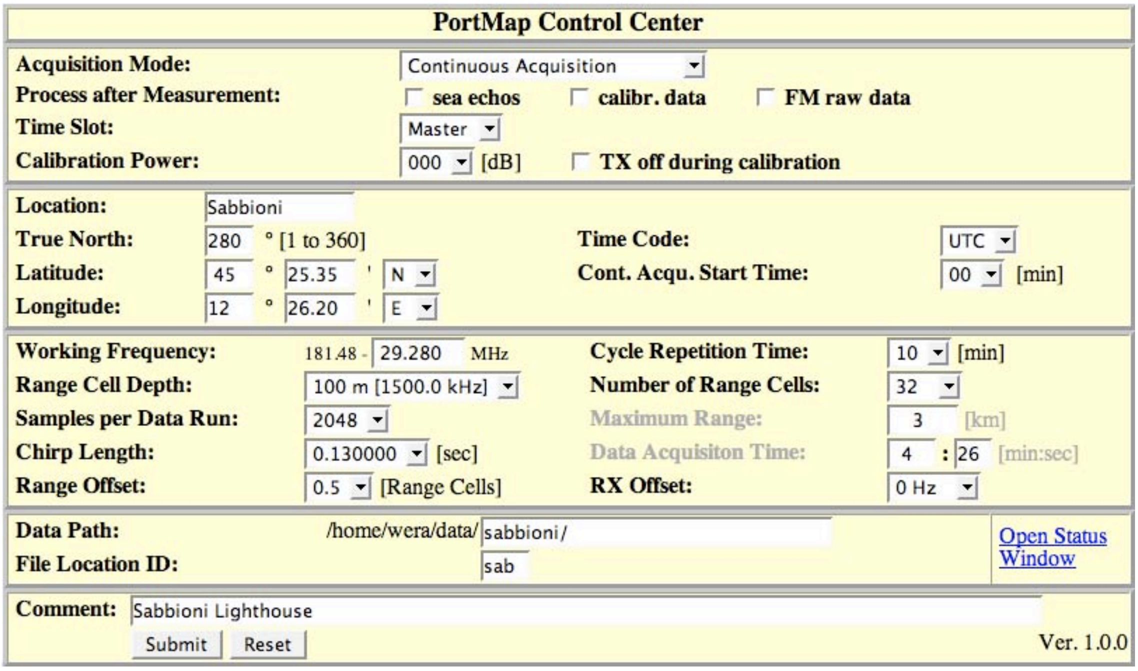

Figure 4.8 PortMap User Interface

Of particular note are the radar settings specified for working frequency, range cell depth, samples per data run, chirp length and number of range cells. These settings dictate the maximum range and the data acquisition time taken for the number of samples of a specified chirp length, i.e. 2048 x 0.13 Sec = 4 minutes, 26 seconds.

The data acquisition time determines the timing sequence that can be used, particularly with a Master and Slave, 2-station system. This is because both stations operate at the same centre frequency of 152.2 MHz. The Master Station takes 4 minutes, 26 seconds with a cycle repetition time of 10 minutes. This allows a Slave Station to start at 05 minutes and acquire data for 4 minutes, 26 seconds before the Master station repeats its acquisition. The real-time system clock on both station workstations provides the timing for both the antenna control and for the start of data acquisition. Because of this, it is important that the system clock is accurately set on both workstations, as there is no automatic synchronisation between the systems. Timing signals from the NAVSTAR Global Positioning System (GPS) could possibly be used to provide this level of synchronisation but are not presently used.

As described in Section 4.4, a separately modified configuration file, position.drv is used for controlling the antenna motion. A typical configuration file appears as :-

```
280   % Start Position in integer degrees
-60   % Position change in degrees (Negative - Anticlockwise)
-3    % Number of Position changes
280   % Current Position in Degrees (modified by software)
```

The fourth value in this configuration file is set by the antenna control program each time the antenna is rotated to a new position. This value is read by the PortMap Control Centre and displayed in the field “True North:” to indicate the boresight angle of the antenna. This value is also written as meta-data at the header of each acquisition file.

The range-resolved time-series of I and Q values that are stored as binary files on the workstation can be post-processed and analysed to produce additional data as required. This could be simply converting these binary time-series and storing them to an ASCII file, to the determination of current and wave measurements. For the PortMap system, post-processing software has been developed for Microsoft Windows as both a command-line tool (pmap2dat.exe) and as a graphical user interface (PortMap.exe) to perform these tasks on other workstations independent of the PortMap system. An example of the outputs available from the graphical user interface, PortMap.exe are shown on the next page. Figure 4.9 displays the I and Q channel time-series values for range cell 4, acquired from antenna #1. Figure 4.10 displays the power spectrum calculated from these values. This post-processing software could also be used to produce the beam-formed, time-series or power spectrum data for a particular azimuth angle within this range cell 4. This technique is the basis for obtaining data resolved in both range and azimuth, which will be covered in Chapter 5, Data Analysis and Results.

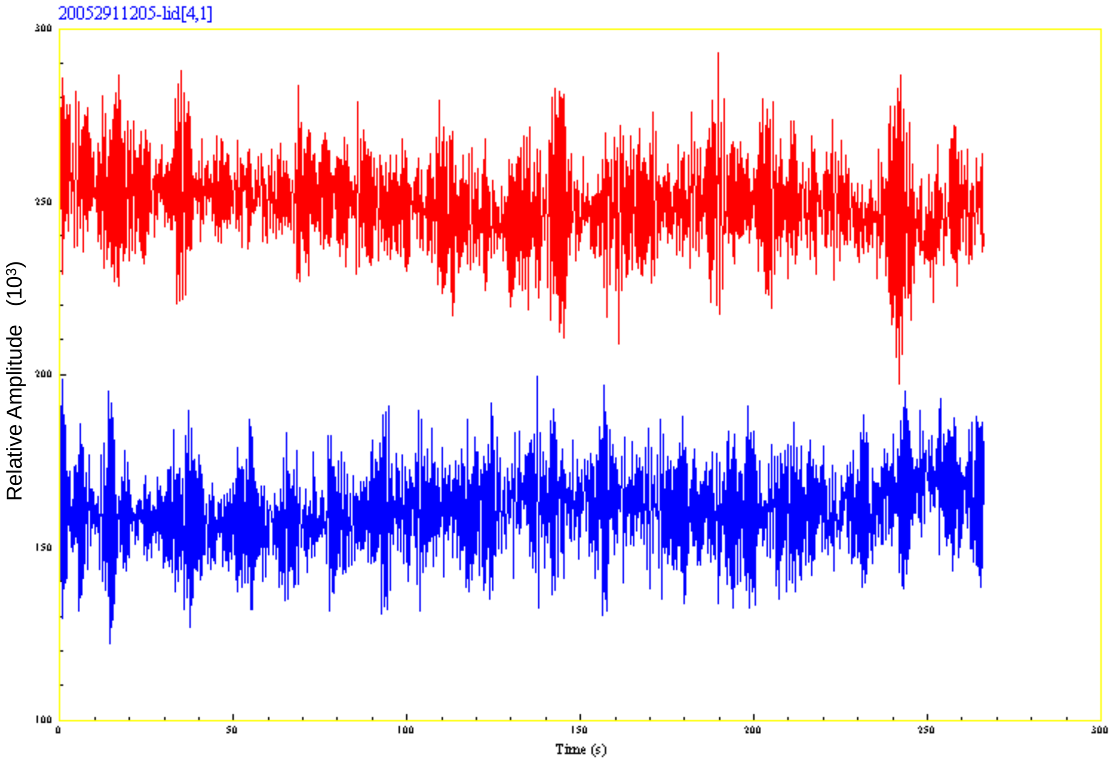

Figure 4.9 Time-Series I (red) and Q (blue) channel for Range-Cell 4, Receive Antenna #1

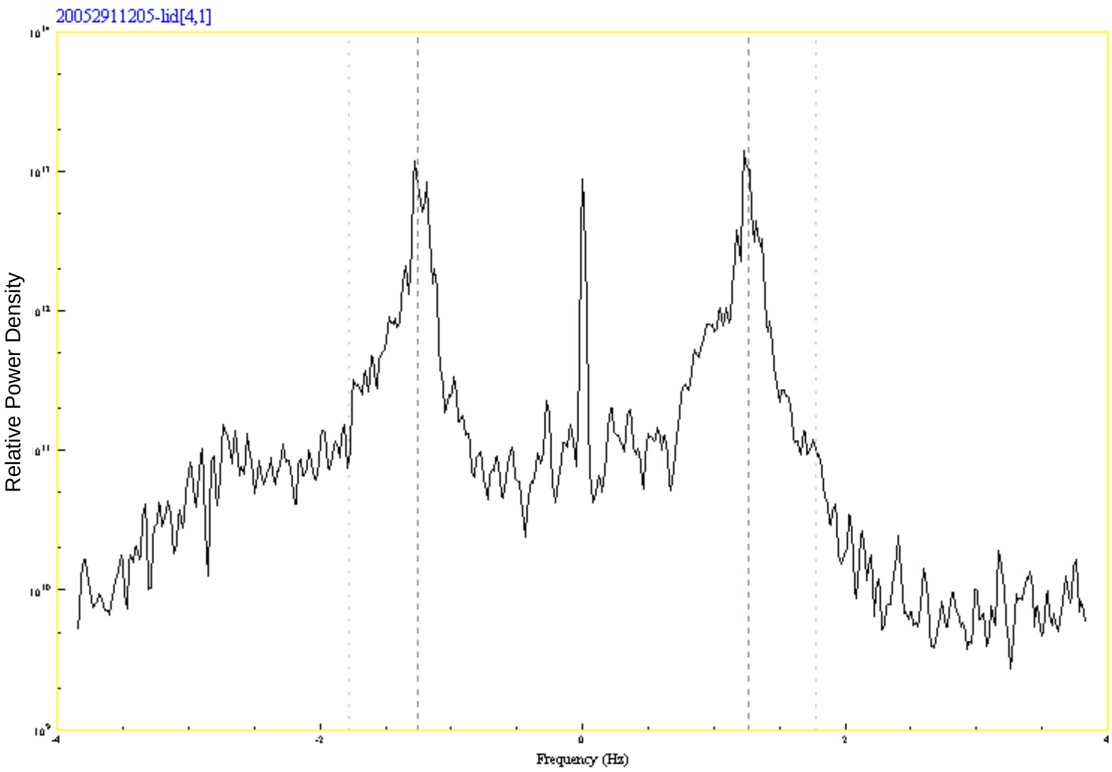

Figure 4.10 Power Spectrum for Range-Cell 4, Receive Antenna #1 (Corresponding to Time-Series shown in Figure 4.9)

4.6 Venice Deployment

The two PortMap radar stations were set up for the 6 week deployment period at the seaward ends of the breakwaters either side of the Lido channel. One station was set up on a mezzanine level of the Punta Sabbioni Lighthouse, the other on a raised concrete block adjacent to the Lido Breakwater Lighthouse. The PortMap electronics and workstation computers were housed inside each of the lighthouses to protect them from moisture and damage from vandalism. Coaxial cables for the antennas together with power and serial communications leads for the motor control were routed from inside the lighthouses out to the antenna systems.

These positions were chosen for their sight lines that encompass an unobstructed view from up the Lido channel through to across and out beyond the channel. This would provide optimal measurement coverage of the channel and the water surrounding each breakwater on the side of the Adriatic sea.

Figure 4.11 PortMap Deployment Locations, Punta Sabbioni (Left) and Lido (Right)

For the system to be able to obtain measurements both inside the channel and out, a steering scheme was adopted such that over a 40 minute period, each station would acquire data from four different boresight directions alternately. In this way, it would be possible to create a complete vector current map that is refreshed every 40 minutes. The timing and directions for this measurement scheme are presented in Table 4.2. Once the end of this sequence is reached, the scheme continually repeats. Over a 24 hour period, 36 acquisitions are recorded for each boresight direction.

Time	Sabbioni Boresight (Master Station)	Lido Boresight (Slave Station)
0	280°	-
5	-	336°
10	220°	-
15	-	36°
20	160°	-
25	-	96°
30	100°	-
35	-	156°

Table 4.2 Antenna Steering Scheme

The projection of these boresight directions onto a satellite image of the channel (Figure 4.12) shows the sequence and coverage zones of this scheme. Although untested, each PortMap radar station is specified to achieve a range of at least 2 km. Regions common in range to both stations dictate the overall system range.

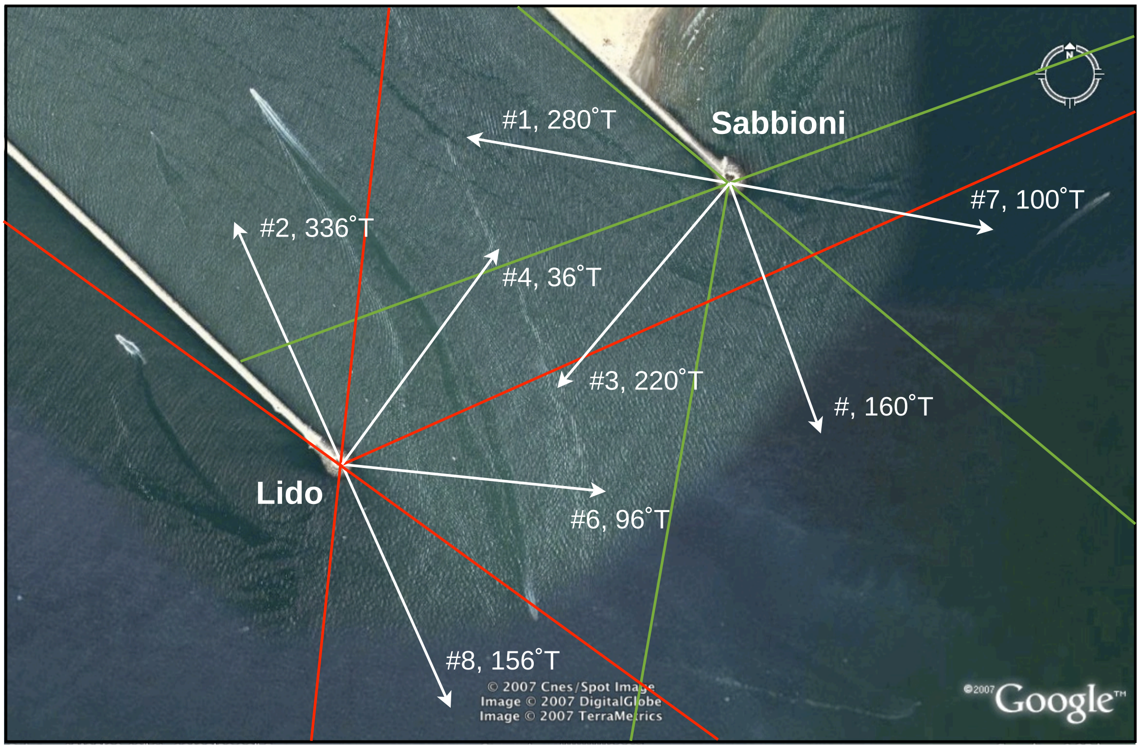

Figure 4.12 Antenna Steering Directions and Sequence
(Image map courtesy of Cnes/Spot, DigitalGlobe, TerraMetrics and GoogleEarth)

A variation to this steering scheme was implemented for three days during the deployment where the radar stations were limited to looking up and across the channel only. Instead of a 40 minute refresh rate of current maps, this would allow updates every 20 minutes.

Time	Sabbioni Boresight (Master Station)	Lido Boresight (Slave Station)
0	280˚	-
5	-	336˚
10	220˚	-
15	-	36˚
20	280˚	-
25	-	336˚
30	220˚	-
35	-	36˚

Table 4.3 Alternative Antenna Steering Scheme

5 Data Analysis and Results

This chapter details how the radar time-series acquisitions obtained over the six week deployment were analysed and compared with ADCP measurements. The first section in this chapter examines the quality of the data obtained from both the radar and the additional instrumentation.

From the very start of the data analysis process it was evident that the radar was not performing to the expected range specifications. Although unknown throughout most of the research effort, the PortMap radar systems used in Venice had a programming fault within the real-time computer software. This was reported by the manufacturer in November, 2006 after most of the data analysis had already taken place. The technical details of this fault will be covered in the final section of this chapter, Section 5.8. The fault effectively caused the range resolution of the system to be 20 m instead of 100 m. This reduced the already poor range of the radar by a factor of 5. As such, the range of the system was insufficient for the purpose of evaluating mass transport through the Lido inlet.

Sections 5.1 through to 5.7 of this chapter describe how current measurements were obtained from the radar spectra and how this could be used to produce surface current measurements along a transect. <u>This was performed on the understanding that the PortMap systems had a range resolution of 100 m.</u> Although now known to be incorrect because of the range resolution error, these sections detail how the analyses and algorithms were developed to provide surface current measurements across the Lido channel transect.

As previously explained, the final section describes the technical details of the PortMap system's fault. It also shows how the direction finding algorithm, DFind was modified to allow for this fault to enable it to create short-range radial current measurements using a range resolution of 20 m, assuming that the dominant energy is from signals of this range resolution. As will be seen in the Discussion chapter, sufficient surface current measurements were obtained within a short range to observe an interesting surface current dynamic within the Lido channel.

5.1 Quality of Data

The quality of the data obtained from the PortMap radar, ADCP, Tide Gauge and Meteorological station (Weather station) are examined in this section. Events causing a complete loss of data where systems were unavailable due to maintenance disruptions or system failure are also reported in this section.

5.1.1 ADCP, Tide Gauge and Meteorological Data Quality

This additional data was provided by the partner organisations, the National Institute of Oceanography and Applied Geophysics (OGS - Trieste) and The Institute of Marine Science (CNR-ISMAR - Venice). It was obtained using commercial instruments and sensors. This provided high quality, reliable data from instruments that have been deployed and used successfully over a long period of time and for previous studies.

For the period of investigation, 1st October - 11th November, 2005 there were no lapses in data (0% data loss) from either the Tide Gauge or Meteorological data sets. These were recorded at 5 minute intervals. The time-series plot shown on the following page (Figure 5.1) represents the wind speed, direction and wind vector data obtained from the weather station for the 1st October.

The self-contained ADCP that was deployed on the sea floor within the channel was retrieved on the 12th October to download the logged data, and for maintenance and cleaning. This resulted in a lapse of ADCP record data on this date for a period of 3 hrs, 40 minutes from 12:20:02 UTC to 16:00:02 UTC. This was considered to be negligible as this represents a mere 0.36% data loss over the period of interest.

A time-series plot of the tide gauge data for the Lido Inlet is displayed in Figure 5.2. This is plotted together with the velocity of the ADCP bin closest to the surface, resolved into the axis of the Lido channel. This gives an overview of the tidal level and corresponding tidal stream velocities within the channel throughout the observation period. Periods of Neap and Spring tides can be clearly observed in this plot.

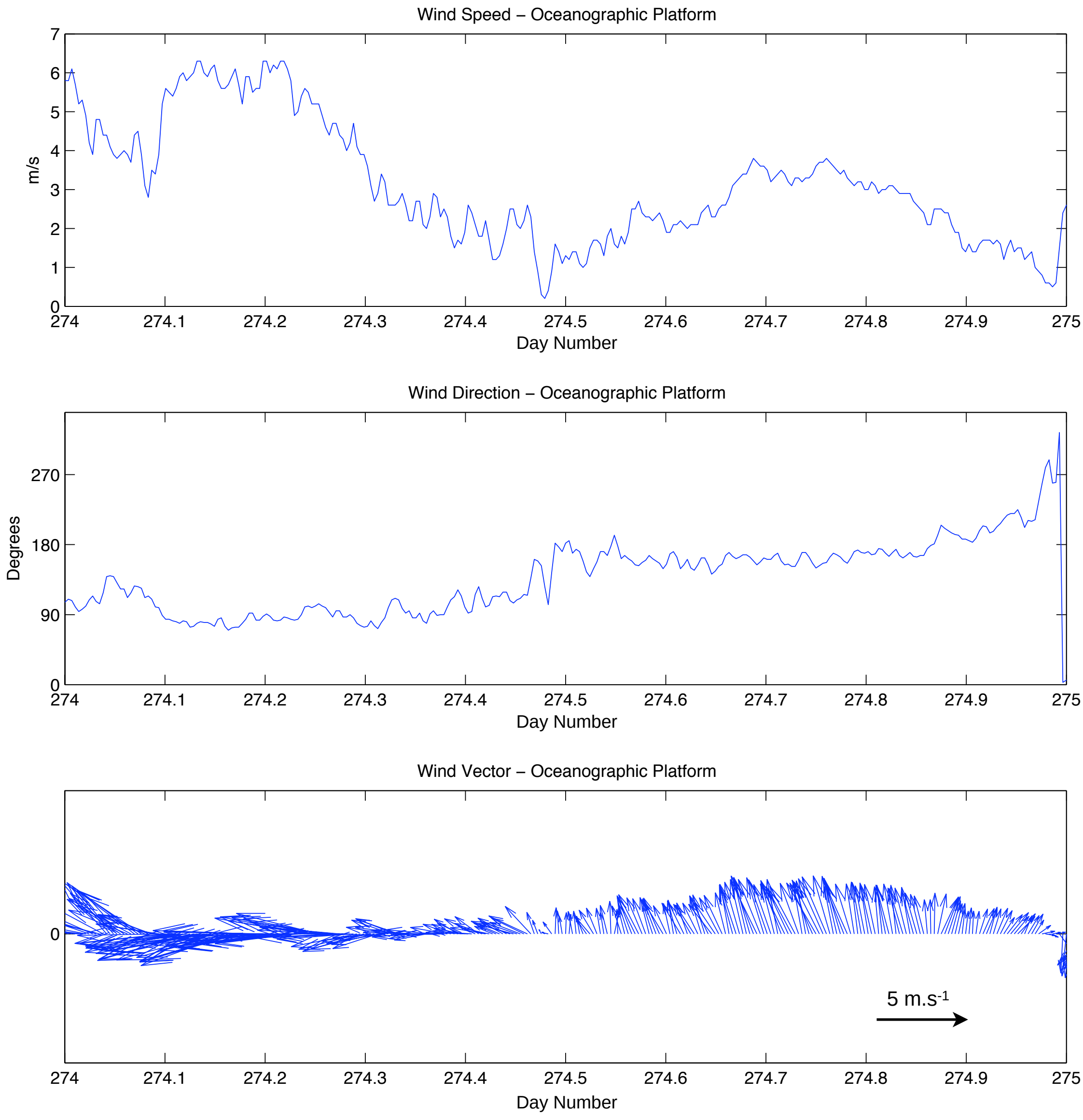

Figure 5.1 Time-series of Wind Speed, Wind Direction and Wind Vector for 1st October

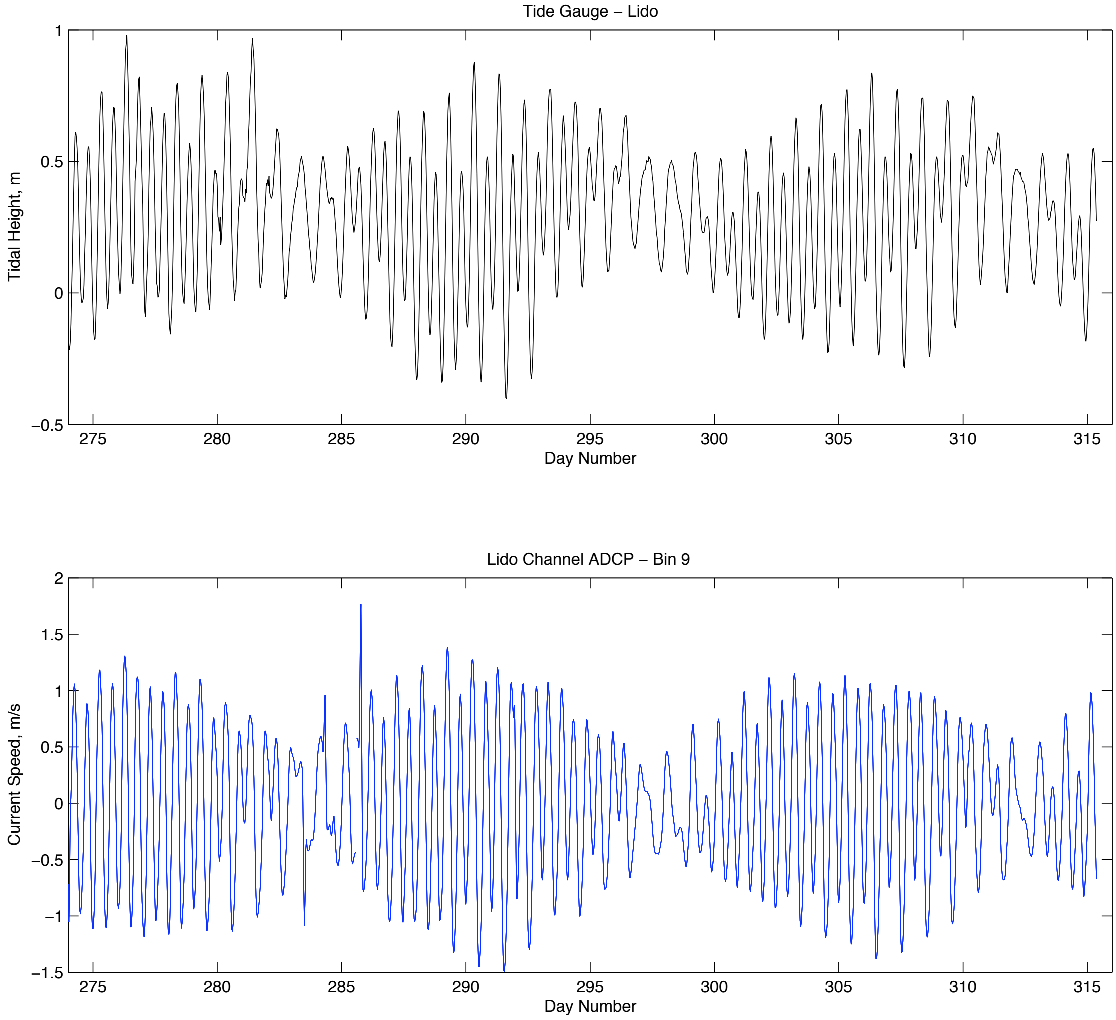

Figure 5.2 Tidal Level and ADCP Bin 9 Velocities for the Lido Channel

In Figure 5.2, the discontinuity on DAY 285 in the Lido Channel ADCP plot represents the period that the ADCP was being serviced. With such a high quality measurement signal, the velocity data obtained from the ADCP provides a sound reference with which to verify the accuracy of the measurements obtained using the PortMap Ocean Surface Current Radar for the ADCP location.

5.1.2 Radar Data Quality

The availability and quality of the measurement of surface currents from the PortMap system depend on obtaining received signals with a good signal-to-noise ratio (SNR) throughout the ranges of interest.

During and immediately following the deployment period, analysis of the radar data took place to observe the signal-to-noise ratio of the recorded signals. This was primarily used to gauge the range at which reliable current data could still be obtained from the radar signals. A post-processing utility, PMAP2DAT.EXE, developed at James Cook University, was used to generate power spectrum files from the binary time-series files written by the PortMap radar. PMAP2DAT was used to output ASCII .dat files containing a 2048 point power spectrum for each antenna, for all 50 recorded range cells. These processed data files were then used by a MATLAB graphical user interface tool developed as part of this Thesis work to present the power spectra graphically as a waterfall plot (Figure 5.3).

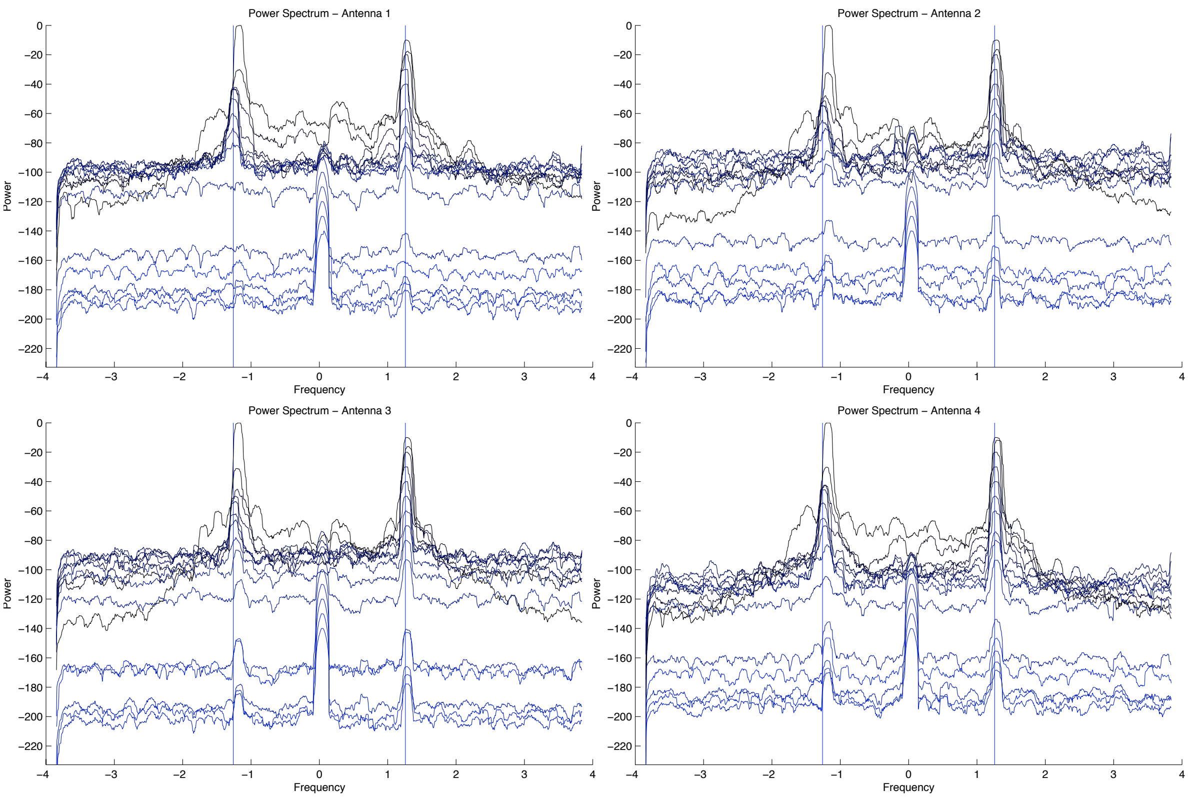

Figure 5.3 Normalised power spectrum plots (ranges 1 to 15) - Good SNR, Index 6

For a single 4 minute, 26 second acquisition, the power spectrum is smoothed using a digital low-pass filter and displayed for a specified number of range cells (typically range cells 1 to 15). The data are also normalised and vertically shifted downward with increasing range to allow for easier inspection. As such, the closest range cell is at the top of the graph.

This graphical representation for each acquisition was visually inspected to estimate the effective range of the radar. The primary indication of good signal-to-noise ratio in the recorded data was the obvious presence of Bragg scatter peaks either side of the 0 Hz centre over a number of ranges. As shown in Figure 5.3, a record with good signal-to-noise ratio shows obvious Bragg peaks extending out to 15 range cells. A record with very poor signal-to-noise ratio such as that shown in Figure 5.4 shows no discernible Bragg peak beyond the first one or two range cells.

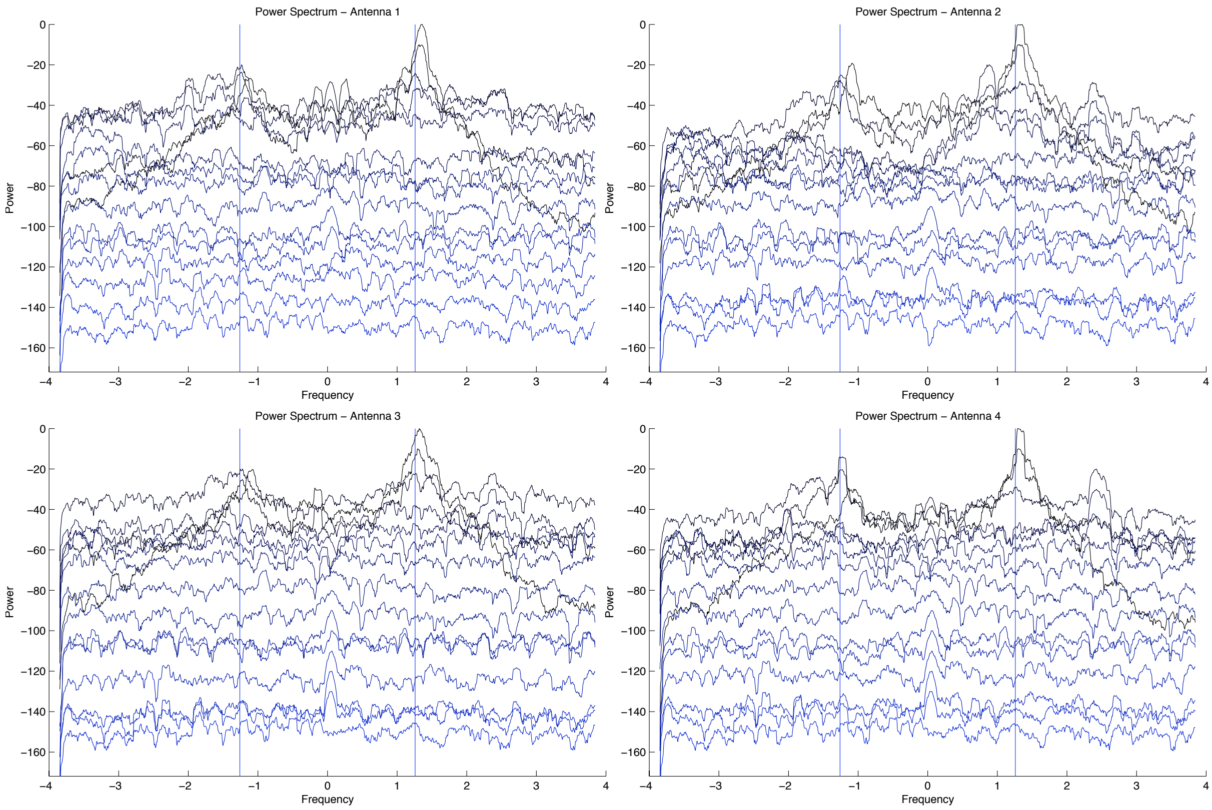

Figure 5.4 Normalised power spectrum plots (ranges 1 to 15) - Poor SNR, Index 1

An estimate of range was evaluated for every record obtained from the radar throughout the six week deployment period. This estimated range was a value from 0 to 6, with a value of 6 indicating that the radar could see in excess of 6 range cells. A rating zero indicated the worst case where the radar had no perceived usable data in this sampling period. As previously indicated, the range resolution during this process was understood to be 100 m at the time of this analysis.

The range estimates for each station were tabled and compared. The histogram in Figure 5.5 shows the distribution of range quality for each station, and for each look direction (left most colour-bar represents the look direction within the channel). Times that the stations collected no data due to failure are ignored. For each station, the radar is mostly perceived to be able to gather data within the first 5 range cells only. Of particular note is the significant number of times that the Lido station is unable to observe any returned Bragg peaks.

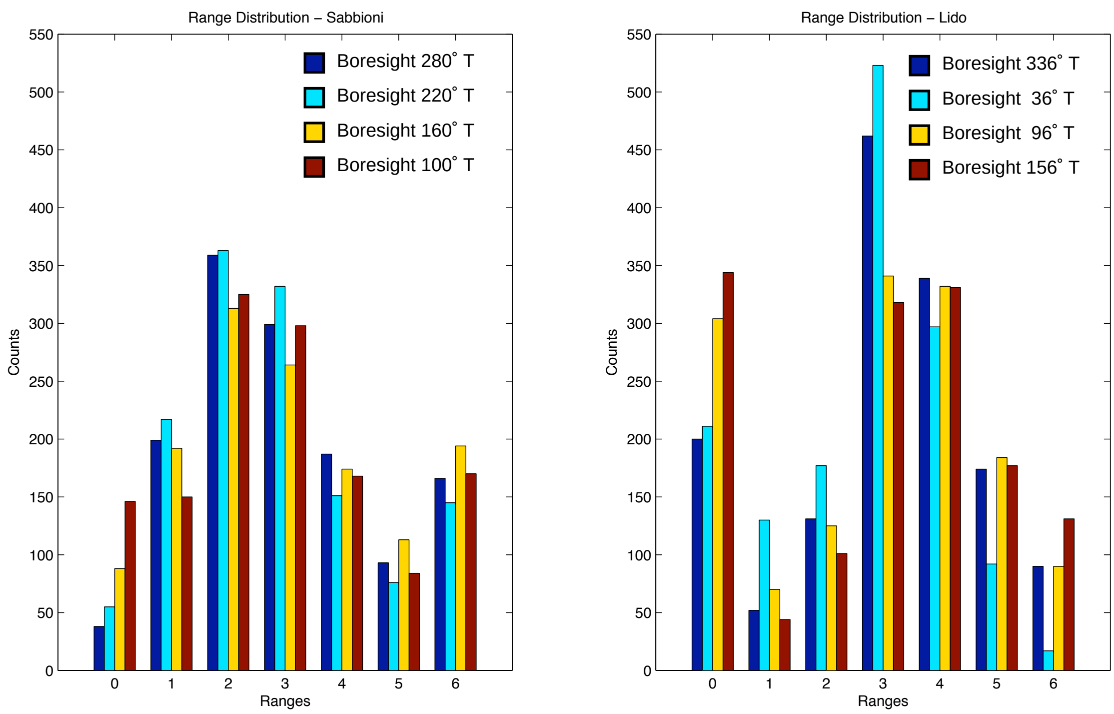

Figure 5.5 Distribution of range quality, Sabbioni and Lido Stations

5.1.3 Radar Failure Events

Although efforts were in place to monitor the stations daily to inspect and correct faults, some data went unrecorded due to system faults. Aside from the Lido station fault that resulted in poor data records, there were only two complete failure events that occurred during the deployment.

The workstation computer at the Sabbioni station completely failed at 2000 local time on the 24th October due to a rodent interfering with the computer's mainboard. This was not locally repairable, and a replacement workstation computer had to be shipped from Germany. This station was brought back online on the 28th October, at 1550 local time. This resulted in a complete loss of data for a four day period.

At the Lido site, minor faults with the antenna controller caused two minor disruptions to the normal sequence of data recording. In the first instance, water ingress caused the power to the antenna to be disrupted on the 13th October. Although data were still recorded, they were only obtained from a single look direction until the fault was fixed the following day. Similarly, a mechanical fault with the motor controller caused the antenna to become stuck in a single look direction the following day. No complete system failures occurred at the Lido station.

5.1.4 Obtaining Surface Current Measurements

From the visual inspection of the recorded radar spectra, we see that most of the time the radar has a range of 500 m or less (100 m range resolution) and is not performing to specification.

Since the Lido channel is approximately 900 m wide, it is obvious and readily seen in Figure 5.6 that the radar system is not providing adequate, overlapping coverage of the channel from both stations. Overlapping coverage of the measurement area is necessary to resolve the two dimensional velocity of the surface current. Without this, it is only possible to obtain radial component current measurements from each radar station.

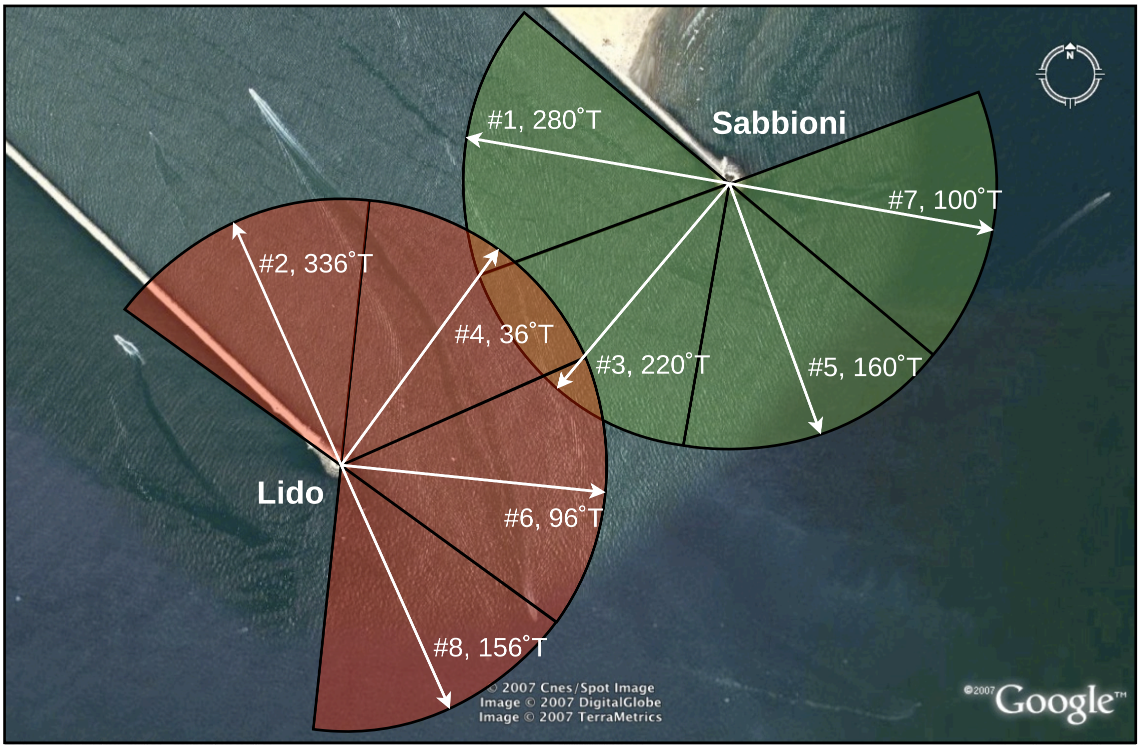

Figure 5.6 Estimated Maximum Radar Range
(Image map courtesy of Cnes/Spot, DigitalGlobe, TerraMetrics and GoogleEarth)

In order to obtain surface current measurements within the channel, we can make the assumption that the current flow within the channel is constrained in the direction of the axis of the channel (toward the lagoon, 316˚). From this, if a region of interest is sufficiently within the channel, the radial velocity obtained from the radar measurement can be resolved in the direction of the channel. This limits our use of the radar data to that obtained from the first two look directions, up the channel (280˚ and 336˚) and across the channel (220˚ and 036˚). The next section explains how surface current measurements are obtained for the channel using a combination of PMAP2DAT and additional MATLAB software.

5.2 Radar Analysis - PMAP2DAT Direction Finding

An Ocean Surface Current Radar can resolve azimuth direction by either of two methods, beam-forming or direction finding. The use of direction finding to resolve the azimuth of received backscatter signals from the ocean is described by Barrick et al. (1977). Direction finding techniques are also described in more detail in Section 5.6 which presents the development of the DFind direction finding algorithm. In this section, we describe the use of the PMAP2DAT post-processing utility which uses direction finding techniques to derive surface current measurements from the binary (.SORT) time-series data.

5.2.1 PMAP2DAT Direction Finding

According to processing parameters specified by the user, PMAP2DAT obtains current measurement data from the binary (.SORT) time-series data recorded by the PortMap radar. This process is performed sequentially in three stages by batch processing files, as specified by the user. These stages include the generation of direction finding radial currents, the re-gridding of these radials onto user specified gridpoints, and the conversion of these results into ASCII .dat files to be imported into other software packages.

For each acquisition file, the direction finding algorithm uses Fast Fourier Transforms to create a 2048 point frequency spectrum for each range of the 2048 time-series samples recorded from each antenna receiver. A weighted sum of the power spectrum for all the antennas is created and then smoothed. A representation of this spectrum is shown in Figure 5.7.

This summed power spectrum is used to determine the location of the Bragg peaks within the spectrum. The Bragg peaks are identified and classified by the amount of energy contained in the peaks found, and whether the peaks are above a pre-determined noise threshold. Various other methods are also employed in PMAP2DAT to compare peaks, including comparisons between peaks either side of 0 Hz.

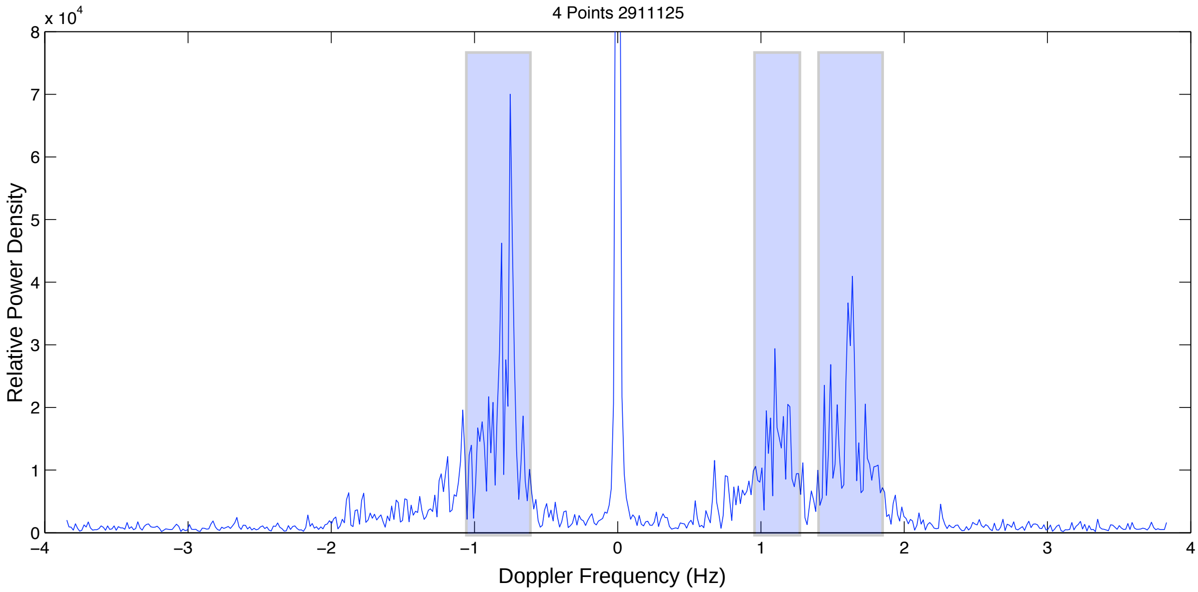

Figure 5.7 Example power spectrum with Bragg peaks of interest

Once the Bragg peak locations are identified in the spectrum, the algorithm uses these frequency bounds to process the original spectrum from each antennae. Within a Bragg peak region of interest, direction finding techniques are used to identify the azimuth of origin for each frequency spectrum point. This uses the properties of the linear antenna array, together with the I and Q values obtained for each antenna spectrum to 'steer' the array. The azimuth angle is the angle at which the signal magnitude is a maximum. Each frequency point that is processed using direction finding has an azimuth angle and a corresponding radial velocity as per the Bragg wave equation (2.7). The measurements are all collated into range radials, i.e. radial measurements for each range cell. These range radials are written to an interim binary file to be processed by the re-gridding operation.

5.2.2 Re-gridding Radial Currents

The second processing stage re-grids the range radials obtained for each range cell onto a grid of latitude and longitude coordinates, as specified by a user gridpoint file. For the Venice deployment, a cartesian coordinate system with the Sabbioni station at the origin was chosen for the re-gridding of the radials.

A 100 m square grid for each radar station is used to re-grid the radial velocities. As discussed in Section 5.1, this is restricted to points within the channel where it is assumed that the current flow is constrained to the direction of the axis of the channel. Grid points that are at angles ill-conditioned for resolving the radial current in the direction of the channel are removed. Points excluded were within +/- 15° of a line perpendicular to the channel direction passing through each radar station. Points where the current was not considered to be constrained within the channel were also excluded. The resulting 100 m grid for each station is shown in Figure 5.8.

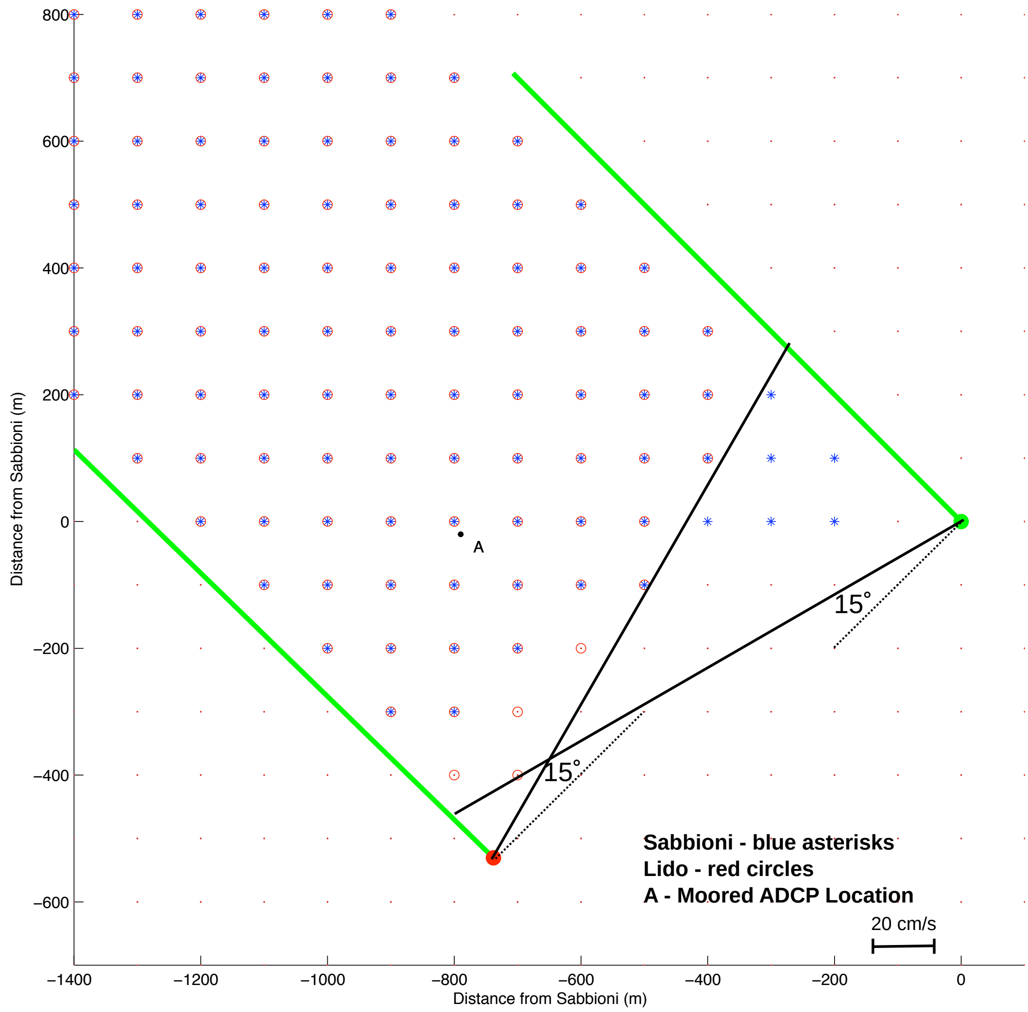

Figure 5.8 Channel Grid points for Sabbioni and Lido

This linear grid was translated into the required coordinates of latitude and longitude using spherical trigonometry (great circles). A diagram representing the geometry used for this is shown in Figure 5.9.

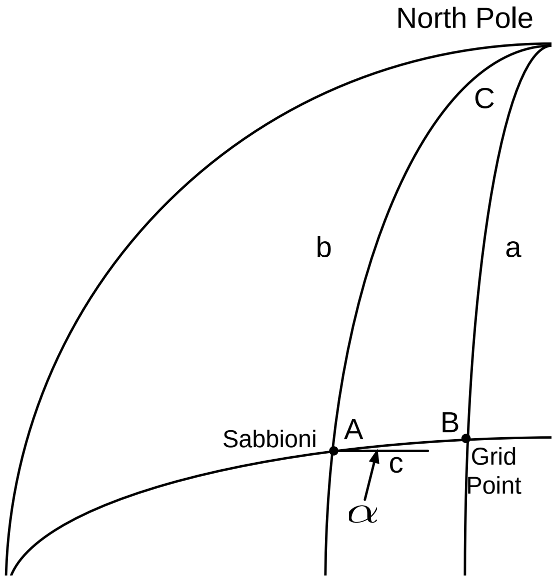

Figure 5.9 Spherical Trigonometry for Latitude/Longitude Conversion

Assuming that the distance between Sabbioni and a selected gridpoint is considered small in relation to the radius of the earth, we can use a great circle passing through the Sabbioni station and the gridpoint to calculate the latitude and longitude of the gridpoint.

Using the spherical trigonometry formulae

$$\cos(a) = \cos(b)\ \cos(c) + \sin(b)\ \sin(c)\ \cos(A) \quad (5.1)$$

$$\frac{\sin(A)}{\sin(a)} = \frac{\sin(B)}{\sin(b)} = \frac{\sin(C)}{\sin(c)} \quad (5.2)$$

let *b* = Latitude of Sabbioni,

the radius of the earth, *Re* = 6371000 km

and *channelx* and *channely* represent the X and Y distance from Sabbioni.

Now,

$$A = \pi/2 - \alpha \qquad (5.3)$$

where

$$\alpha = \tan^{-1} \frac{channely}{channelx} \qquad (5.4)$$

If *channelx* is less than zero then $\alpha = \alpha + \pi$

The angle *c* (radians) is given by

$$c = \sqrt{channelx^2 + channely^2}/Re \qquad (5.5)$$

and equation (5.1) can now be used directly to solve for *cos(a)*.

Using this result,

$$a = \cos^{-1}[\cos(a)] \quad \text{and} \quad \sin(a) = \sqrt{1 - \cos^2(a)} \qquad (5.6, 5.7)$$

Now, using Equation (5.2), we may solve for *sin(C)* :-

$$\sin(C) = \frac{\sin(c)\ \sin(A)}{\sin(a)} \qquad (5.8)$$

The latitude and longitude of the selected gridpoint are thus given by :-

$$GridPointLat = a \qquad (5.9)$$

$$GridPointLong = LongSab + C \qquad (5.10)$$

A MATLAB script was used to generate a separate gridpoint file (.grid) containing the Latitudes and Longitudes of the gridpoints for each radar station.

PMAP2DAT now re-processes the radial currents obtained for each range cell and performs an inverse distance weighted sum of the radial velocities within a region surrounding each gridpoint contained in each station's respective .grid file. Once processed, these gridpoint radials are output to a second interim binary file.

5.2.3 Archiving Data

The final processing step takes the radial currents for each of the specified gridpoints, and outputs these to an ASCII .dat file. These files consist of gridpoint coordinates relative to the origin (Sabbioni Station), surface current speed (m/s) and bearing (degrees East of True North). This file format is suitable for importing into other software tools such as MATLAB. MATLAB is used for all further analyses. Figure 5.10 shows an example of a radial current map generated by MATLAB using an archived radials file produced by PMAP2DAT.

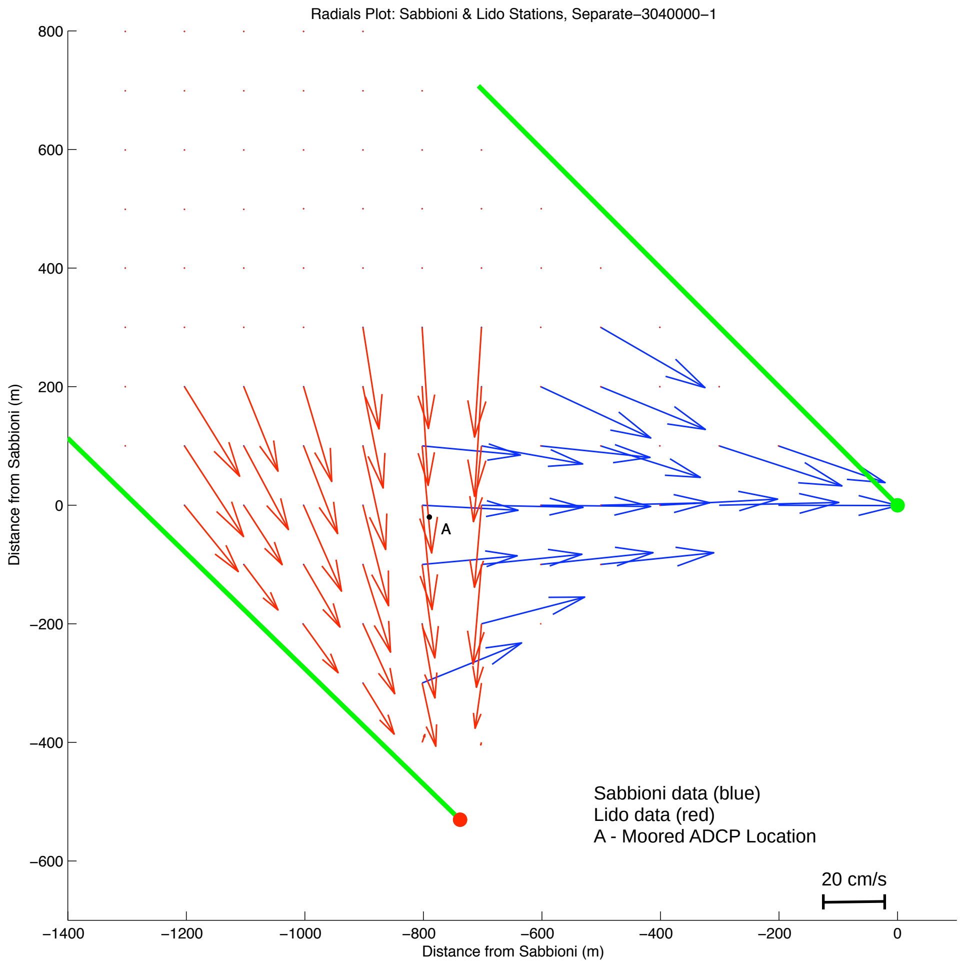

Figure 5.10 Radial Current Map

5.2.4 Channel Currents

The radial current measurements obtained using PMAP2DAT are now further processed to obtain the surface current within the channel. As shown in the section on radar quality in Section 5.1, there is not adequate overlapping coverage of the channel from both stations. We make the assumption that if the region of interest is constrained within the channel, then the surface current is in the direction of the axis of the channel. We can therefore use the radial component current measurements to determine the channel current.

The channel current is determined as follows. A radial current measurement for a gridpoint can be used to determine the channel current at that point. Using the diagram shown in Figure 5.11, the channel current resolved in the direction of the radial can be written as

$$V_{radial} = V_{channel} * \cos(\theta) \tag{5.11}$$

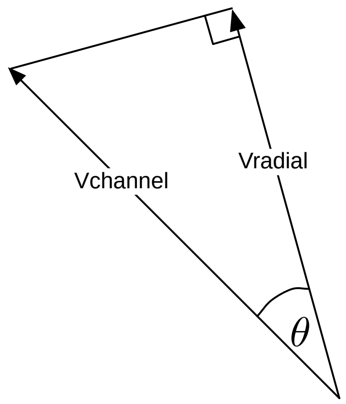

Figure 5.11 Channel Current with Radial Component

Now, taking the positive channel current to be in the direction of a flood tide (i.e. 316°) we can evaluate θ as the difference between the radial current direction and the channel axis direction as

$$\theta = \theta_{radial} - \theta_{channel} \tag{5.12}$$

Therefore, the magnitude of the channel current is given by

$$V_{channel} = \frac{V_{radial}}{\cos\left(\theta_{radial} - \theta_{channel}\right)} \tag{5.13}$$

where a positive value for $V_{channel}$ is a current towards the lagoon (flood current).

Solving for the channel current, $V_{channel}$ in equation 5.13 can become ill-conditioned as the difference between the radial angle and the channel direction approaches 90°. To prevent this from occurring, channel gridpoints that would create a difference angle greater than 75° were removed from the grid as shown previously in Figure 5.8.

This process is performed for each radial current velocity produced by PMAP2DAT to create a vector map of currents within the channel. Figure 5.12 shows the channel currents for the corresponding radials that were processed by PMAP2DAT in Figure 5.10.

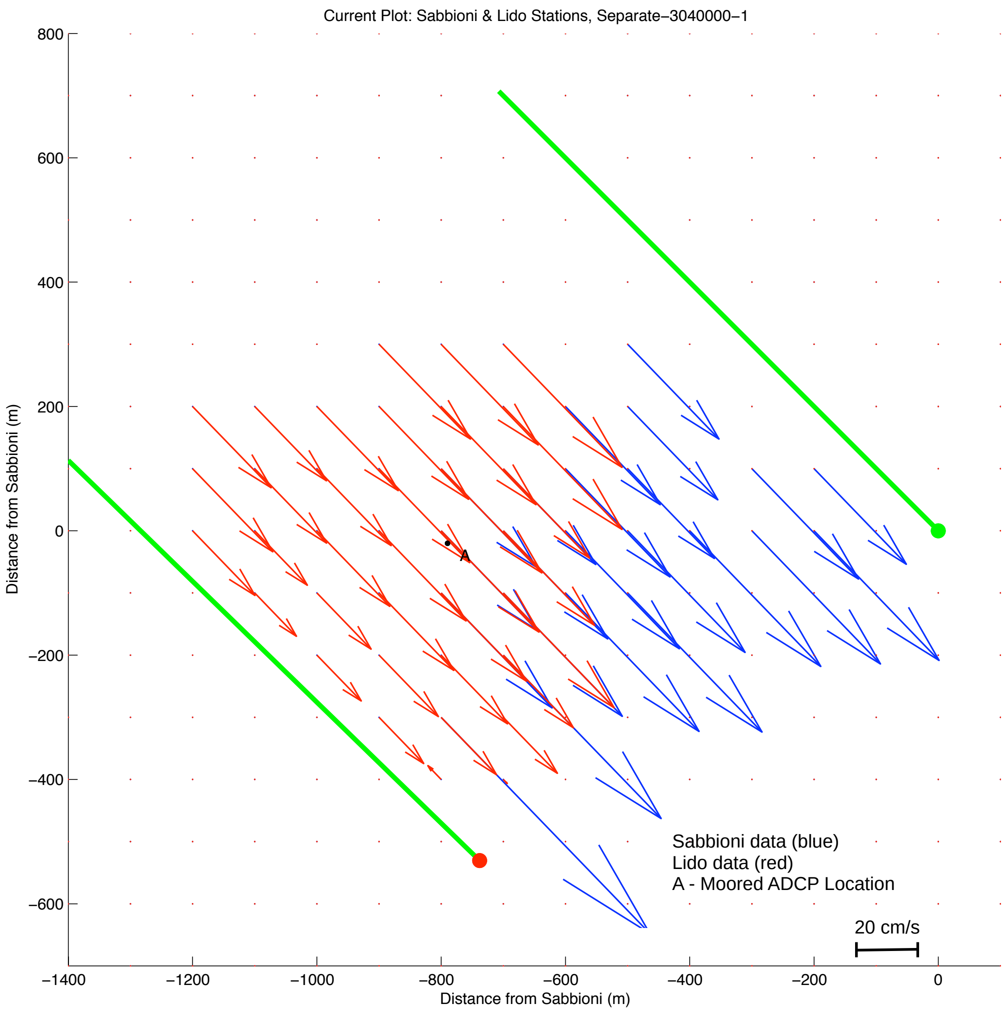

Figure 5.12 Channel Currents derived from Radial Measurements

5.2.5 Development of User Interface

A large quantity of data was produced from the six week deployment. To efficiently process and analyse this data, batch processing for PMAP2DAT was used together with a graphical user interface (GUI) developed in MATLAB to perform the above operations.

Once the entire data set had been batch processed using PMAP2DAT to produce radial current data files, the "CurrentsGUI" user interface was used to visualise and scroll through current vector maps from any date or time within the data series.

A screenshot of "CurrentsGUI" shown below in Figure 5.13 shows the interface, and the controls used to view the current data. As will be described in Sections 5.4 and 5.5, this tool was further developed to process sequences of vector maps for producing time-series of average current measurements within a 200 m radius of the ADCP location and for creating a channel transect of surface currents.

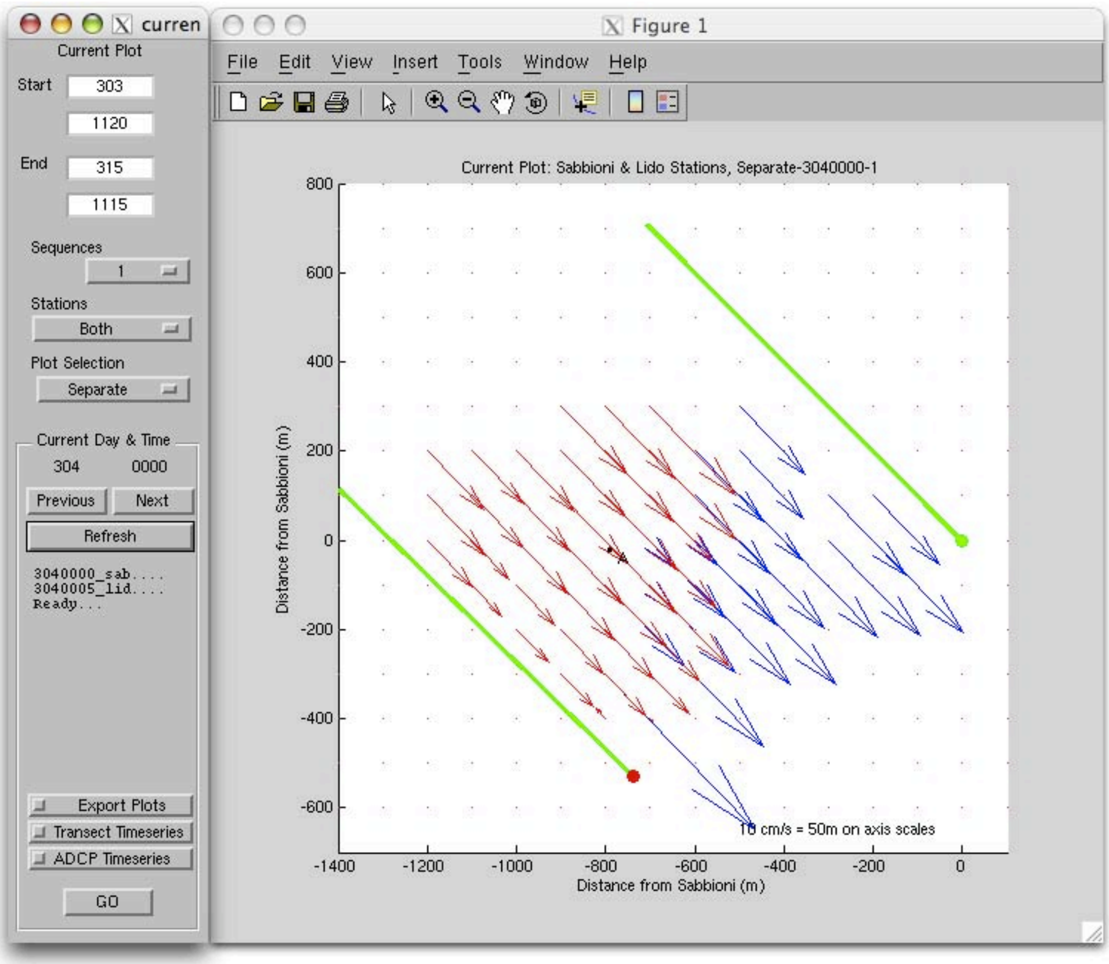

Figure 5.13 CurrentsGUI Graphical User Interface

5.3 Spatial Separation Correlation - Radar Spectra

In order to verify the range resolution of the radar system, an exercise was undertaken to observe the correlation between beam-formed radar spectra at a number of points within a region that spanned multiple range cells.

From Lido time-series data, radar spectra were generated using beam-forming to each location of a 25 point grid covering 250 x 250 m. The spacing of the points on this grid is 50 m in both the x and y direction, as shown in Figure 5.14.

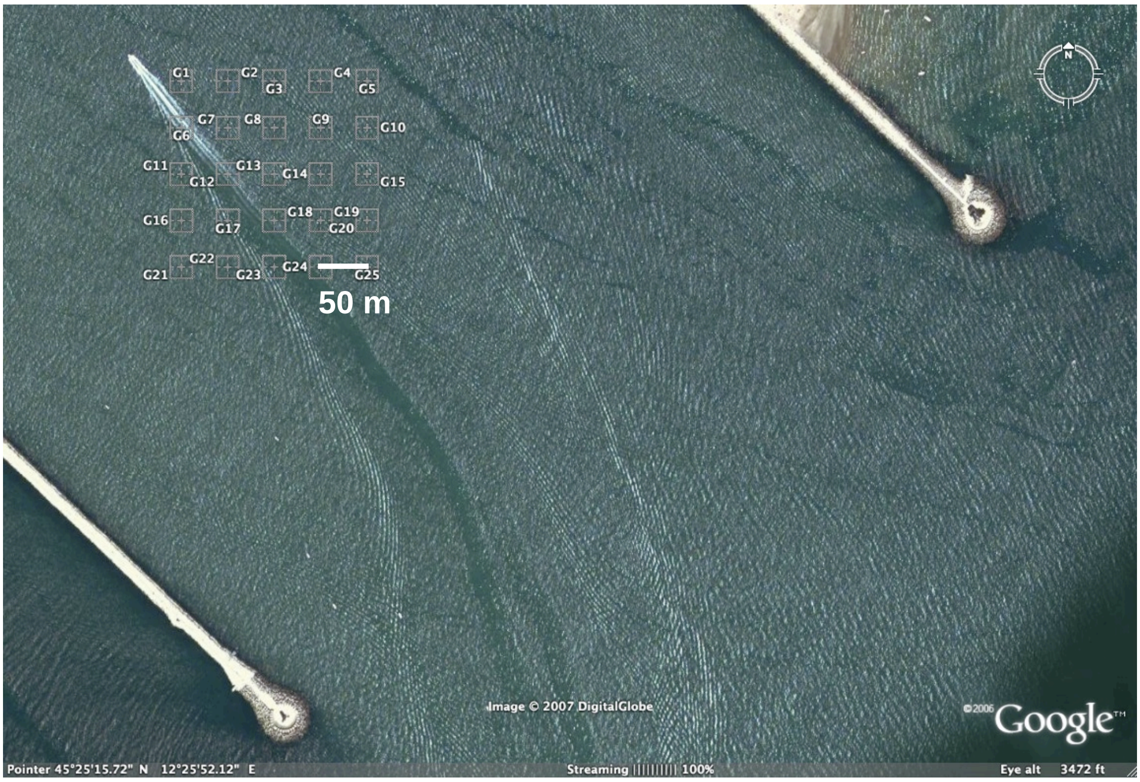

Figure 5.14 25-Point Correlation Grid Locations
(Image Map courtesy of GoogleEarth and DigitalGlobe)

A radar spectrum was produced for each point on this grid by using beam-forming techniques. The spectra were produced using a DC filter on the antenna time-series signals to eliminate any strong 0 Hz spectral peaks.

Using the spectra for each point in the grid, the auto-correlation between all points was calculated as

$$\sum_k \frac{A_{ijk} * A^*_{ijk}}{n} \tag{5.14}$$

where *k* is the amplitude spectrum index, *i,j* are the spatial location coordinates, and *n* is the number of spectrum points in the complete sum (i.e. n = 2048 * 25).

Next, a correlation index was calculated using the spectrum and complex conjugate of the comparison spectrum for each value of increasing spatial separation. In this 5 x 5 grid, the spatial separation increases from 2 through to 4. For example, the calculation for a spatial separation of 1 is the sum

$$\sum_k \frac{A_{ijk} * A^*_{i+1,j,k}}{n}$$

$$\sum_k \frac{A_{ijk} * A^*_{i,j+1,k}}{n} \quad \text{, spatial step = 1} \tag{5.15}$$

and for increasing spatial separation, for example spatial step of 2

$$\sum_k \frac{A_{ijk} * A^*_{i+2,j,k}}{n}$$

$$\sum_k \frac{A_{ijk} * A^*_{i,j+2,k}}{n} \quad \text{, spatial step = 2} \tag{5.16}$$

The values obtained using these correlation functions for spatial step from 1 to 4 are plotted against spatial step number. The resulting plot of spatial separation correlation obtained for the 25 point grid spectrum data for a chosen day and time (DAY291, 1205) is shown in Figure 5.15 below. Although very coarse, this plot shows that the spectral correlation for adjacent points diminishes with increasing distance of separation. It must be noted too that no distinction is made between the correlation in the direction of range or azimuth.

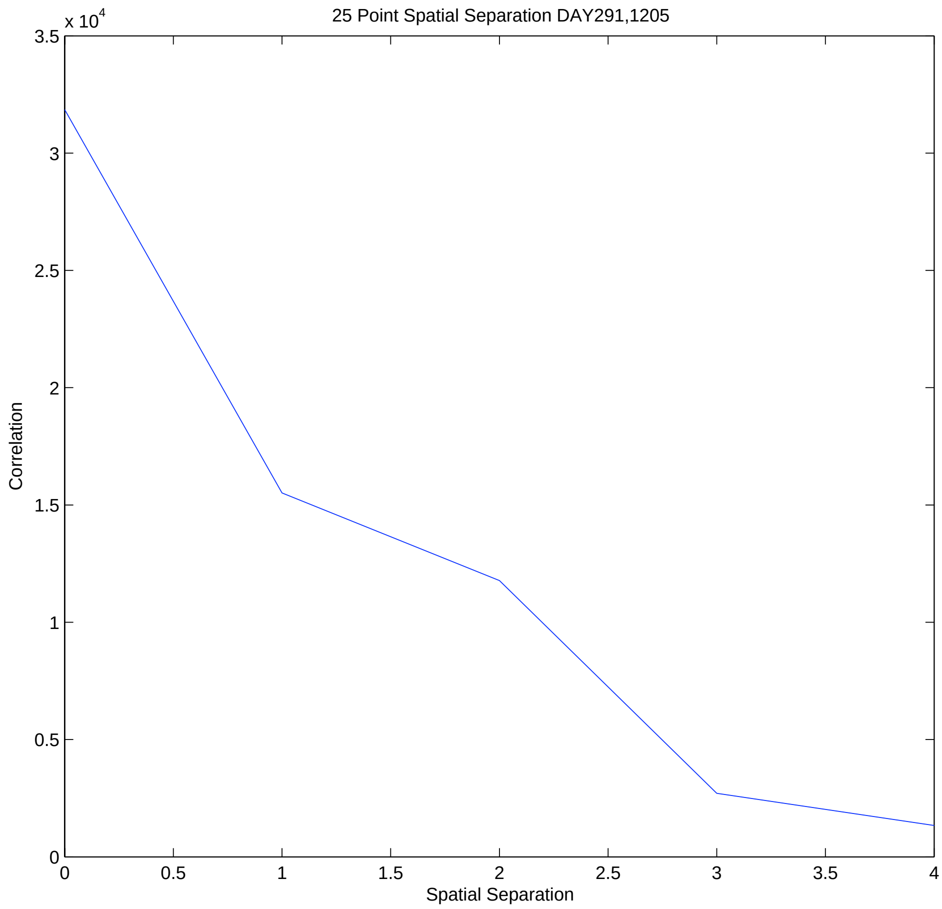

Figure 5.15 25 Point Spatial Separation Correlation

A modified approach was undertaken to overcome the limitations of using only 25 points in the comparison. It was also considered that high current shear may exist between the gridpoints on the coarse 25 point grid (50 m spacing) so a new grid was used with additional gridpoints placed on a 10 m spacing within the existing grid. Over the same region of interest, beam-formed radar spectra were obtained for each of the 441 gridpoints on this fine scale grid. The spatial step correlations were also calculated and plotted separately for increasing separation in the direction of range, and for across the azimuth. Using the same data as before, the correlation values for the 441 point grid are shown in Figure 5.16 below.

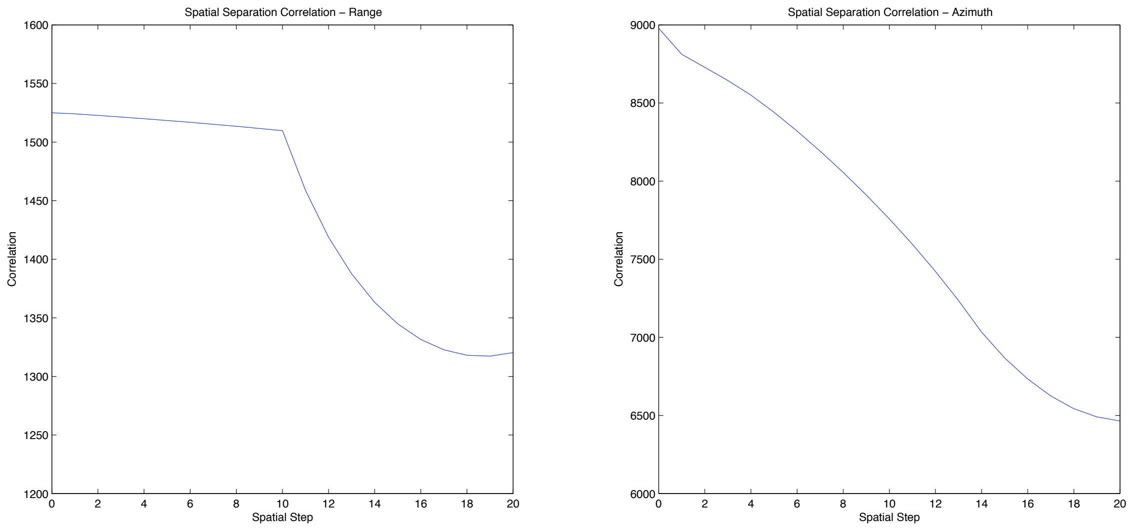

Figure 5.16 441 Point Spatial Separation Correlation

We can see from the first graph in Figure 5.16 that the spectral correlation in the direction of range for spatial steps 1 through 10 declines slightly. The correlation then decreases rapidly for spatial separation steps above 10. As the gridpoint spacing chosen was a tenth of the range resolution of the radar, this shows that the range resolution of the system is indeed dictated by the bandwidth and is 100 m.

From the second plot, we see that the correlation in the direction across the azimuth decreases with increasing spatial separation.

5.4 Averaging GridPoint Radar Measurements

The surface current maps within the channel, as obtained in Section 5.2 can be further processed to provide secondary current data for regions within the channel. In this section, we create an average surface current measurement for a circular zone of the channel surrounding the deployed ADCP. This will allow the comparison of radar current measurements within this zone with those obtained by the ADCP.

5.4.1 ADCP Region Averaging

Surface current data from radar gridpoints within a 200 m radius of the ADCP location are used to create an average surface current measurement for the ADCP region. The region of interest is shown in Figure 5.17 by the circular dotted line surrounding the ADCP location marked as point A.

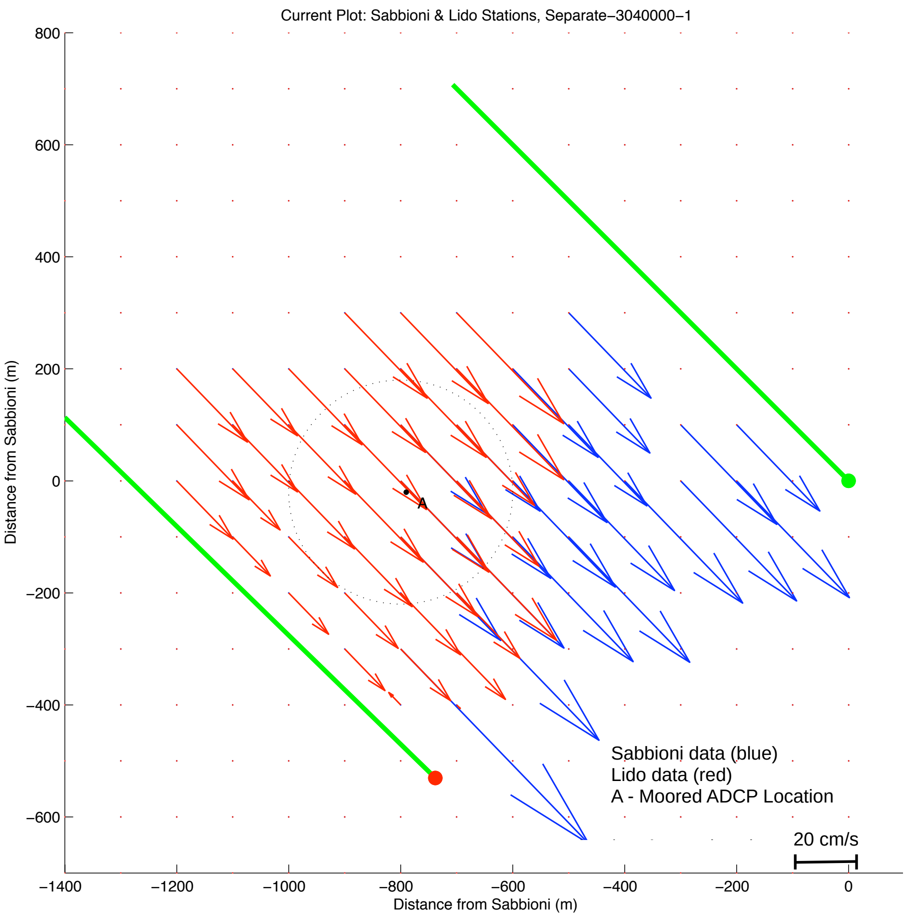

Figure 5.17 ADCP Region of Averaging

The mean and standard deviation are calculated for valid radar surface current measurements within the circular zone. Any data points having a surface current measurement differing in value more than twice the standard deviation from the mean are discarded. The remaining data points that are within twice the standard deviation of the mean are inverse-distance-weighted summed using the formula

$$\bar{Z} = \frac{\sum_{i=1}^{n} \frac{Z_i}{d_i^p}}{\sum_{i=1}^{n} \frac{1}{d_i^p}} \qquad (5.17)$$

where Z_i is the radar surface current at each valid data point, d_i is the distance of each data point from the origin (ADCP location), and p is the chosen weighting factor of 2.

The variance for the points used for this inverse-distance-weighted mean is calculated :-

$$S_z^2 = \frac{\sum_{i=1}^{n} \left[\frac{(Z_i - \bar{Z})^2}{d_i^p} \right]}{\sum_{i=1}^{n} \frac{1}{d_i^p}} \qquad (5.18)$$

where $\bar{Z}$ is the inverse distance weighted mean, as calculated using Equation 5.17. The standard deviation is obtained directly from the result obtained for the variance.

As an example, the mean current within the ADCP zone for the current vector map shown in Figure 5.17 above is calculated and then plotted in Figure 5.18.

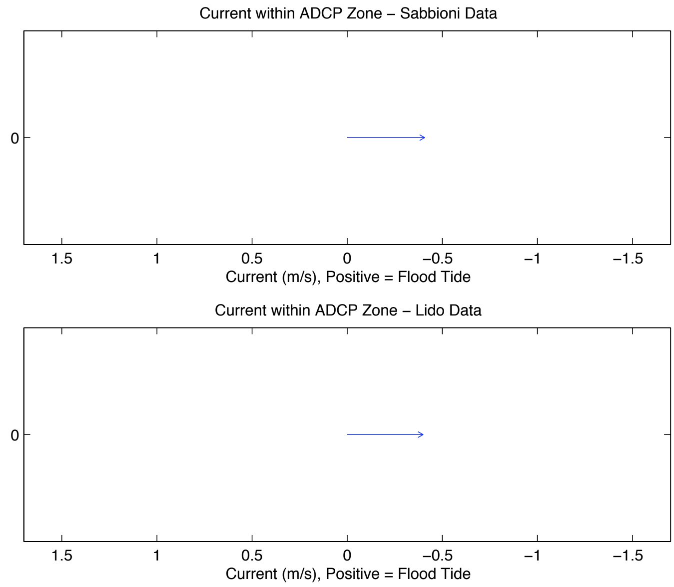

Figure 5.18 Average Channel Current within the ADCP Zone

The graphical user interface, "CurrentsGUI" uses the process shown above to calculate the inverse-distance-weighted mean for either a single current map, or sequentially for a range of current maps as specified by start day/time and end day/time. The software processes all the current maps within the chosen date/time range and produces an output file consisting of a time-series of ADCP region averages and corresponding standard deviations. A quality index which is the number of data points used to calculate the inverse-distance-weighted mean and standard deviation is also recorded.

The six week time-series obtained for the average channel current within the ADCP zone is shown in Figure 5.19. This plot shows the tidal level, ADCP zone current measured using Sabbioni Radar data and the Lido Radar data respectively. The ADCP zone average current signals are considerably noisy. The Sabbioni average current data is also noisier and has more discontinuities than that obtained using the Lido data. This is because the Sabbioni station has insufficient range to cover the ADCP region properly, as shown in Section 5.1.

The ADCP zone currents obtained from the radar current maps can now be compared with the ADCP measured currents for the bin closest to the surface (Bin 9) which is at a depth of 1 m. The scatter plot shown in Figure 5.20 shows that the results obtained using the radar do not correlate well with the ADCP results, and that the radar is consistently measuring lower current speeds than the ADCP.

5.4.2 Noise Reduction

An iterative process of binomial weighting and interpolation can be used on the ADCP zone time-series to reduce the noise in the signal. For each value in the ADCP zone time-series, a binomially weighted value can be calculated using the formula

$$U_i = \frac{u_{i-2} + 4u_{i-1} + 6u_i + 4u_{i+1} + u_{i+2}}{16}$$

where *i* is the index of the current time-series value. Now, if a binomially weighted value differs by more than 1 m.s^{-1} from the original value, the original value is discarded and replaced by an interpolated value being the mean of the adjacent points in the time-series.

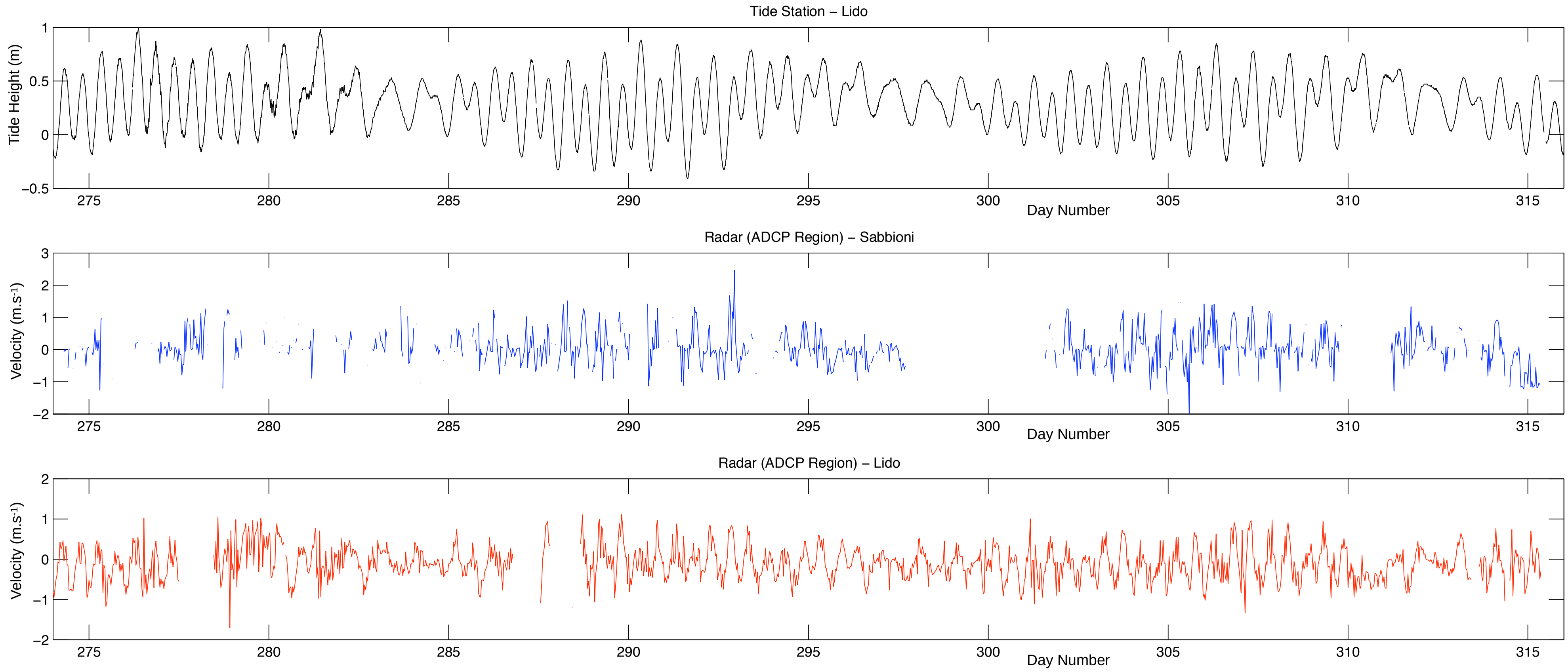

Figure 5.19 ADCP Zone Average Current Time-series
Current speed in the direction of the channel ($m.s^{-1}$)

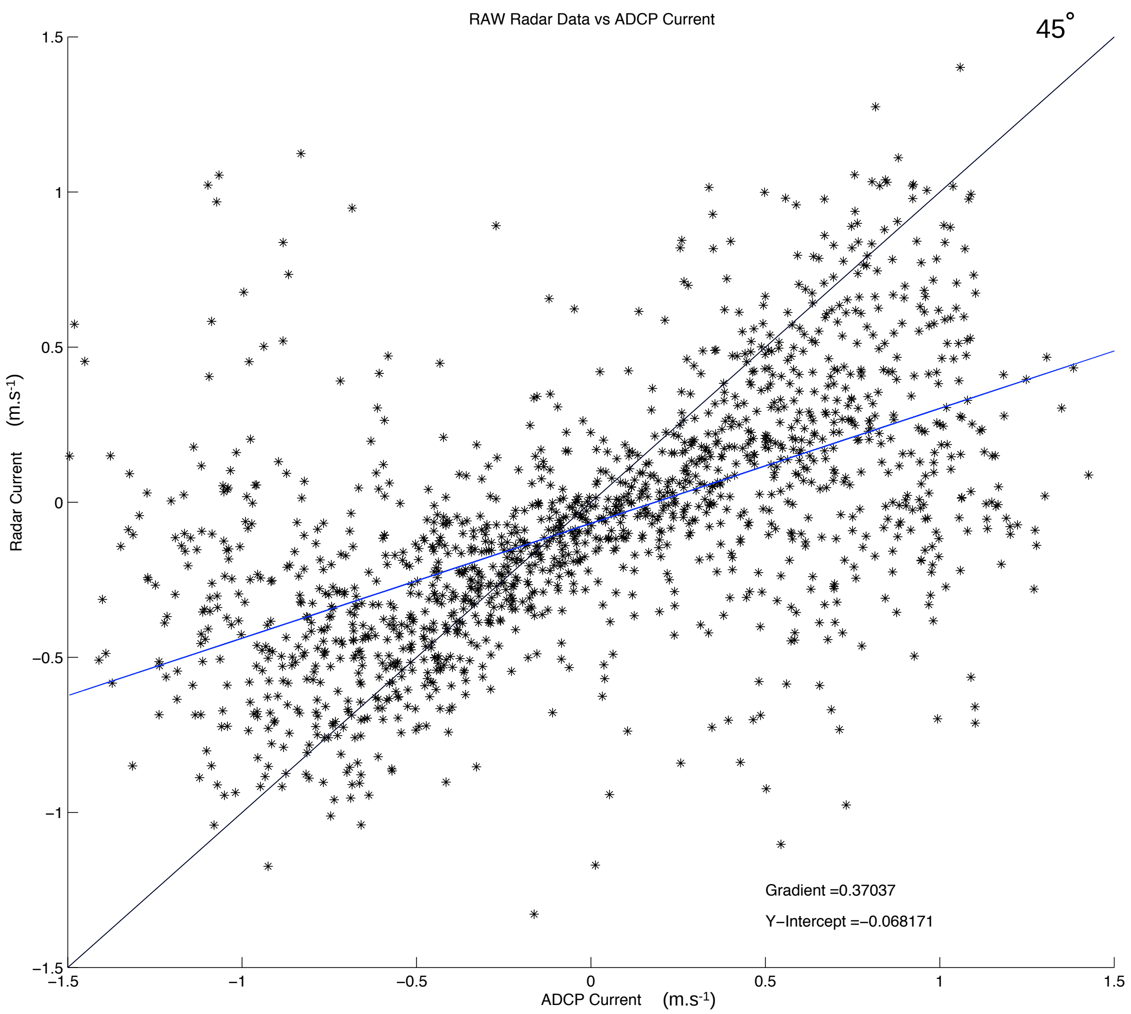

Figure 5.20 Radar Current (ADCP Zone) vs ADCP Current (Bin 9)

This binomial weighting and interpolation process is then repeated. This second time, a point in the first pass interpolated series is discarded if it differs by more than 0.3 ms^{-1} from the second binomially weighted value. Once points have been removed and interpolated a second time, the final output is a binomially weighted smooth curve.

This process is summarised in the flow chart shown in Figure 5.21, with the resulting processed time-series for the ADCP zone radar current data shown in Figure 5.22 on the following page.

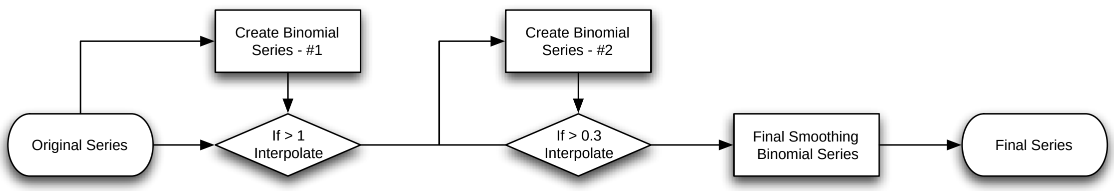

Figure 5.21 Binomial Weighting and Interpolation Algorithm

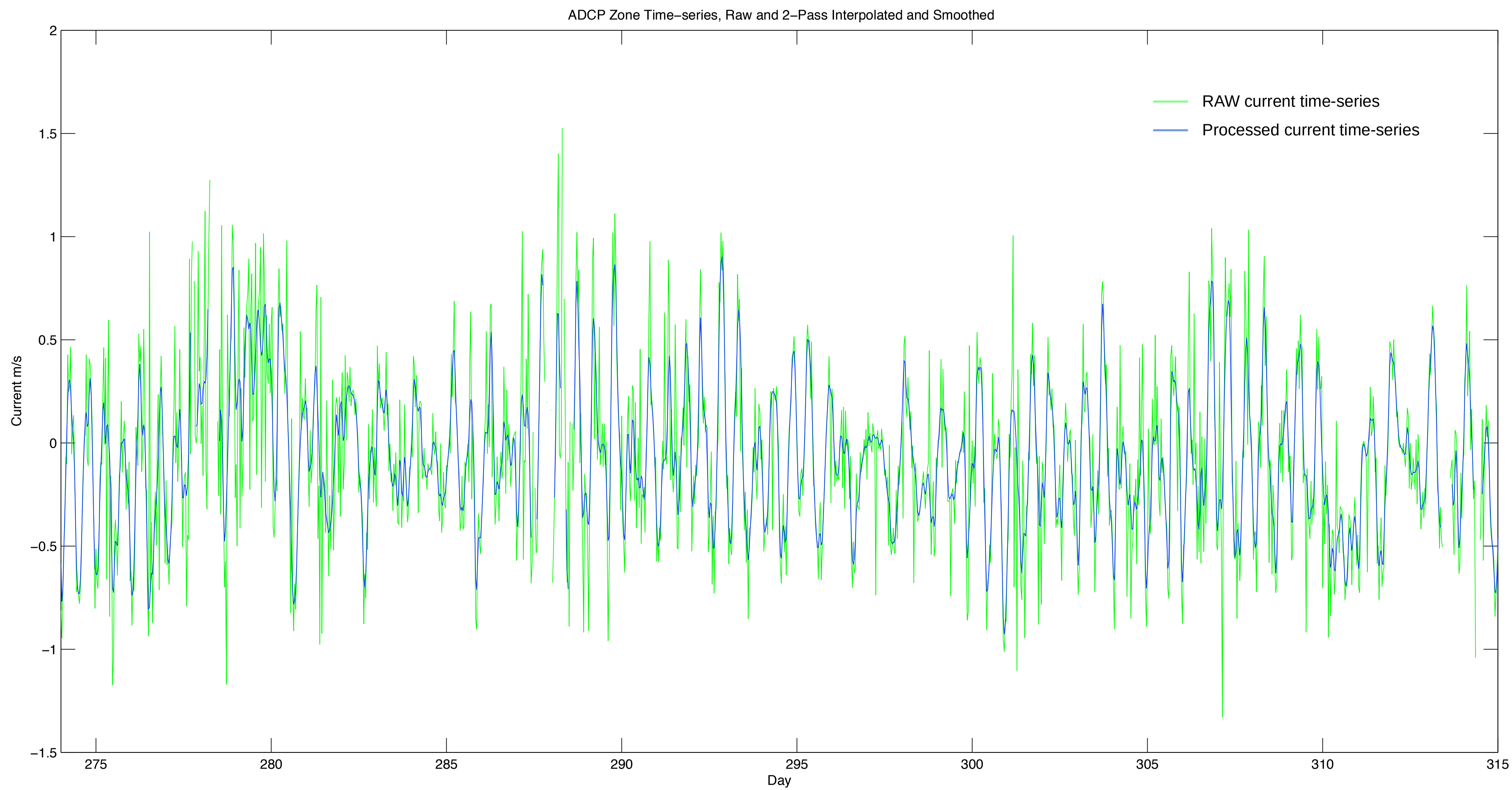

Figure 5.22 ADCP Zone Average Current Time-series - RAW and Processed

Comparing the interpolated and smoothed ADCP zone radar currents with those measured by the ADCP reveals that although we have reduced the noise in the radar current signal, the radar is still consistently reporting lower current speeds than the ADCP. The variation between the two instruments also increases for ADCP current speeds greater than 0.5 m.s^{-1}.

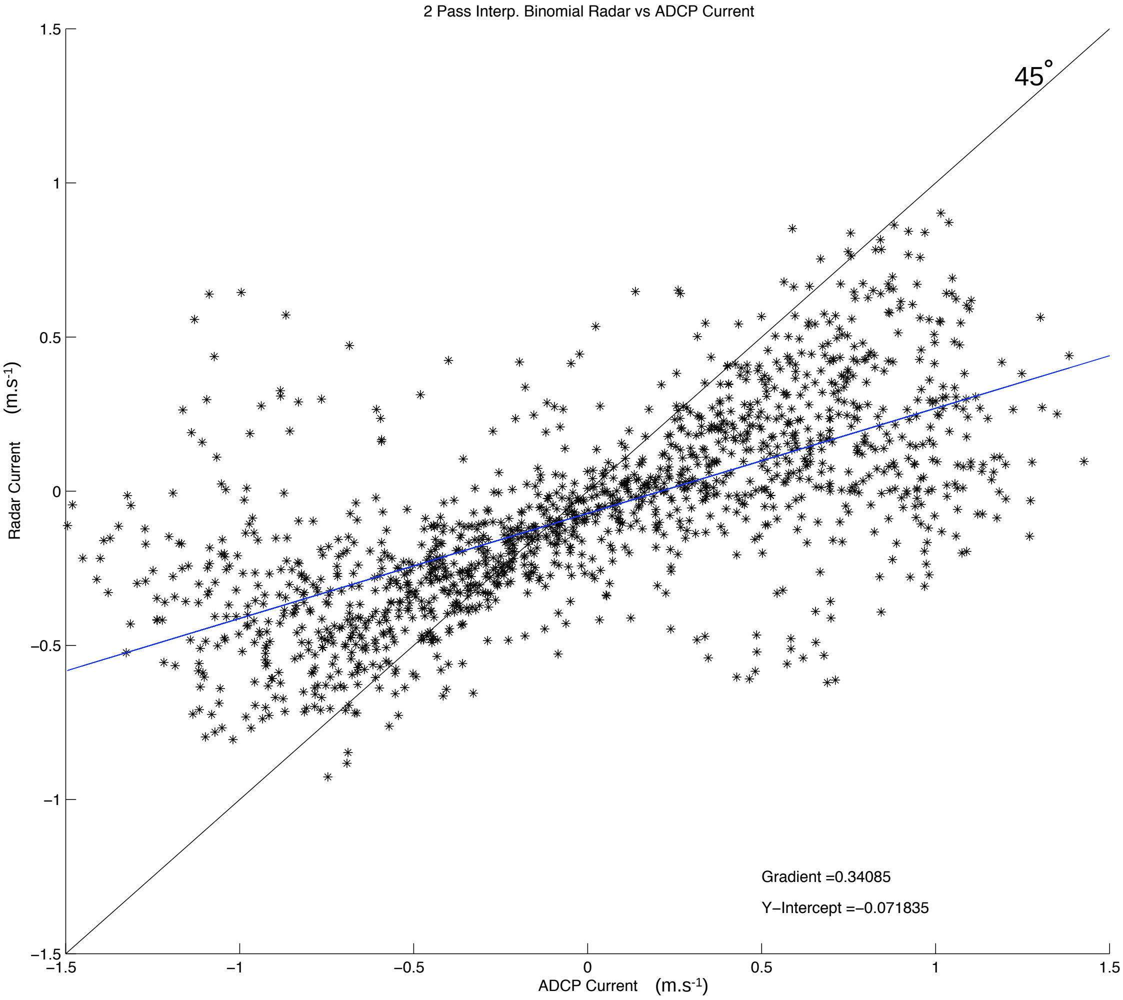

Figure 5.23 Interpolated/Smoothed Radar Current (ADCP Zone) vs ADCP Current (Bin 9)

5.5 Generating Three Dimensional Transects

In this section, we describe the processing of surface current measurements obtained from both the Sabbioni and Lido stations to create a surface current velocity profile across a transect of the Lido inlet. This transect profile can be combined with the ADCP current data to provide three dimensional profiling of currents within the Lido channel.

5.5.1 Transect Averaging

The method used for transect averaging is similar to the ADCP region averaging presented in Section 5.4. Average surface current measurements along the transect are calculated using data from points within a rectangular zone surrounding each transect point. The transect used aligns with the ADCP location in the middle of the channel, as shown by the thick blue line crossing the channel in Figure 5.24.

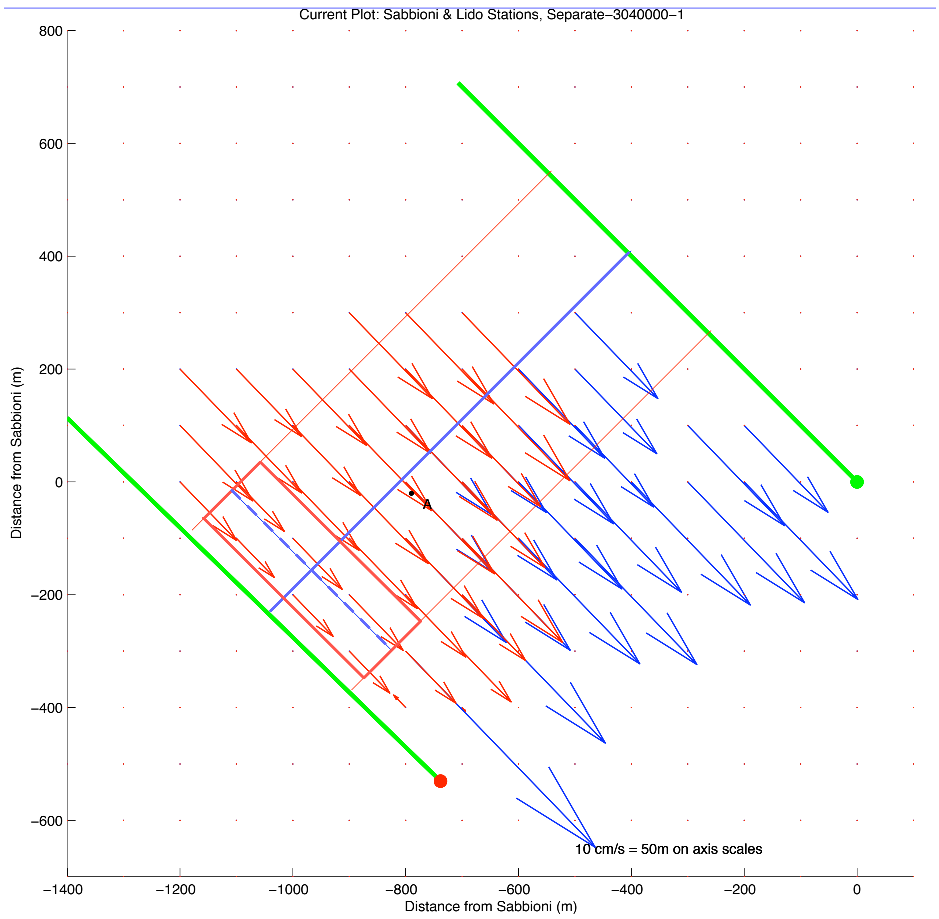

Figure 5.24 Channel Transect - Averaging Region

Points spaced 100 m apart along the transect are used as the centre points for the average current calculation. For each of these points, a rectangle is formed which is bounded by parallel lines 200 m either side of the transect line, together with lines in the direction of the channel, 70.7 m either side of the transect point. This geometry is shown below for the second point along the transect (Figure 5.25).

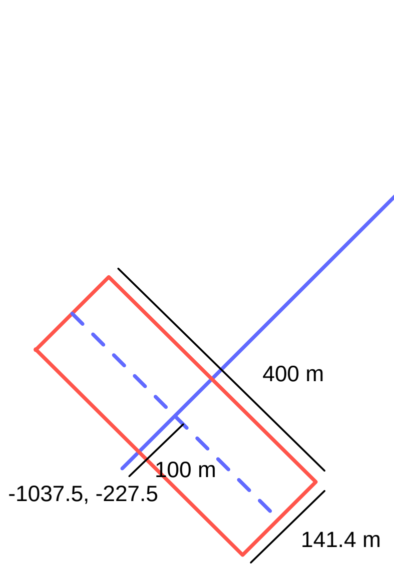

Figure 5.25 Transect Bounding Box Geometry

The algorithm for generating the transect profile takes the vector map points as shown in Figure 5.24. A subset of data points is created that are within 200 m perpendicular distance to the transect line. This subset is then sequentially processed for each point along the transect to identify data points that are within 70.7 m perpendicular distance to a vector in the direction of the channel that passes through the selected transect point. The determination of perpendicular distance in each case is calculated using the vector method below.

For three points, P1 (x_1, y_1), P2 (x_2, y_2), P3 (x_0, y_0) as shown in Figure 5.26, the perpendicular distance, *d* can be calculated using a vector method.

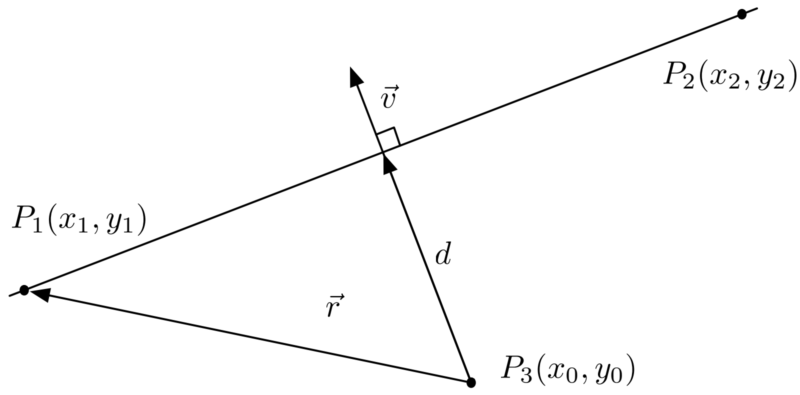

Figure 5.26 Vector Method for determining perpendicular distance

If the line is specified by two points, P1 and P2, then a vector $\vec{v}$ perpendicular to the line is given by

$$\vec{v} = \begin{bmatrix} y_2 - y_1 \\ -(x_2 - x_1) \end{bmatrix} \tag{5.19}$$

and the vector $\vec{r}$ is given by

$$\vec{r} = \begin{bmatrix} x_1 - x_0 \\ y_1 - y_0 \end{bmatrix} \tag{5.20}$$

Then the distance from P_3 to the line is given by projecting $\vec{r}$ onto $\vec{v}$, giving

$$d = |\hat{v} \cdot \vec{r}| = \frac{|(x_2 - x_1)(y_1 - y_0) - (x_1 - x_0)(y_2 - y_1)|}{\sqrt{(x_2 - x_1)^2 + (y_2 - y_1)^2}} \tag{5.21}$$

or

$$d = \frac{|det(P_2 - P_1 \;\; P_1 - P_0)|}{|P_2 - P_1|} \tag{5.22}$$

Once data points are identified within each rectangular section of the transect, the inverse-distance-weighted mean and standard deviation are then calculated using the inverse-distance-weighting formulae 5.17 and 5.18 from Section 5.4.

Figure 5.27 shows an example transect plot for the vector map shown in Figure 5.24. The first two plots show the transect processed using individual station data whereas the third plot shows the transect profile if current data from both stations is combined.

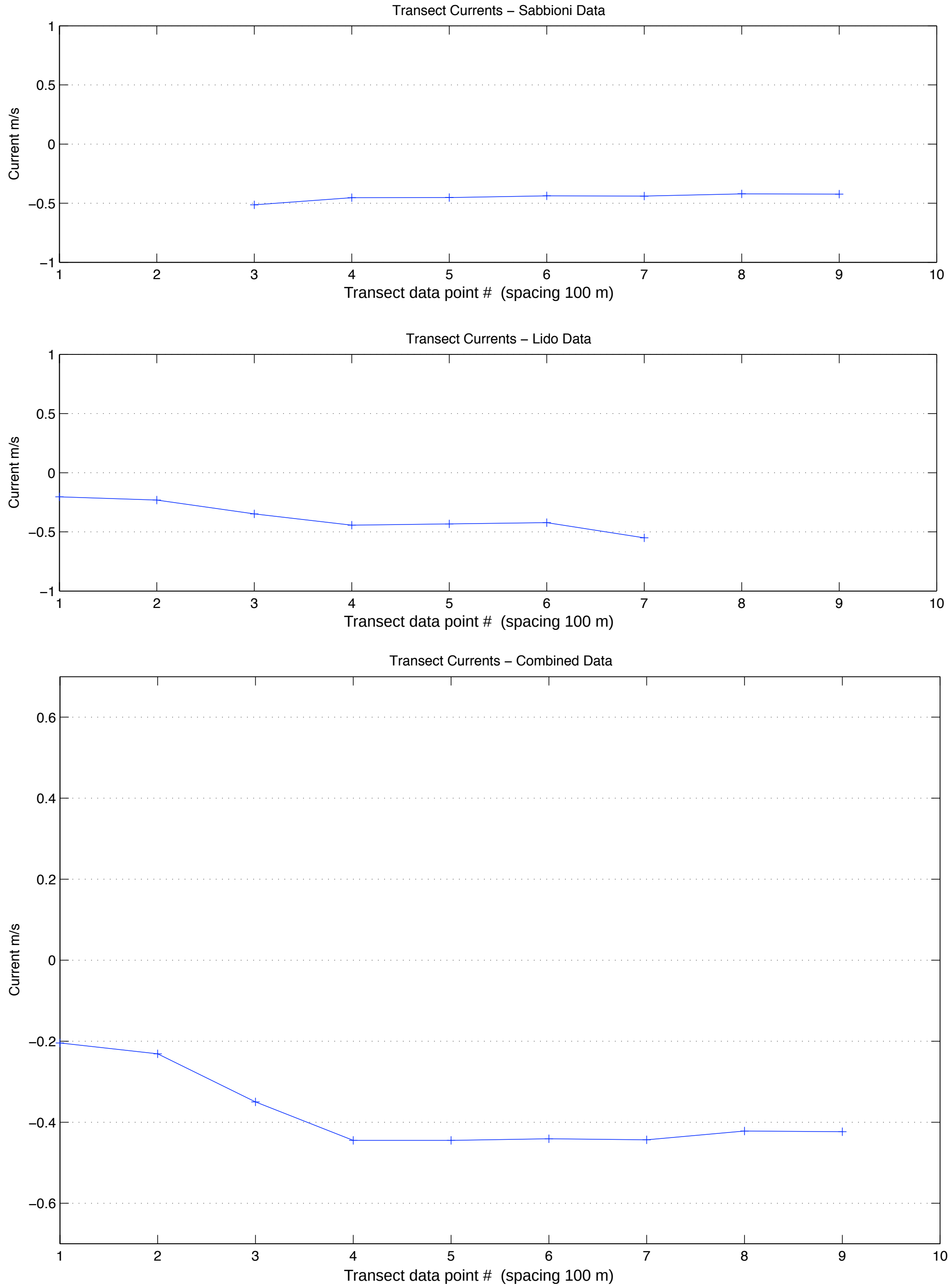

Figure 5.27 Transect Profile for Day 304_0000
(Transect data point # 1 is 50 m from Lido Breakwater)

Similar to the ADCP region averaging, the graphical user interface, “CurrentsGUI” is also used to implement the transect processing. It is used to produce a time-series of transect measurements between chosen dates and times. These time-series transect values may also be used together with the ADCP measurements and water depth profile to form a 3-Dimensional transect view such as that shown in Figures 5.28 and 5.29.

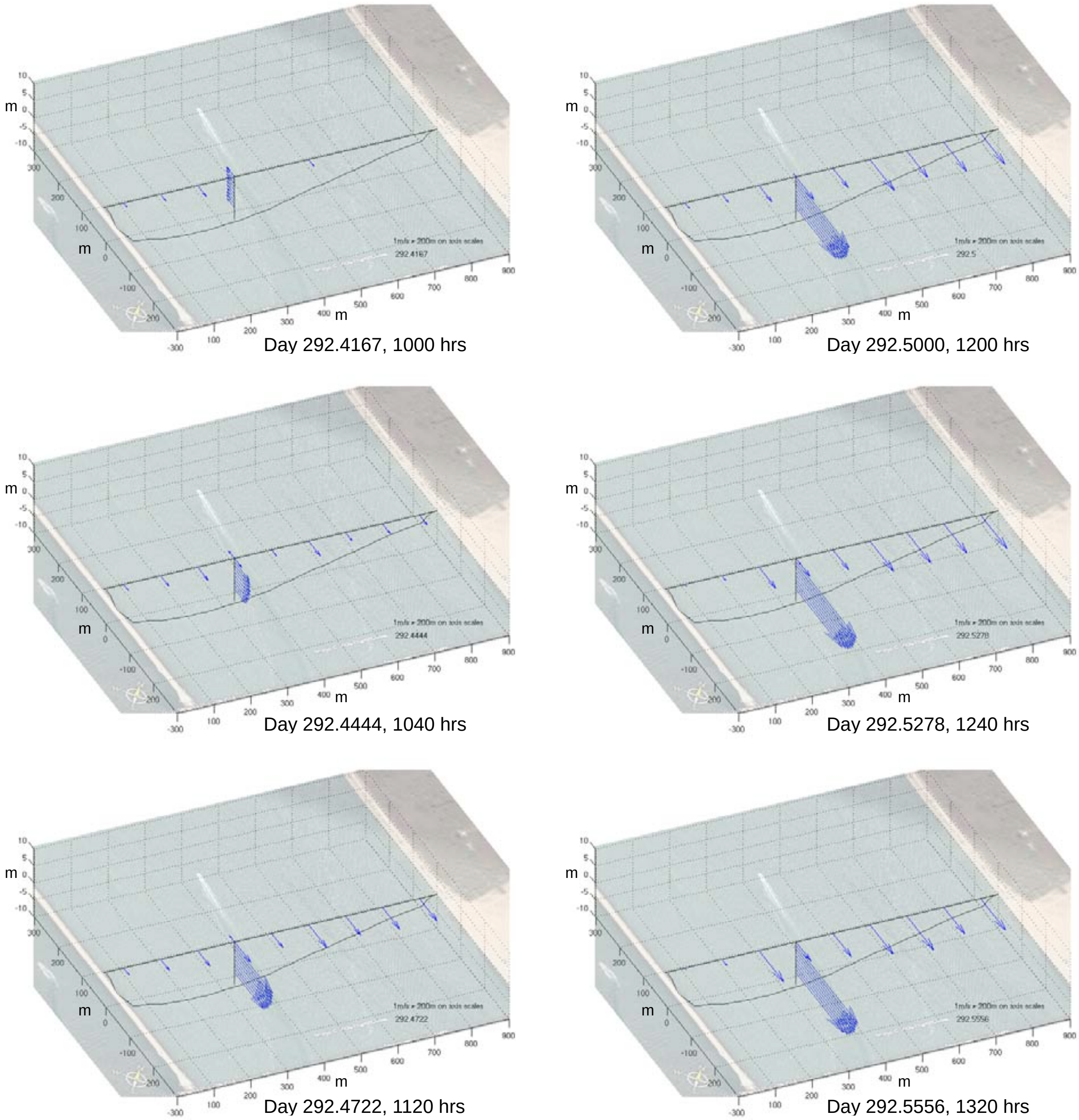

1 m.s^{-1} = 200 m on x-axis scale

Figure 5.28 3-Dimensional Transect view, Day 292.4167 - 292.5556
ADCP current vectors indicate the vertical profile at 400 m across the channel.
(Image Texture Map Courtesy of Google Earth)

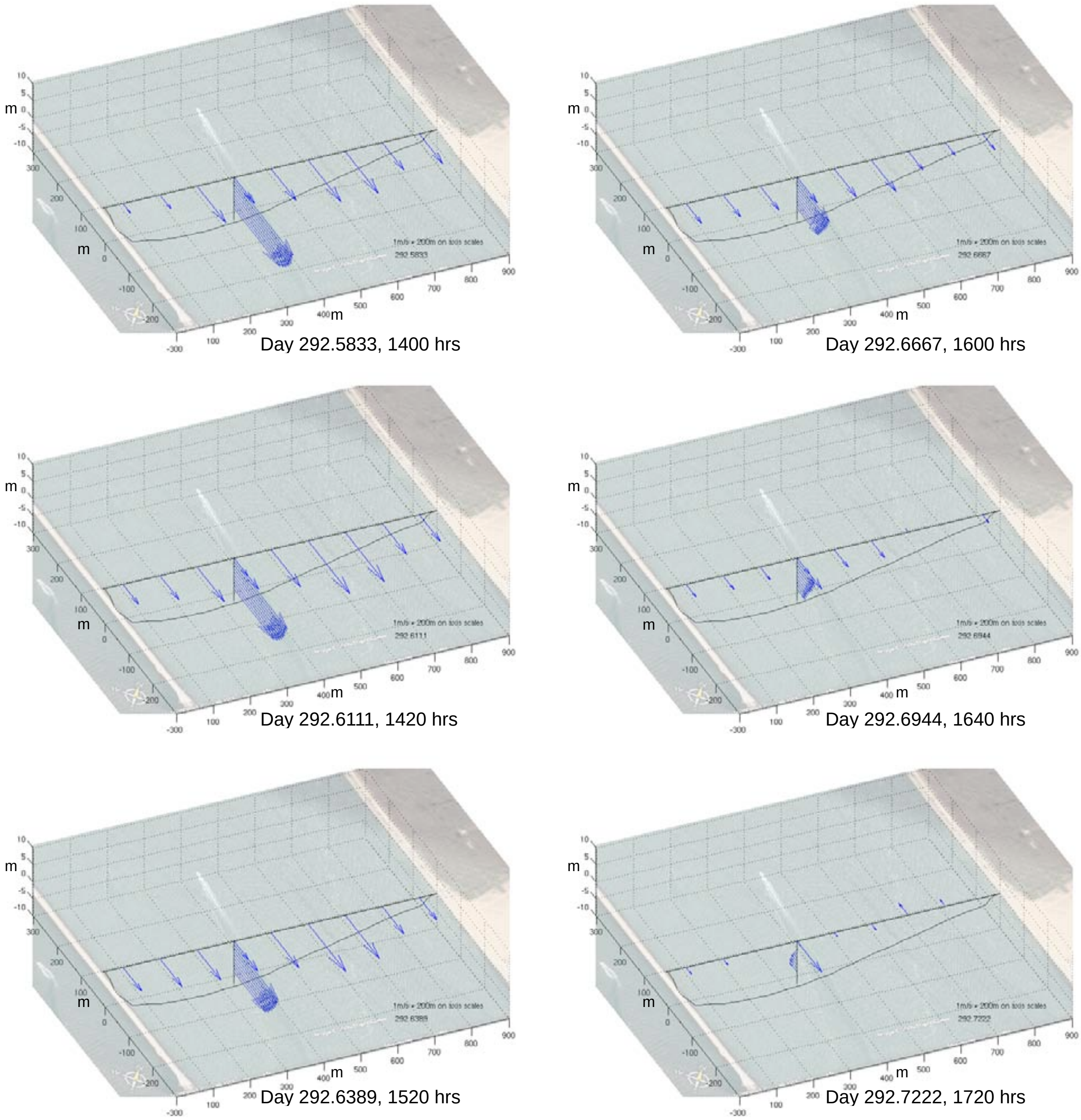

1 m.s^{-1} = 200 m on x-axis scale

Figure 5.29 3-Dimensional Transect view, Day 292.5833 - 292.7222
ADCP current vectors indicate the vertical profile at 400 m across the channel.
(Image Texture Map Courtesy of Google Earth)

The 3-Dimensional transect view clearly shows the transect surface current profile, the ADCP current profile and the bathymetry of the transect. It must be noted that the scale used for the vertical dimension is different from the horizontal dimensions.

The image sequence shown in Figures 5.28 and 5.29 is during a strong ebb tide during spring tides. In this sequence, when strong currents are measured by the ADCP, the radar is clearly seen to under-report the current velocity. This further shows the effect seen in the scatter plots presented in Section 5.4 where the radar measurements fail to correlate well with the ADCP for higher current speeds.

Using the same technique as for the ADCP zone averaging in Section 5.4, each time-series for individual transect points can be 2-pass interpolated and binomially smoothed. In Figure 5.30, the interpolated and smoothed average current for transect point 4 (300 m from Lido side) is compared with the ADCP current (Bin 9). This shows a similar result to that obtained for the ADCP region averaging. The spatial region used for each of these radar averages is centred approximately on the same location though a different shape.

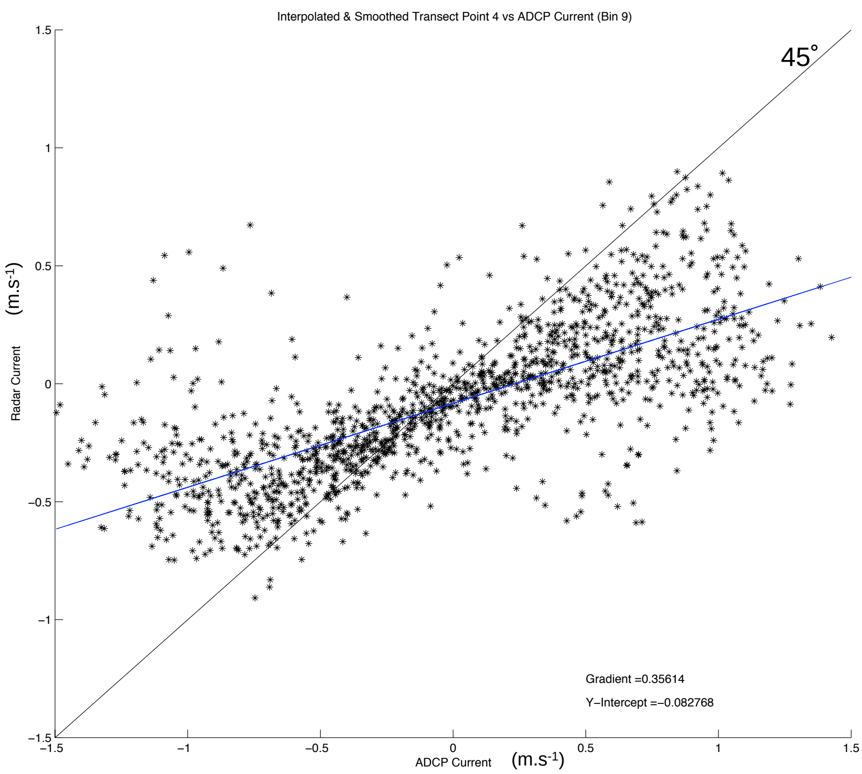

Figure 5.30 Transect Point 4 vs ADCP Current (Bin 9)

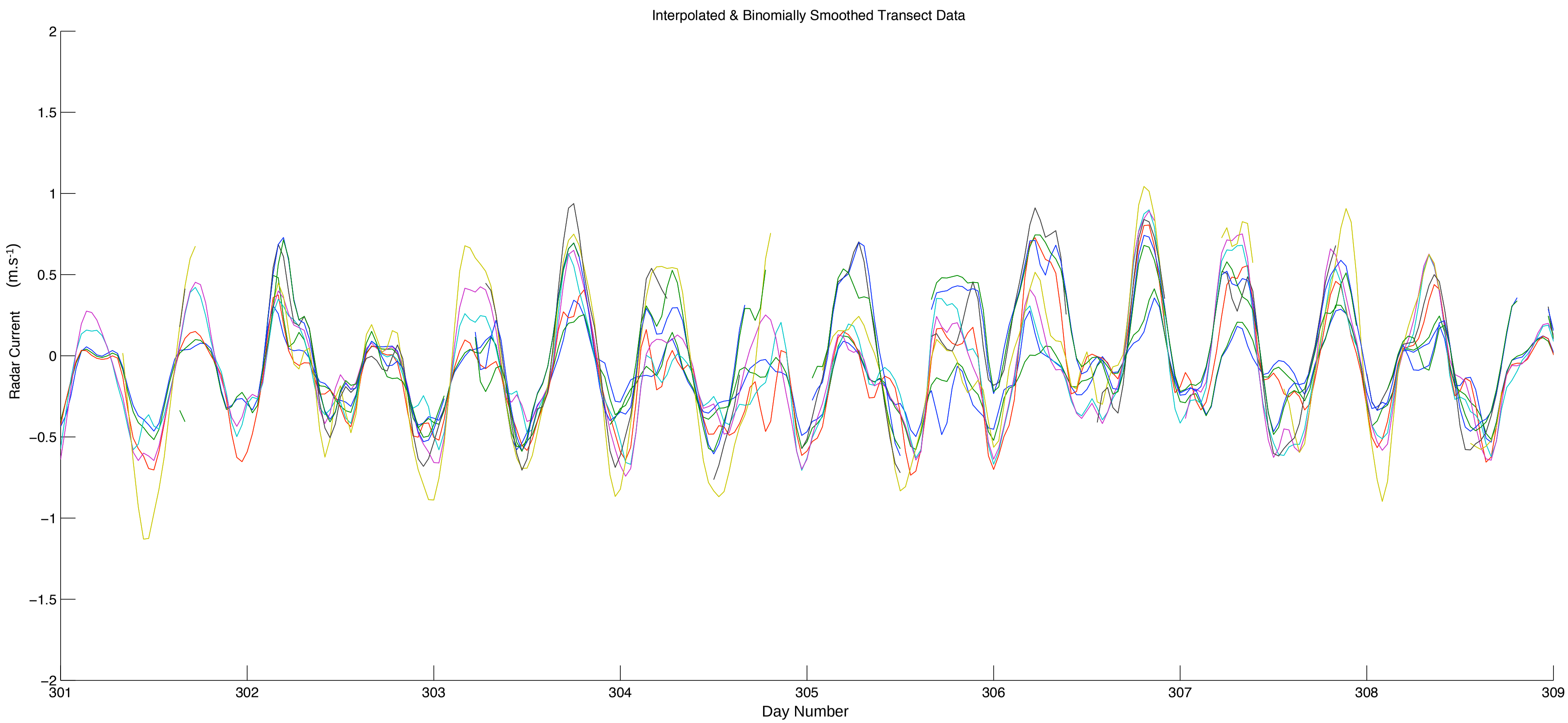

Figure 5.31 Surface Current Transect Time-series
(all points on transect)

There is still a significant level of noise in the transect current velocity signal (Figure 5.31), even after each point on the transect is interpolated and smoothed. This, together with the constant under-reporting of current speeds from the radar measurements led to the investigation of sources of noise in the radar signal. The next section describes some of these noise artefacts and a different approach to obtaining surface current measurements from the radar spectra.

5.6 Radar Analysis - Direction Finding with Phase Correlation Discrimination

Close inspection of the radar spectra reveals that spurious noise peaks appear randomly within the range spectra. At times these peaks appear outside of the area we would expect to see Bragg peaks, but at other times these peaks are in superposition with Bragg peaks. This noise can affect the derivation of current measurement from the spectra, so a method of characterising the noise was developed and used to improve the accuracy of current measurements.

The range spectrum from each of the antennae is used to calculate the sum of the power spectra for all the antennae. For the example given in Figure 5.32, we can identify two main energy areas, as highlighted. One is approximately between -2 to -1 Hz, the other around +3 Hz. Now, we would expect Bragg wave signals to be shifted by the underlying current velocity from their +/- 1.2587 Hz positions and so, could reasonably expect that the -2 to -1 Hz energy is the Bragg wave signal. The signal situated at 3 Hz is therefore considered to be noise. It does not represent Bragg energy and its origin may be due to outside interference or internal electrical noise within the radar system.

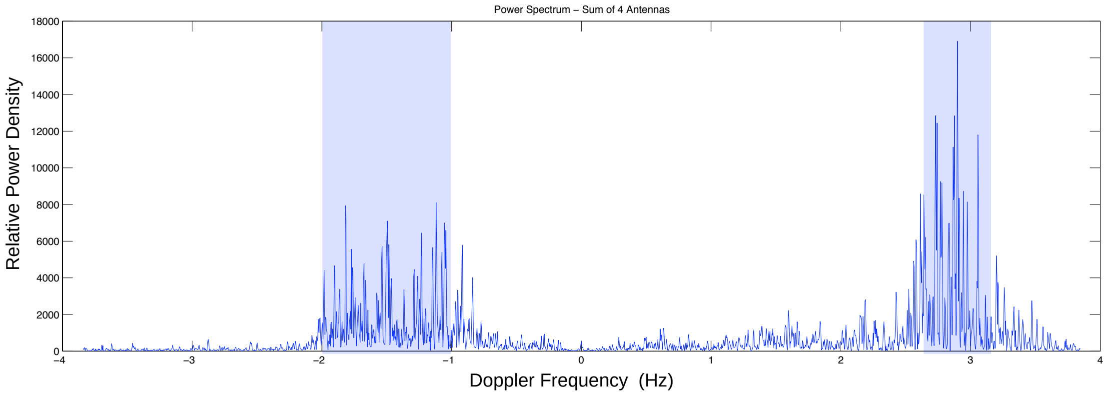

Figure 5.32 Power Spectrum, Sum of 4 Antennae - Day 274, 1925

Looking in more detail at the -2 to -1 Hz energy band, we compare the phase of each antenna's signal with another. First, the phase values for antenna #1 are plotted against the phase values for antenna #2 for each point on the spectrum in this frequency band, as shown in the first plot of Figure 5.33.

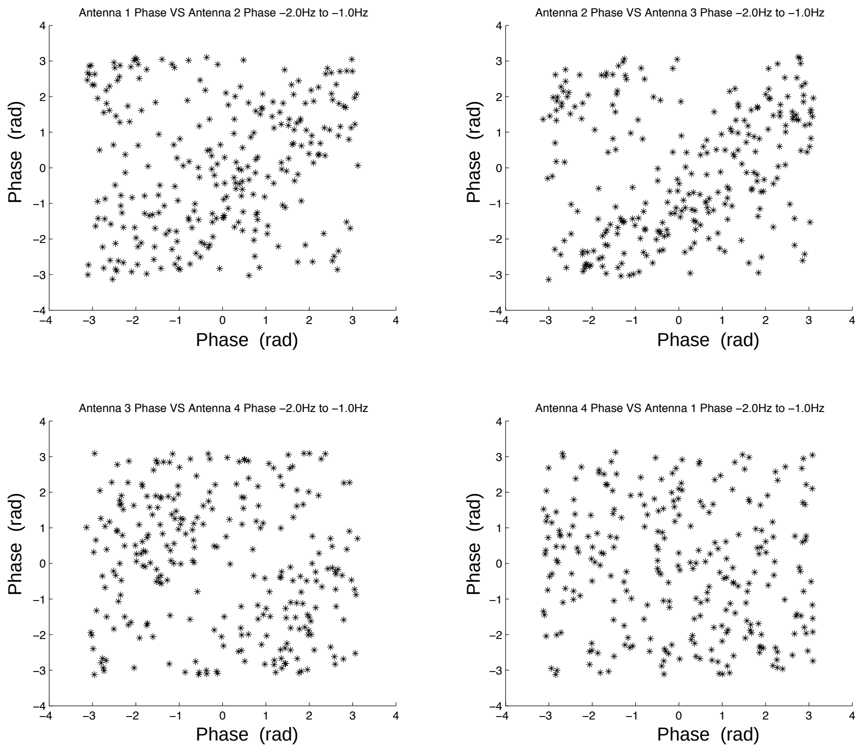

Figure 5.33 -2 to -1 Hz Region Phase Correlation

Similarly, the phase relationships between the other antennae are also plotted. The phase relationship plot for the 3Hz energy band is shown below in Figure 5.34.

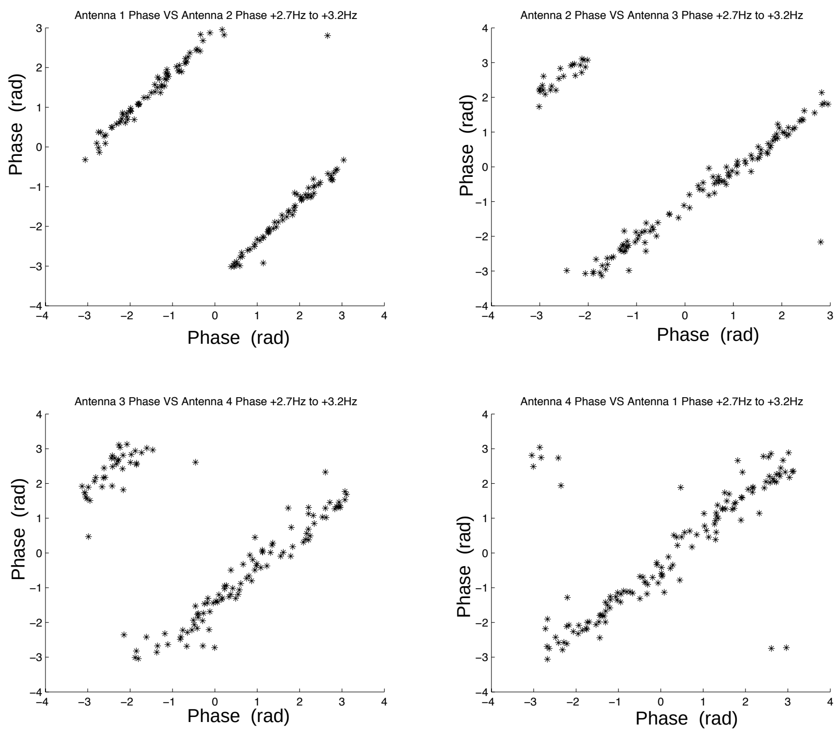

Figure 5.34 3Hz Region Phase Correlation

For the 3 Hz noise peak, the phase of the signals from each antenna is strongly, linearly correlated. This shows that the origin of these spurious signals is not from external interference, as if this were the case they would originate from a specific direction or directions. When direction finding techniques are used on these spurious signals, they appear to originate from either +/- 45 degrees to the azimuth of the antenna array regardless of the orientation, because the phases are always linearly correlated.

Since PMAP2DAT does not have the function to discern this phase correlation when selecting energy peaks, a separate analysis algorithm was written in MATLAB to produce radial current measurements from range spectra. The MATLAB algorithm uses the phase correlation property of peaks to discard peaks that are due to spurious internal noise. PMAP2DAT is still used to batch-process the range time-series into range spectrum .dat files.

5.6.1 MATLAB Direction Finding Algorithm

The first step undertaken by the MATLAB Direction Finding algorithm, “DFind” is to import a range spectrum file containing the range spectrum for each of the ranges to be analysed. As the radar isn’t satisfactorily obtaining signals from beyond 10 range cells, the DFind algorithm is limited to 10 range cells to increase the processing speed.

Processing is undertaken one range cell at a time. The example shown will use the complex spectra from the 5th range cell obtained by the Lido station. Initially, the power spectrum for each antenna is generated and summed together (Figure 5.35).

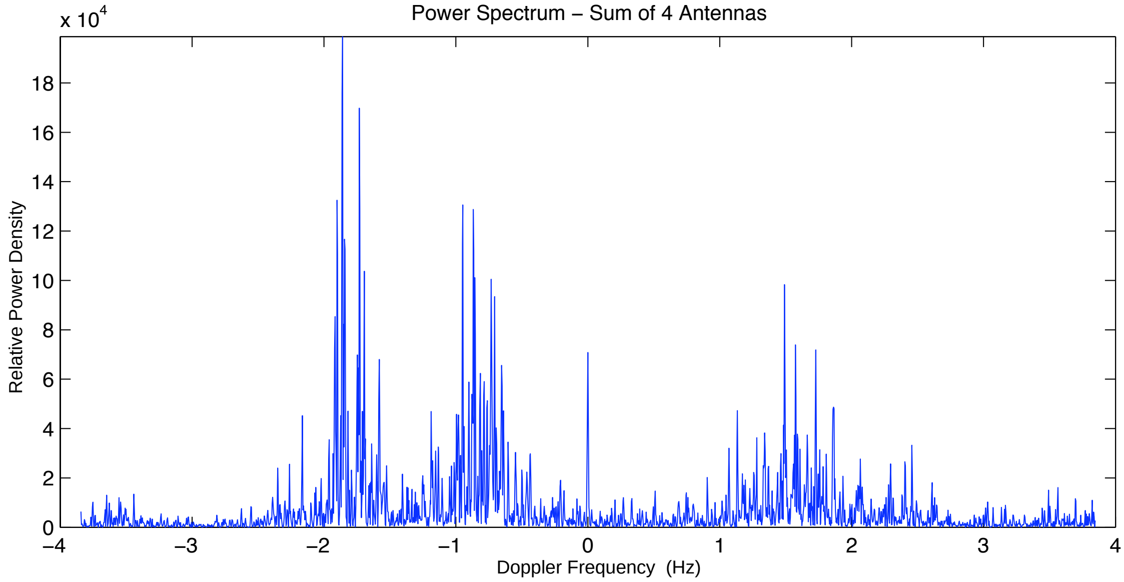

Figure 5.35 Power Spectrum (Day 291, 0445 Range 5) - Sum of 4 Antennas

The power spectrum sum for all antennae is then smoothed, and the largest peak on the negative half of the spectrum is identified. The width of the selected peak is determined by the points at which the signal falls 6 dB below the main peak.

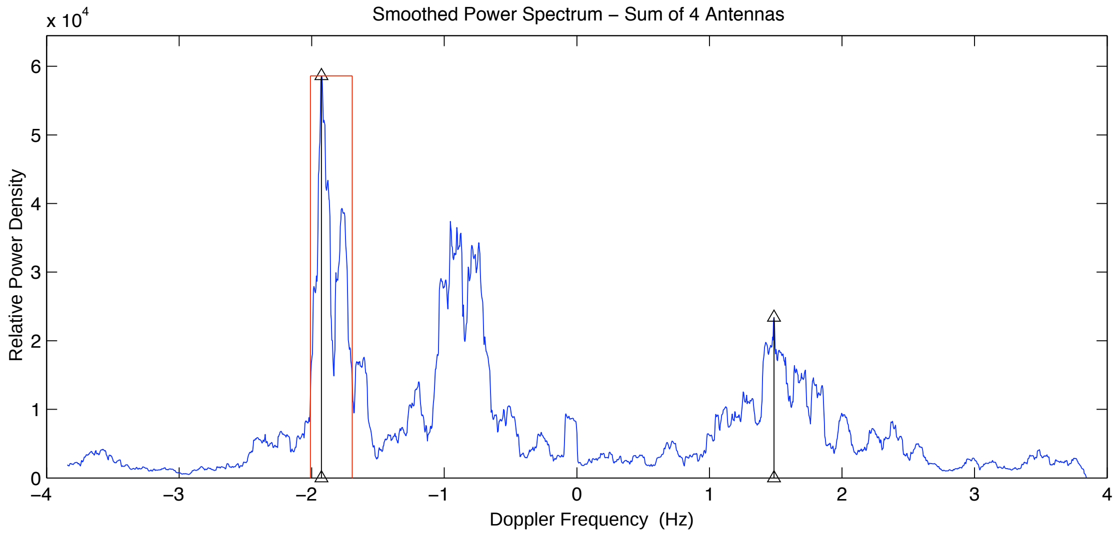

Figure 5.36 Smoothed Power Spectrum (Range 5) - Selection of Positive Peak

The selected peak is then compared with the noise level of the spectrum to determine if it satisfies a minimum signal-to-noise criterion. The Rayleigh noise figure for the spectrum is determined using a method developed by Heron and Heron (2001). Using this method, the summed power spectrum is rank ordered as per the first plot shown in Figure 5.37.

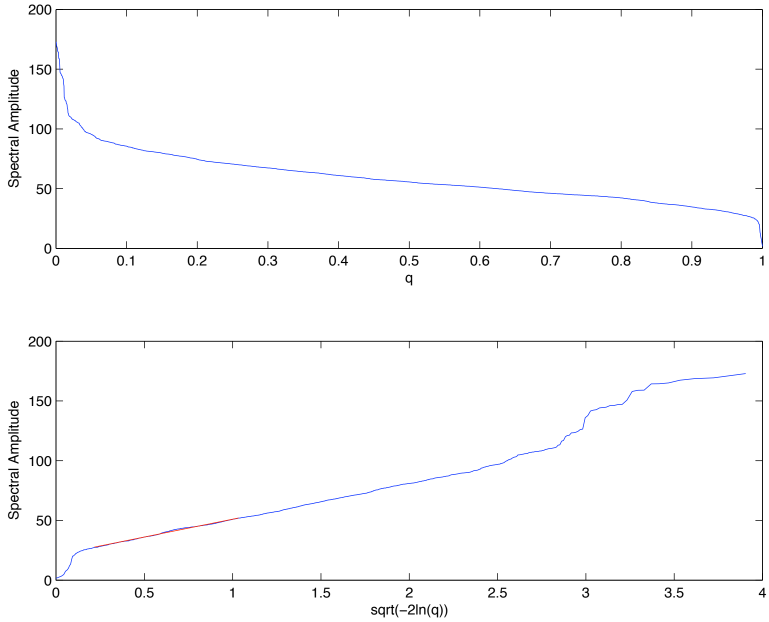

Figure 5.37 Rank Ordered Spectrum, and $[p, \sqrt{-2\ln(q)}]$

Using the relation for Rayleigh distributed random noise,

$$\sigma^2 = \frac{p^2}{-2\ \ln(q)} \tag{5.23}$$

we may use the relationship between *p* and *q* to determine the Rayleigh noise figure as a least-squares fit through data points $[p, \sqrt{-2\ln(q)}]$. As such, the second plot in Figure 5.37 shows a least-squares fit to determine the slope, σ of the linear portion. For a chosen spectral peak to be considered having sufficient signal level, it must be six times the slope value of σ.

Once the peak is selected and satisfies the signal-to-noise criterion, it is checked for the phase correlation effect shown above. The phase of the complex spectrum for antennas 1 and 2 is sorted and plotted in ascending order. A least-squares fit is plotted for this comparison and if the standard deviation of the residuals is greater than 1 the peak is rejected. This is the case for the data shown in Figure 5.38 so the initially selected peak is rejected.

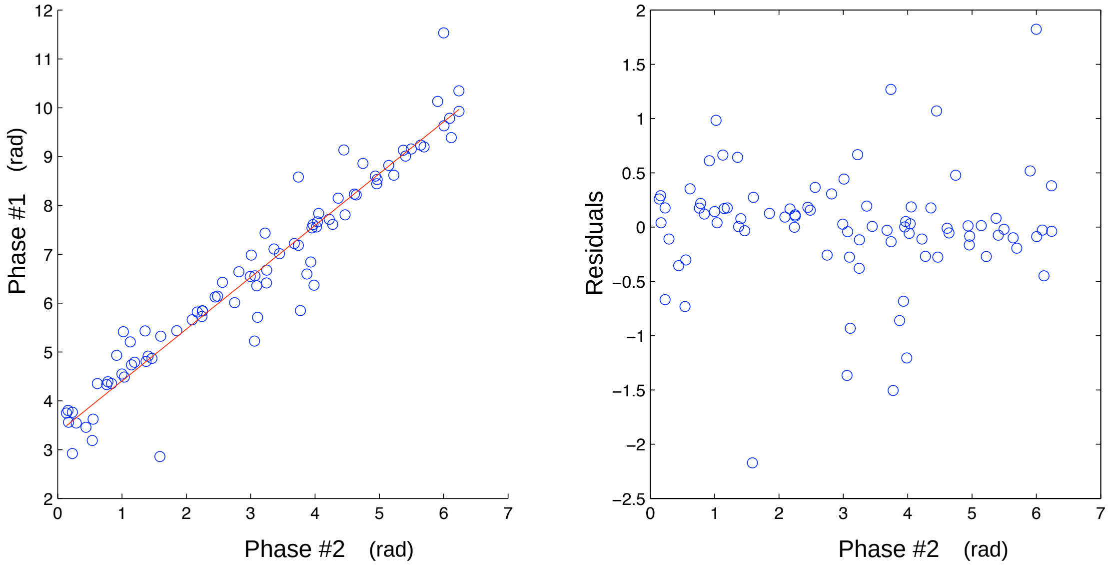

Figure 5.38 Phase Comparison Least-Squares Fit (Std. Deviation of Residuals > 1)

Once a peak is rejected, the next most significant peak on that half of the spectrum is selected, as shown in the case of Figure 5.39.

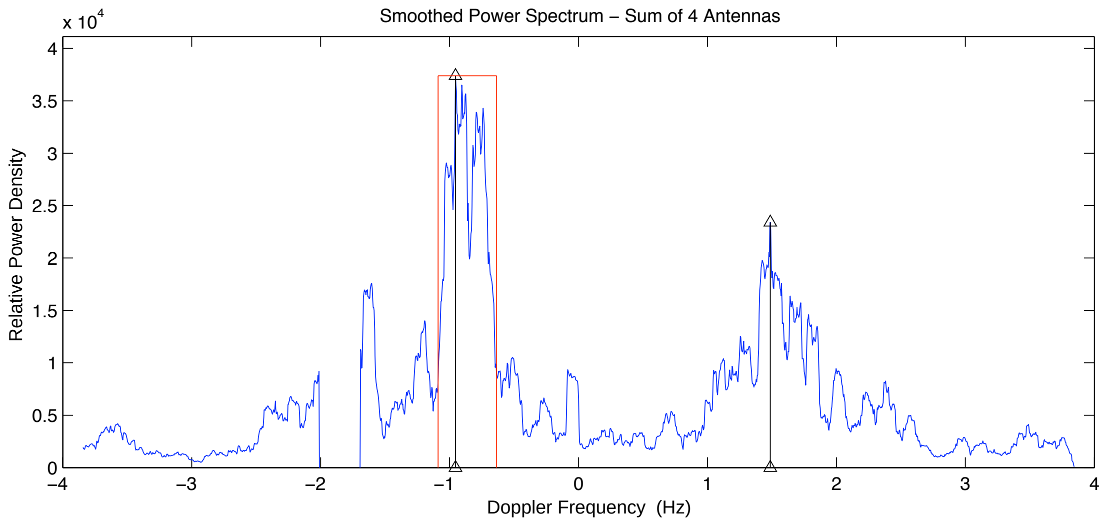

Figure 5.39 Smoothed Power Spectrum (Range 5) - Selection of Next Peak

This next peak is again compared with the noise figure, and examined for phase correlation. As shown in Figure 5.40, the phases are not well correlated between antennas 1 and 2 for this second selected peak, so it is accepted as being a valid peak for the negative half of the spectrum.

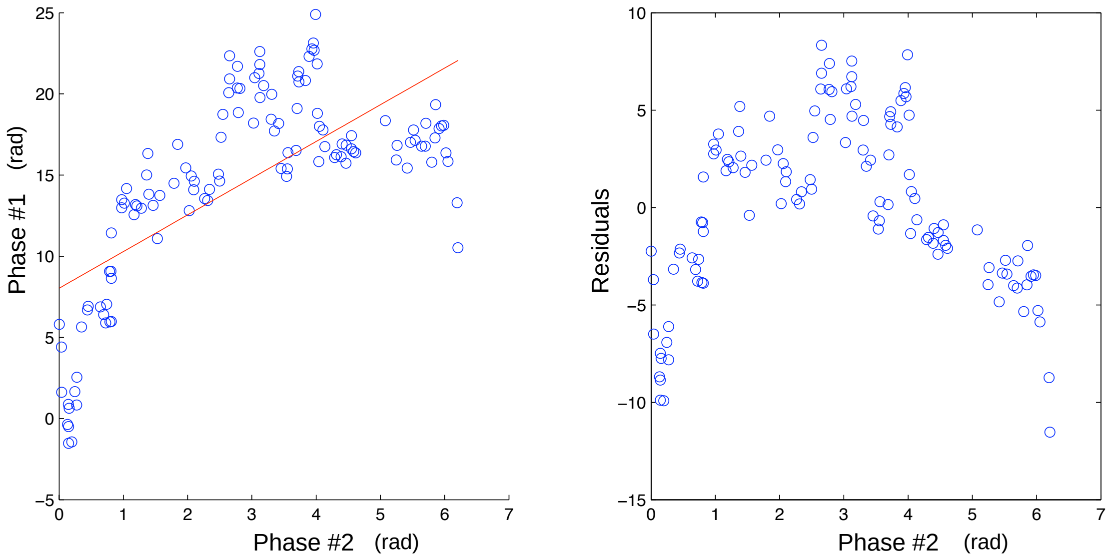

Figure 5.40 Phase Comparison Least-Squares Fit - Peak B
(Standard Deviation of Residuals < 1)

This process is repeated for the positive half of the spectrum. If valid peaks exist in both halves of the spectrum, the strongest peak is selected to be used in the direction finding process to determine radial current velocities. If there are no valid peaks in either half of the spectrum, no current measurements are obtained for that range spectrum.

The peak that is selected for direction finding is defined by a start and stop frequency point. The complex I and Q values corresponding to each frequency point of the antenna spectrum are used to determine the azimuth of signal origin for each frequency point. Using antenna array pattern multiplication, the values for I and Q can be used to plot the magnitude of the signal for various steering angles, thus determining the direction at which this is a maximum.

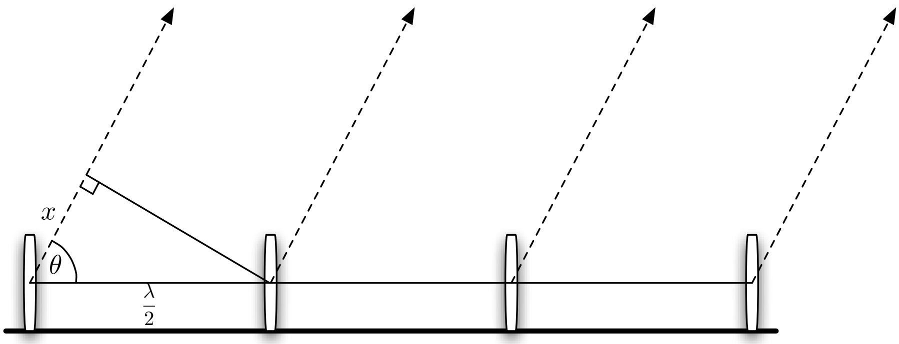

Figure 5.41 Antenna Array Steering Geometry

For the linear antenna array shown in Figure 5.41 with half-wavelength spacing of the elements, the magnitude for phase angle ψ can be calculated as follows :-

$$g = |a_1 \ e^{j\phi_1} + a_2 \ e^{j\phi_2 + \psi} + a_3 \ e^{j\phi_3 + 2\psi} + a_4 \ e^{j\phi_4 + 3\psi}| \quad (5.24)$$

where a_1, a_2, a_3, a_4 and $\phi_1, \phi_2, \phi_3, \phi_4$ are the magnitudes and phases computed from the I and Q values for each receiver at a particular spectrum frequency point. As the phase angle, ψ is varied from -90° to +90°, this corresponds to a physical steering angle of

$$\cos\theta = \frac{x}{\frac{\lambda}{2}} = \frac{\psi}{2\pi}\lambda * \frac{2}{\lambda} = \frac{\psi}{\pi} \quad (5.25)$$

where the physical steering angle, θ is calculated as

$$\theta = \cos^{-1}\frac{\psi}{\pi} \quad (5.26)$$

As the phase angle, ψ, is varied to 'steer' the antenna through all forward angles of azimuth, the magnitude, *g* can be plotted against steering angle, θ as shown in Figure 5.42.

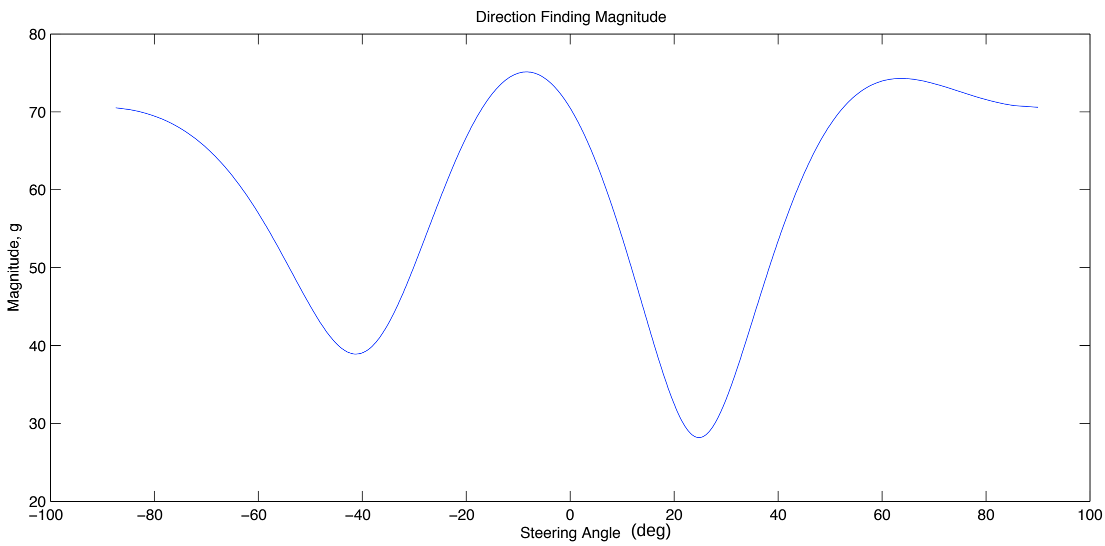

Figure 5.42 Direction Finding Magnitude vs Steering Angle

In figure 5.42, the peak magnitude is determined. If this peak doesn't fall within +/- 30° of the boresight direction, it is discarded. If the peak falls within +/- 30°

of the boresight as shown above, it must then satisfy a further hysteresis criterion in order to be accepted. The minima either side of the peak must fall to below half the value of the peak. In the case of Figure 5.42, the left-hand minimum does not satisfy this, so this frequency point would be discarded and not used to derive a radial measurement. If a frequency point within the peak on the spectrum satisfies all direction finding criteria, the Doppler shift radial current measurement is obtained for that frequency point and stored as a radial measurement.

Once radial current measurements are obtained for every frequency point of a valid peak in the range spectrum, these radial measurements are stored for later re-gridding. An example of the radial current measurements obtained for the spectrum shown above for the 5th range on Day 291 at 0445 h is presented below in Figure 5.43.

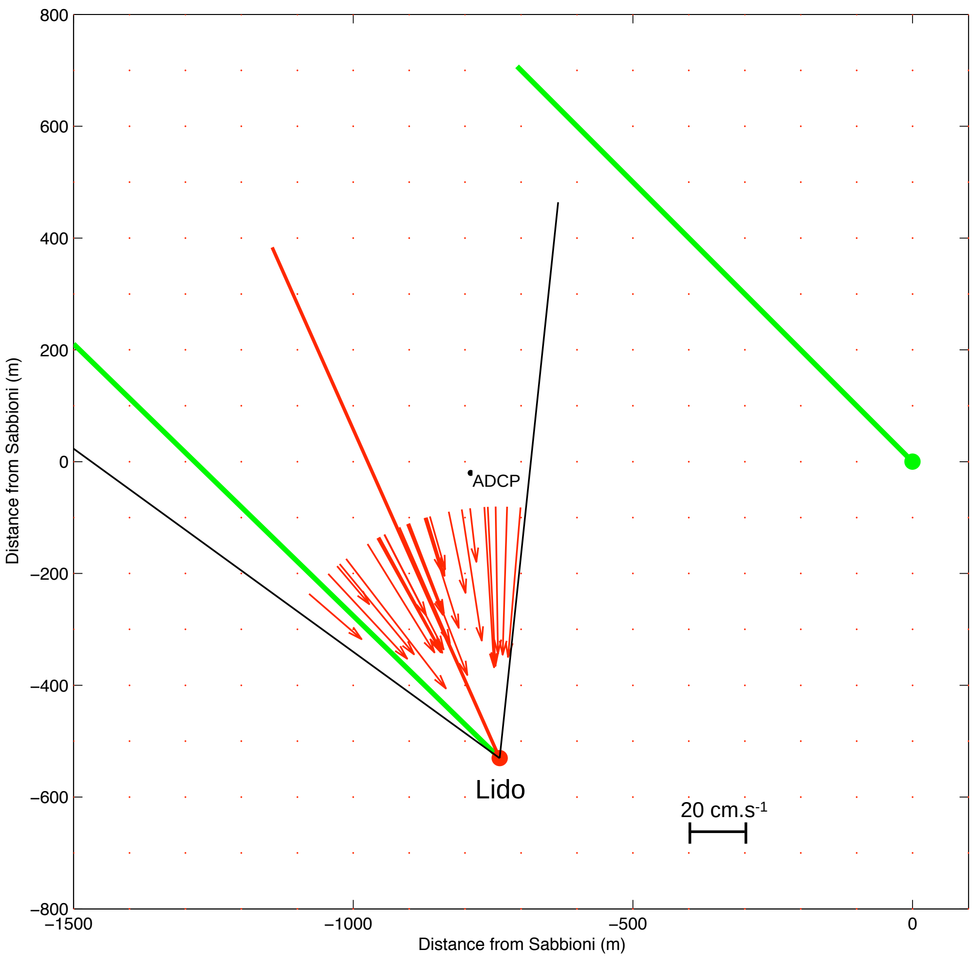

Figure 5.43 Lido, Day 291 at 0445 h - Range 5 Radial Measurements

Once every range spectrum has been processed to obtain radial current measurements, these data are used to produce radial velocity measurements for gridpoints using inverse distance weighting techniques such as those shown in Sections 5.4 and 5.5. Radial measurements lying within 70 m of each gridpoint are used to create an inverse distance weighted average radial current velocity for that gridpoint. Any velocity measurement that differs by more than twice the standard deviation from the mean is also discarded prior to a final mean being calculated for a gridpoint. The re-gridded radials obtained for the Lido acquisition on Day 291, 0445 h are shown below in Figure 5.44.

Once the radial measurements are obtained for the pre-determined gridpoints, these data are output in the same file format as that produced by the PMAP2DAT analysis software. This allows all the existing secondary analysis software developed in MATLAB to be able to process the current data obtained using MATLAB DFind.

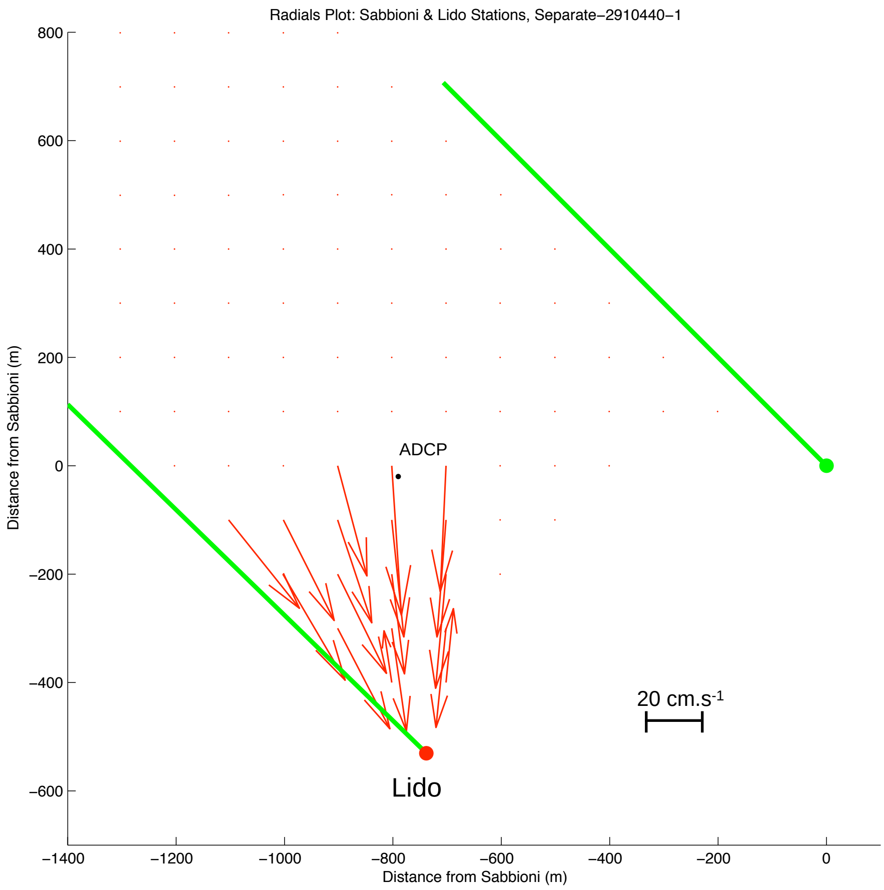

Figure 5.44 Lido, Day 291 at 0445 h - Radial Measurements

‘CurrentsGUI’ was used to process the radial current measurements obtained using the DFind algorithm for the entire deployment period. The time-series for the ADCP Region average current obtained is shown below in Figure 5.45. Compared with the time-series obtained using the PMAP2DAT algorithm (Figure 5.19), the DFind algorithm has resulted in higher peak current readings. The structure of the time-series for the Lido station is more representative of the tidal flow with spring and neap tides clearly present. The average current signal obtained for the ADCP region using the Sabbioni data has more noise though.

Similarly, the comparison between 2-pass interpolated and smoothed ADCP region average with the ADCP current measurements (Bin 9) shows that the use of the MATLAB DFind algorithm has improved the correlation between the two instruments, though not substantially (Figure 5.46).

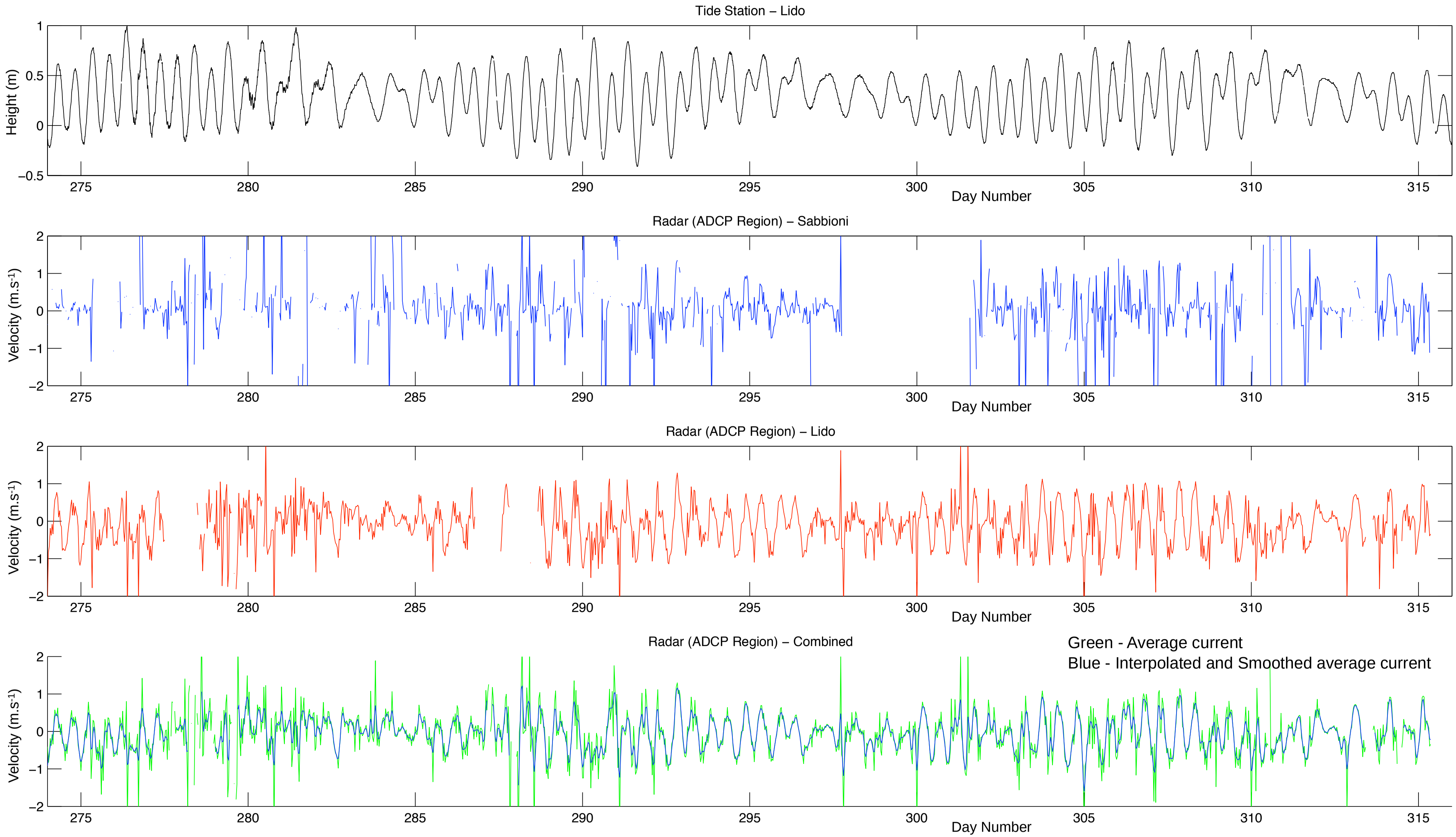

Figure 5.45 MATLAB DFind, ADCP Zone Average Current Time-Series

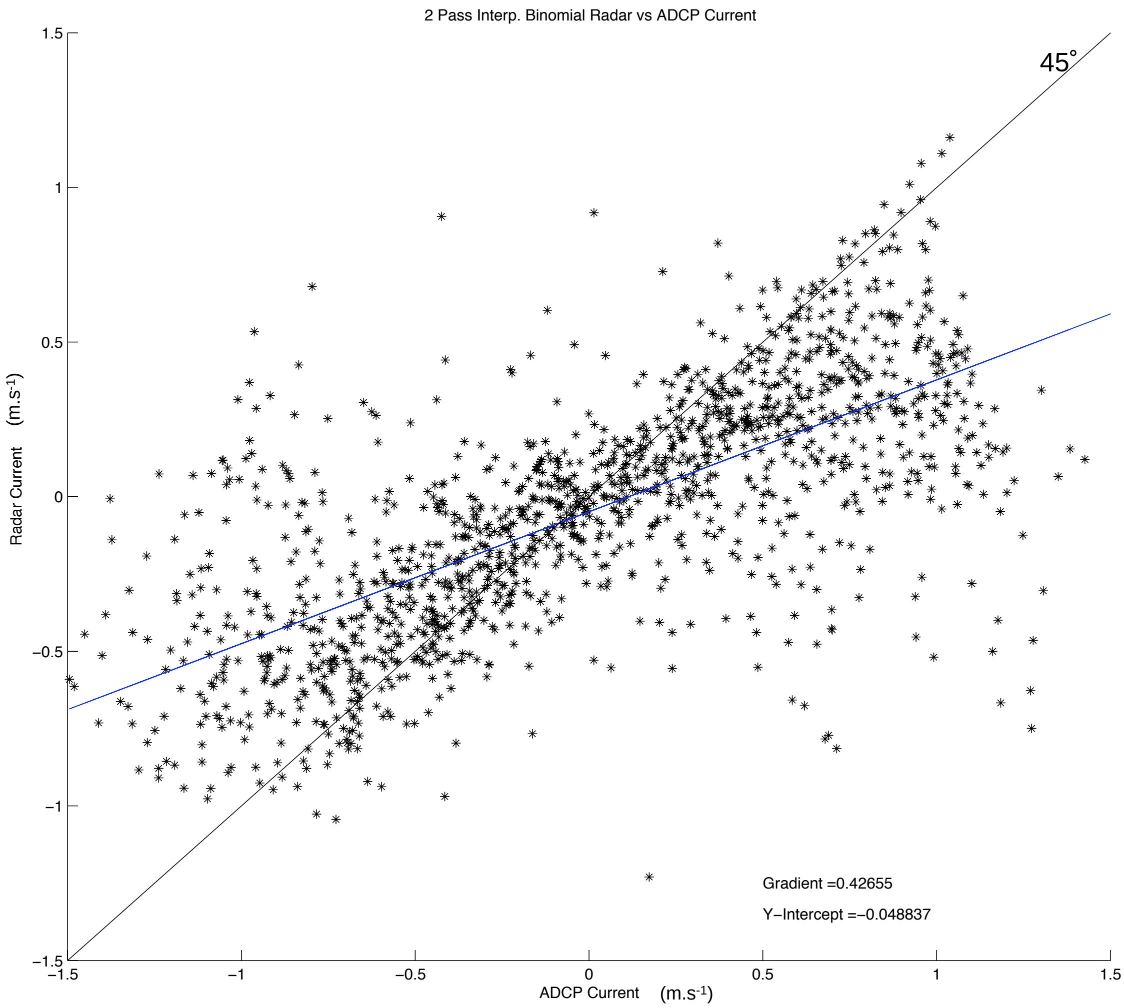

Figure 5.46 MATLAB DFind Interpolated/Smoothed Radar Current (ADCP Zone) vs ADCP Current (Bin 9)

The MATLAB DFind algorithm was developed to improve the accuracy of the radar measurements by characterising noisy peaks in the spectra and discarding these where necessary. The DFind algorithm has produced an improved time-series record and greater correlation with the ADCP measurements. The surface current velocity time-series for individual transect points is too noisy to be used for a definitive mass transport calculation.

5.7 FFT Analysis and Accumulated Transect Profiles

Although the radar surface current measurements obtained using MATLAB DFind are still too noisy to be used for calculating mass transport, alternative methods of analysing the ADCP region and transect surface currents were investigated.

5.7.1 FFT Analysis

This method analyses the transect time-series data in the frequency domain to differentiate between low-frequency tidal driven current signals and noise. For each day of the deployment period, a Fast Fourier Transform is created for both the ADCP signal and the ADCP region radar signal. An example of this for day 274 is shown below in Figure 5.47.

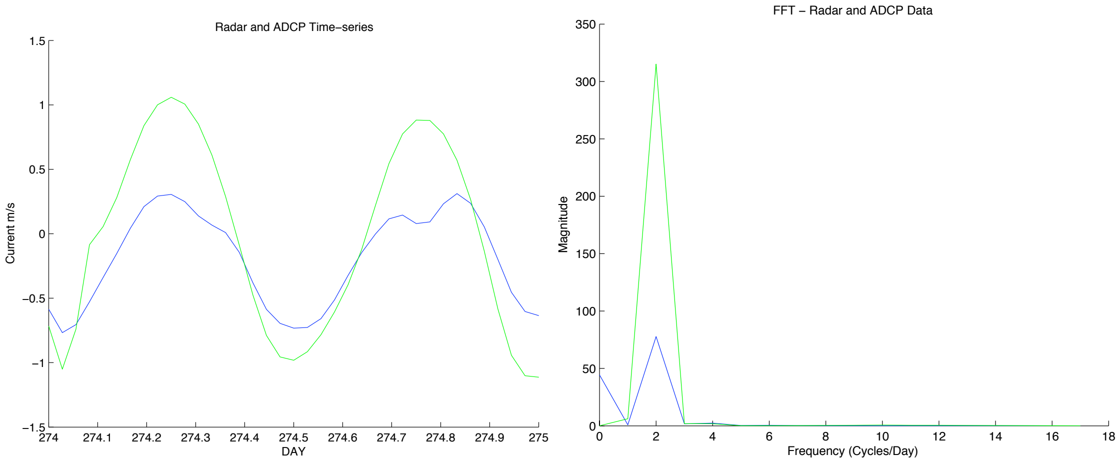

Figure 5.47 FFT Analysis - Acceptable Radar Signal
(Blue - Radar, Green - ADCP)

Good quality current signals from either radar or ADCP are seen visually as smooth low-frequency sinusoidal curves, such as that shown in the first plot of Figure 5.47. These good quality current measurement signals are characterised as having strong spectral peaks at 2 cycles/day, representing the semi-diurnal tidal signal. In this analysis, good signals were identified as having greater than 35% of the area under the spectral curve within the region between 1 and 3 cycles/day. An example of a poor radar signal compared with the ADCP signal is shown below for Day 279 in Figure 5.48.

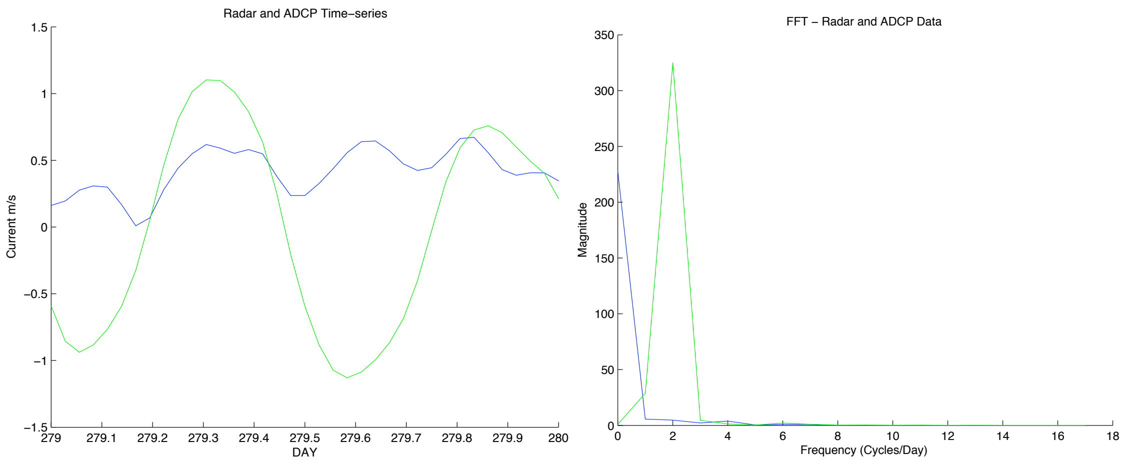

Figure 5.48 FFT Analysis - Poor Radar Signal
(Blue - Radar, Green - ADCP)

In this case, the ADCP region radar signal is significantly different from the ADCP signal. The spectral analysis shows that much of the energy is centred around 0 cycles/day. Data obtained on days such as this are discarded, as the spectral signal does not lie between 1 and 3 cycles/day. The remaining good quality data are used to produce a comparison of the ADCP and the ADCP region radar data, as shown in Figure 5.49 below.

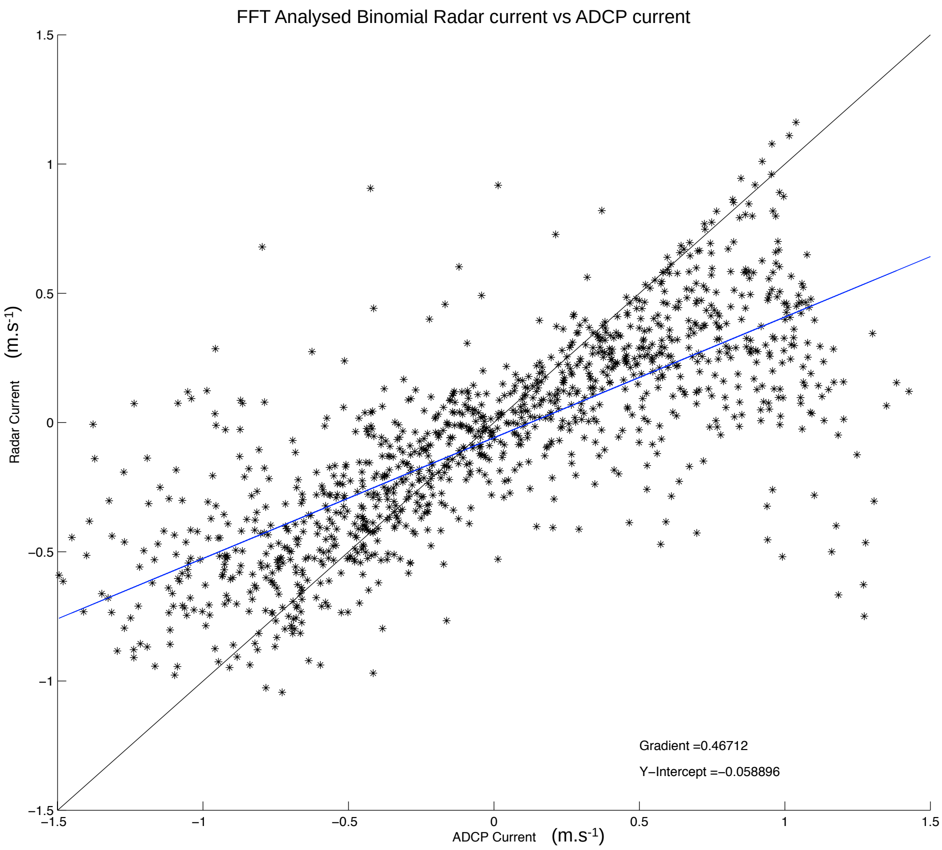

Figure 5.49 FFT Analysed Data vs ADCP Current

Compared with Figure 5.46, this plot shows a reduced number of outliers. There is still a significant disagreement between the readings obtained from each instrument though. Even when only using good quality radar data, the radar is still reporting lower current measurements than the fixed ADCP in the channel.

5.7.2 Accumulated Transect Profiles

Profiles of the surface current along the channel transect were created for various bins of flood and ebb current velocity, and the state of tide. The interpolated and smoothed transect profile measurements obtained in Section 5.6 were sorted into bins using the fixed ADCP velocity measurements and tide gauge data as references. The ADCP velocity ranges used for the sorting bins are listed in Table 5.1.

Ebb Tide	Flood Tide
Currents -0.1 to +0.1 m/s	Currents -0.1 to +0.1 m/s
Currents -0.1 to -0.25 m/s	Currents +0.1 to +0.25 m/s
Currents -0.25 to -0.50 m/s	Currents +0.25 to +0.50 m/s
Currents -0.50 to -0.75 m/s	Currents +0.50 to +0.75 m/s
Currents -0.75 to -1.00 m/s	Currents +0.75 to +1.00 m/s
Currents -1.00 to -1.25 m/s	Currents +1.00 to +1.25 m/s

Table 5.1 Transect Profile Sorting Bins

A two pass iteration process was used to remove outliers beyond twice the standard deviation from the mean. The remaining transect point measurements within each bin were plotted, together with the mean surface current for each point across the transect, as shown in Figure 5.50.

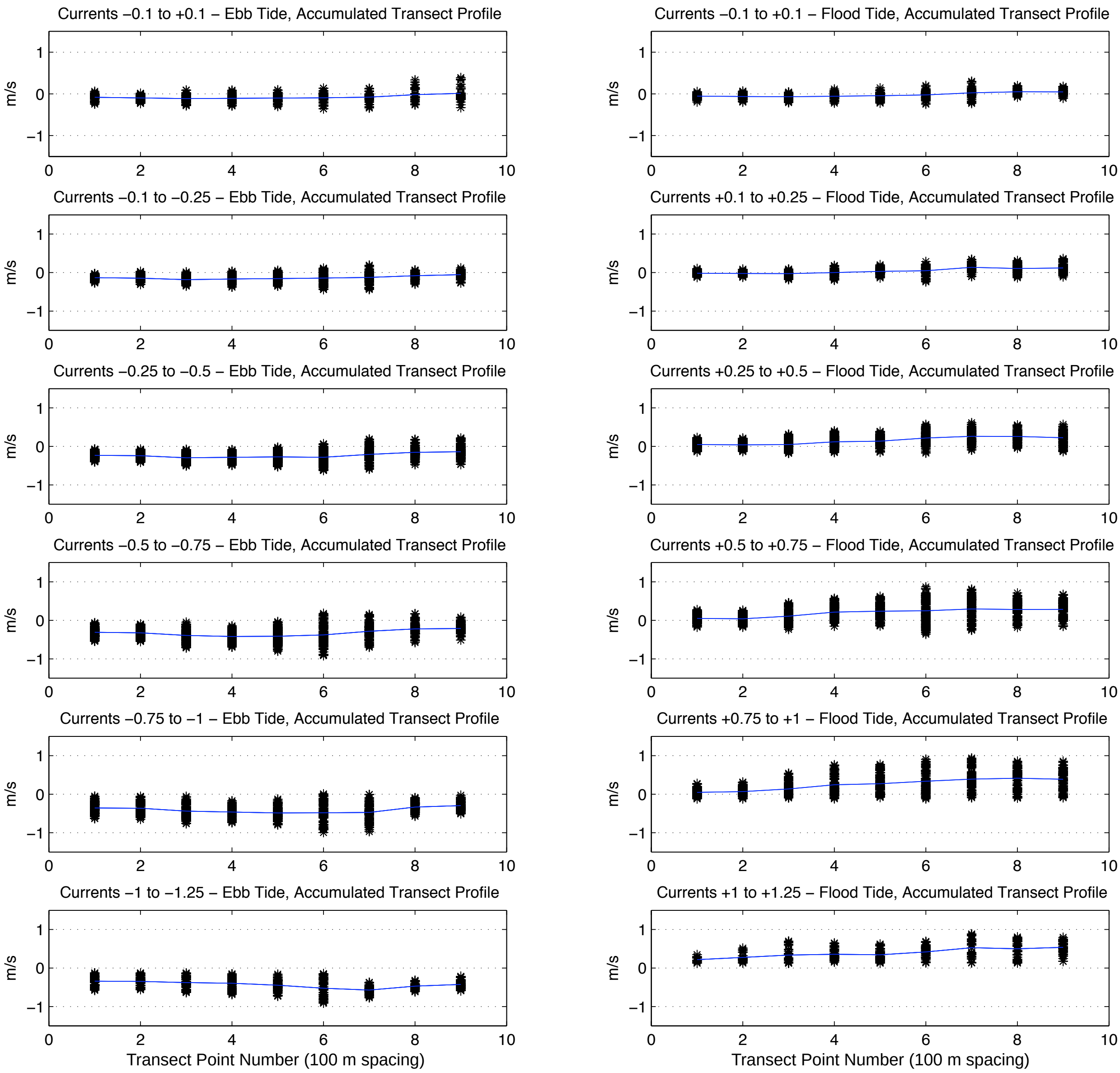

Figure 5.50 Accumulated Transect Profiles

The plotted results are consistent with all the previous comparisons that have been made between the radar and the ADCP results, with the radar consistently measuring lower current velocities. As the ADCP measured velocity increases, the variability of the radar measurements also increases.

In the next section, we discover why there are discrepancies between the radar current velocities and those obtained by the ADCP.

5.8 Modified Range Resolution, Manual Direction Finding Analysis

After all the previous analyses had been undertaken with the understanding that the PortMap radar had a range resolution of 100 m, the PortMap manufacturer, Helzel Messtechnik reported a fault with the programming of the real-time computers within PortMap.

The programming fault was in one of the range-resolving Fast Fourier Transform operations performed by the CL7, whereby the incorrect half of the spectrum was being used. Therefore, the desired spectrum signal produced by the 152.2 MHz signal is discarded. By chance, the signals and range resolved data actually being used were in fact produced by a 5th harmonic (145.42 MHz) of the primary oscillator frequency (29.084 MHz). This resulted in a change of bandwidth by a factor of 5, which in turn caused the range resolution to be 20 m instead of 100 m. The power level of the 5th harmonic signal was also significantly less than the 152.2 MHz signal resulting in a lower signal-to-noise ratio and further contributing to a reduction in the range of the system. One contributing factor to the low transmit power was that the 145.42 MHz frequency was well out in the edge of the transmitter and antenna filters. One interesting consequence of this was that the bandwidth occupied by this very low signal was very wide, making the 20 m resolution the true spatial resolution of the system.

To compensate for the fault present in the PortMap system, the MATLAB DFind algorithm was modified to use a range resolution of 20 m and a radar frequency of 145.42 MHz. Using the expected maximum range cell number from Section 5.1 with this new range resolution of 20 m, we can see in Figure 5.51 the effect that this has on the achieved coverage of the channel by the radar system.

With the change in range resolution, a new high-resolution measurement grid is required for re-gridding the radial measurements. A grid with 20 m spacing in both the x and y directions was created with the Sabbioni station again used as the origin.

Figure 5.51 Modified Range Resolution (20 m) Estimated Maximum Radar Range (Image Map Courtesy of Cnes/Spot, DigitalGlobe, TerraMetrics and GoogleEarth)

Using a new radar frequency of 145.42 MHz, Bragg wave spectral peaks for zero surface current will now be centred at +/- 1.2303 Hz in the radar spectra.

Although highly time-consuming, the direction finding algorithm was modified to require manual intervention to confirm each Bragg peak selected for obtaining current measurements. This was done to attain the best possible current measurement results from a select number of days within the six week deployment. Any peaks that visually appear too noisy were discarded by operator intervention. Data acquired by both the Sabbioni and Lido stations were analysed for a single direction looking up the channel for Days 291, 292, 293, 294 and Days 302, 303, 304, 305, 306. These days were selected because they were during spring tides and were identified as having better signal-to-noise ratio for the signals acquired. An example short-range radial current map from data acquired on DAY 291 at 2320 h is shown in Figure 5.52. Note the individual current maps for each station, as a result of higher resolution and shorter range.

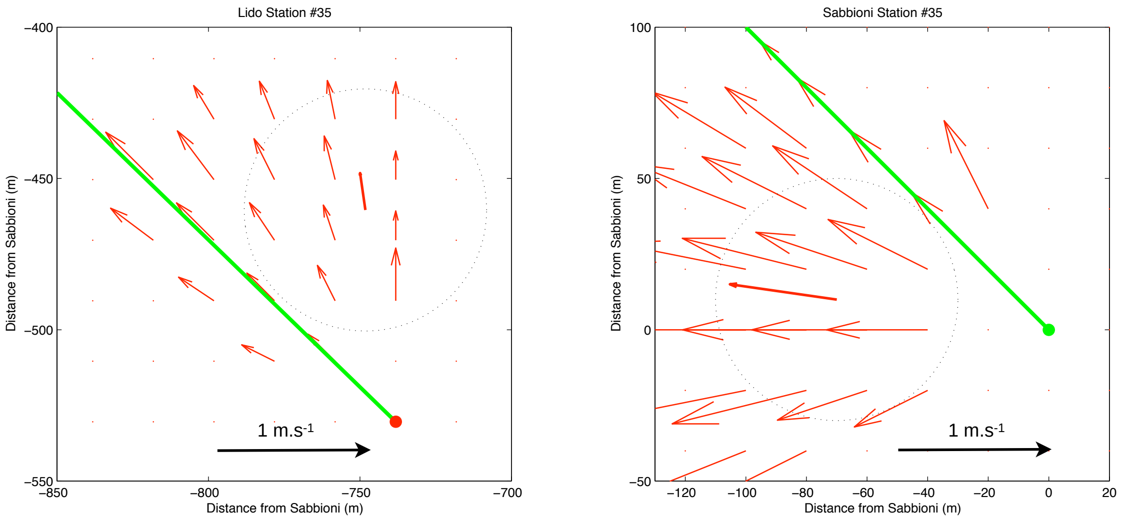

Figure 5.52 Current Vector Map, DAY 291 at 2320 h (20 m Range Resolution)

In this example during a flood tide, a much stronger current velocity is seen from the water entering the channel around the Sabbioni station than near the Lido station.

Of particular note in Figure 5.52 are the regions indicated by the dotted line circle near the Sabbioni and Lido stations. In a way similar to the ADCP zone average produced in Section 5.4, an average radial current is calculated within these circles using inverse-distance-weighting averaging of the surrounding radial measurements. This average measurement is shown on the plot as a thick vector arrow at the centre of each circle near the Sabbioni and Lido stations. These are used to create a time-series of average current measurements in the vicinity of the Sabbioni and Lido breakwaters. For example, the time-series for average surface currents within these zones for Day 291 is shown below in Figure 5.53. Positive current flow indicates a flood tidal stream. This time-series has also been binomially smoothed using a three point binomial series (1 2 1).

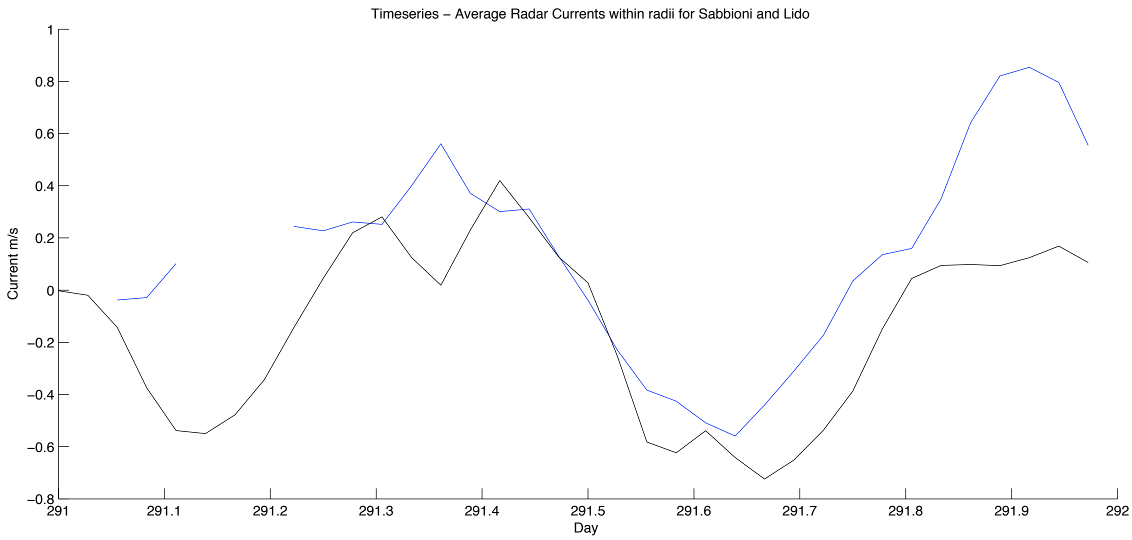

Figure 5.53 Sabbioni and Lido Breakwater Zone Current Averages
(Blue - Sabbioni, Black - Lido)

As per the current vector map above, we see that toward the end of Day 291, the incoming tidal stream at Sabbioni exceeds that for the Lido side of the channel. This time-series representation for average current at either side of the channel proves a useful tool for identifying variation across the channel. This is shown in more detail in Section 6.1 below where a phase difference between the Sabbioni and Lido station tidal streams is discussed.

6 Discussion of Oceanographic Outcomes

6.1 Tidal Stream Phase Difference between Sabbioni and Lido

Visual observations of the current flow within the Lido channel were recorded throughout the duration of the deployment period to be compared with recorded data. It was observed that during an ebb tide, current velocities on the deeper, Lido side of the channel were typically greater than those for the Sabbioni side. During a flood tide, the current entering around the Sabbioni breakwater was stronger than that observed on the Lido side. This horizontal gradient of current velocities across the channel was a consistently observed feature of the channel dynamics.

During periods of spring tides, the gradient of current velocities across the channel was at times seen to extend to current flow in opposing directions. During one of these events, while the tide was still ebbing on the Lido side of the channel, a turbid water plume was seen to flow into the channel on the Sabbioni side. A photo taken during one of these events on the 17th October, 2005 (Figure 6.1) clearly shows the turbid plume entering the channel on the Sabbioni side.

Figure 6.1 Turbid plume observed entering on the Sabbioni side of the channel

This observed current dynamic has an important influence on the transport of sediment into the Lido Inlet and the Venice Lagoon. It was observed that when the wind speed exceeds 5 $m.s^{-1}$, the wave re-suspension zone along the Adriatic Coast and Cavallino beach extends beyond the end of the Sabbioni training wall. When this occurs, the ingress of turbid water into the channel occurs, as depicted in the above photo.

The surface current measurements and corresponding average time-series for the Sabbioni and Lido breakwater zones produced as per Section 5.8 were examined for evidence of this cross-channel difference in current direction. The first short-range time-series generated for days 291 - 294 is shown in Figure 6.2 on the following page. The first feature of note is that during an ebb tide in the latter half of Day 291 the average current on the Sabbioni side of the channel is seen to reduce in strength and then change direction while an outgoing flow still exists on the Lido side of the channel. This feature can be examined more clearly by examining the short-range vector current maps.

In the sequence of vector current maps presented in Figures 6.3, 6.4, 6.5 and 6.6, each sequence is a 40 minute observation period. At the start of this sequence (plots 291.6388 and 291.6666), the current is observed to strongly ebb at both sides of the channel. The ADCP also records a strong ebb current at the centre of the channel. Over the next 80 minutes (plots 291.6944 and 291.7222) the current velocity decreases. This decrease is more noticeable at the Sabbioni side of the channel than the Lido side. In plot 291.7500, the current direction reverses at the Sabbioni side of the channel with a front seen to form between the opposing current regimes. Plot 291.7777 shows this flood current increasing at the Sabbioni side with the front progressing further up the channel. Note that in plots 291.7500 and 291.7777 the ADCP still records an outgoing tidal flow. Finally, in plot 291.8055 the tidal stream changes direction at both the Lido side of the channel and at the ADCP location. This occurs 80 minutes after the tide has changed direction at the Sabbioni side of the channel.

Another feature to note in the average current time-series (Days 291 - 294) is that on three occasions during days 292 and 293 the current starts to ebb on the Sabbioni side though it reduces in velocity as the Lido flow becomes stronger.

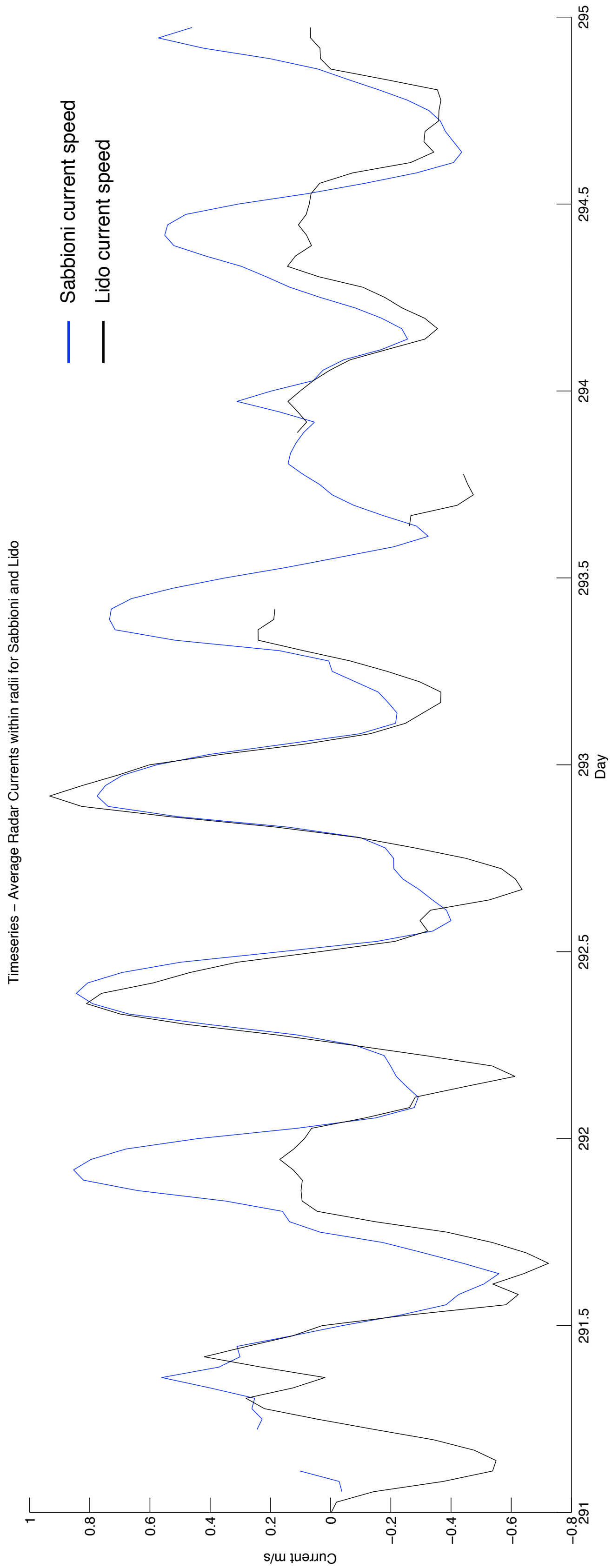

Figure 6.2 Breakwater Zone Time-series : Day 291 - 294

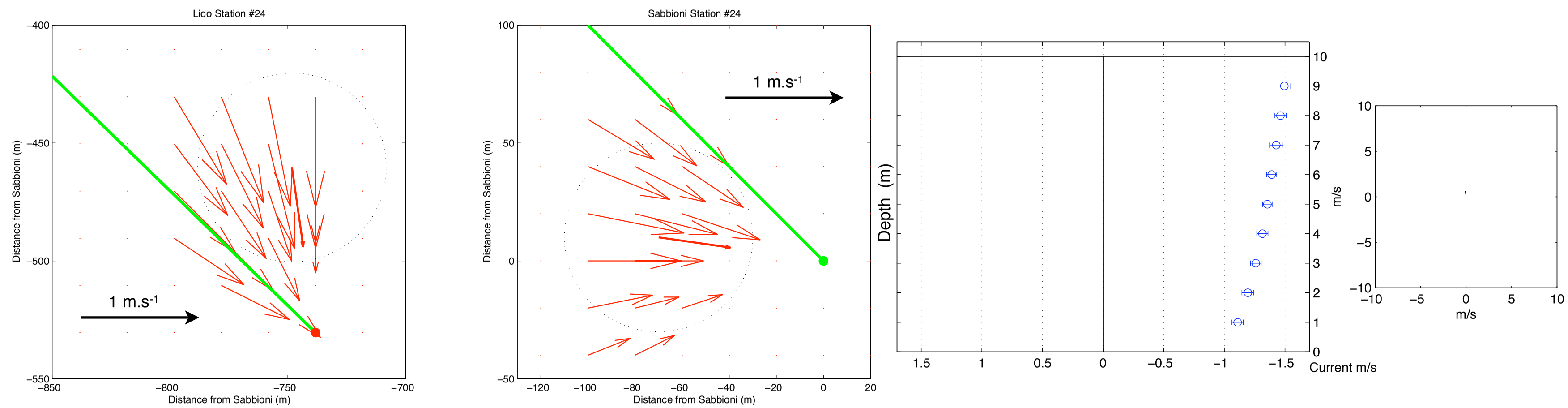

UTC 291.6388

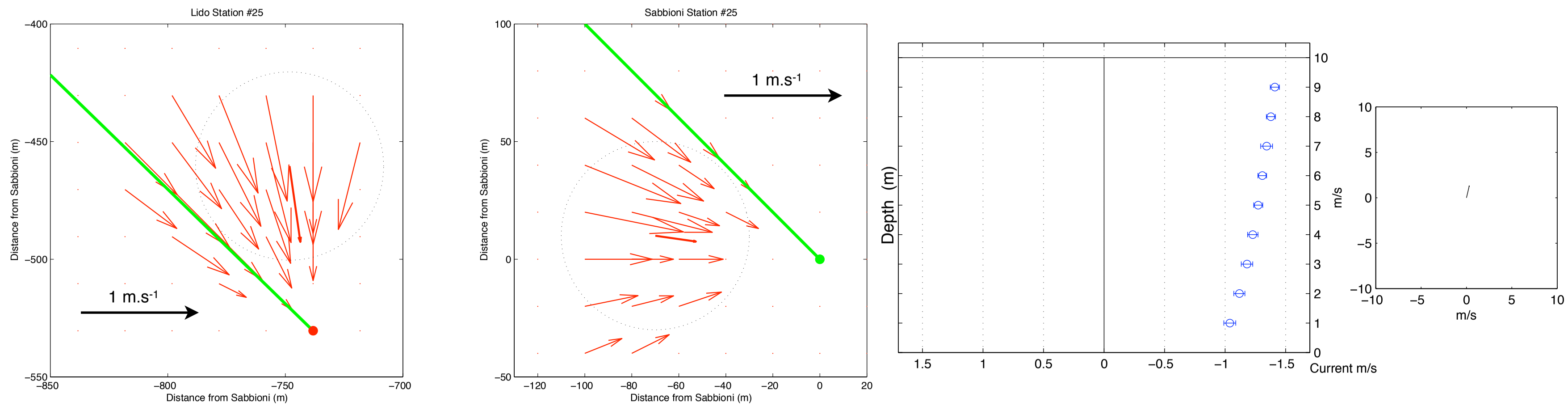

UTC 291.6666

Figure 6.3 Current Vector Map Sequence, Vertical ADCP Profile and Wind Vector Day 291.6388 - 291.6666

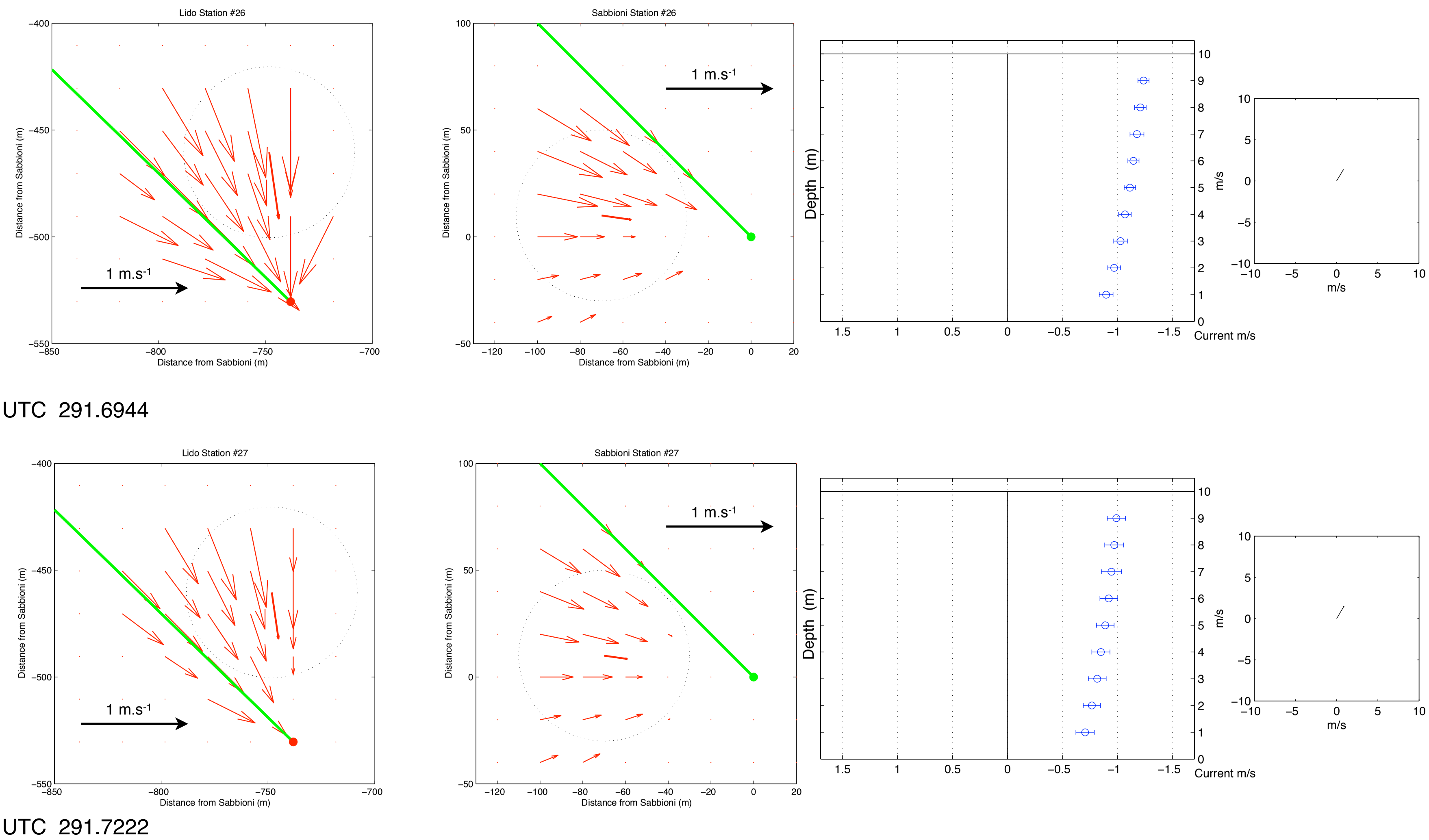

Figure 6.4 Current Vector Map Sequence, Vertical ADCP Profile and Wind Vector Day 291.6944 - 291.7222

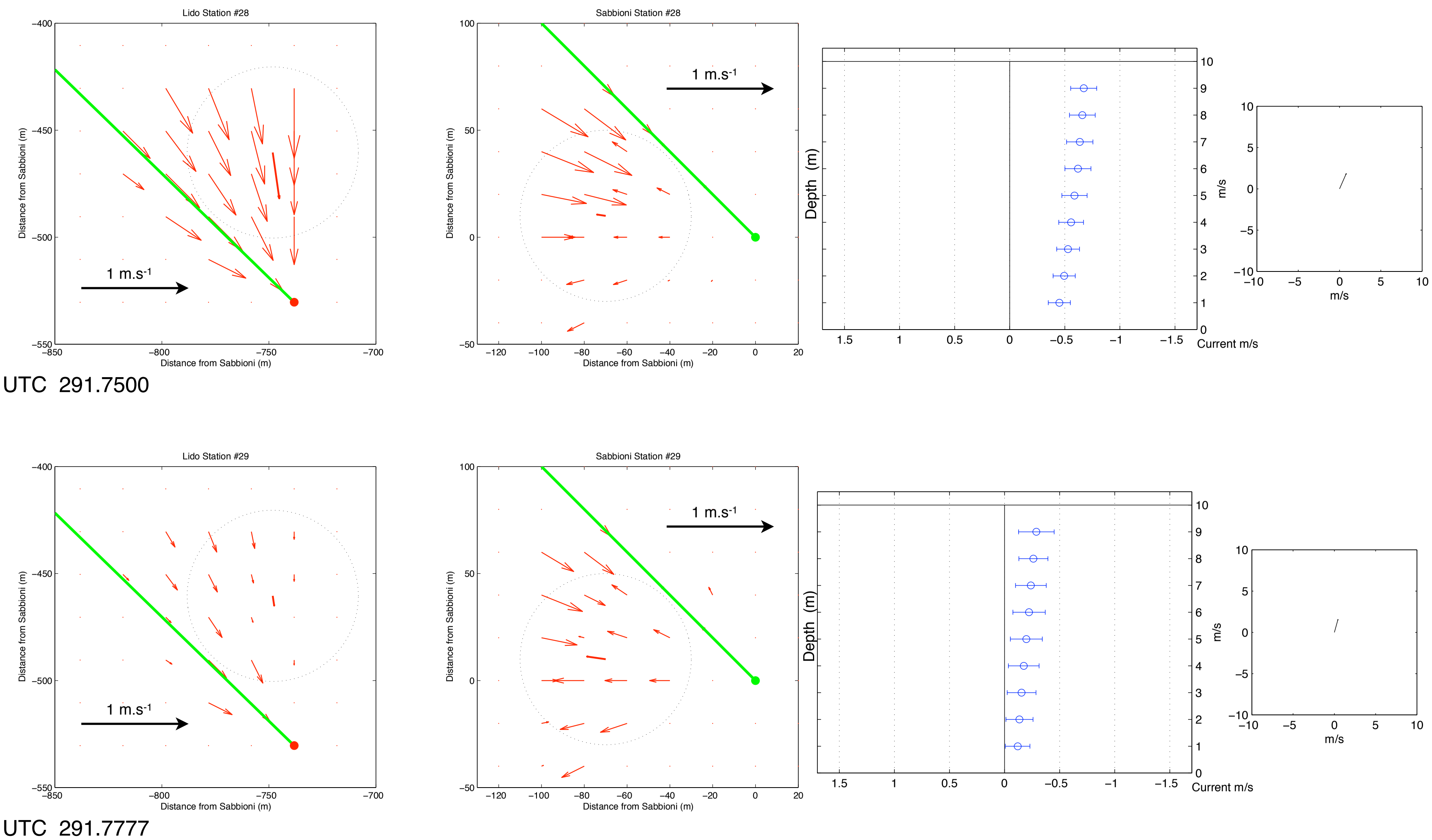

Figure 6.5 Current Vector Map Sequence, Vertical ADCP Profile and Wind Vector Day 291.7500 - 291.7777

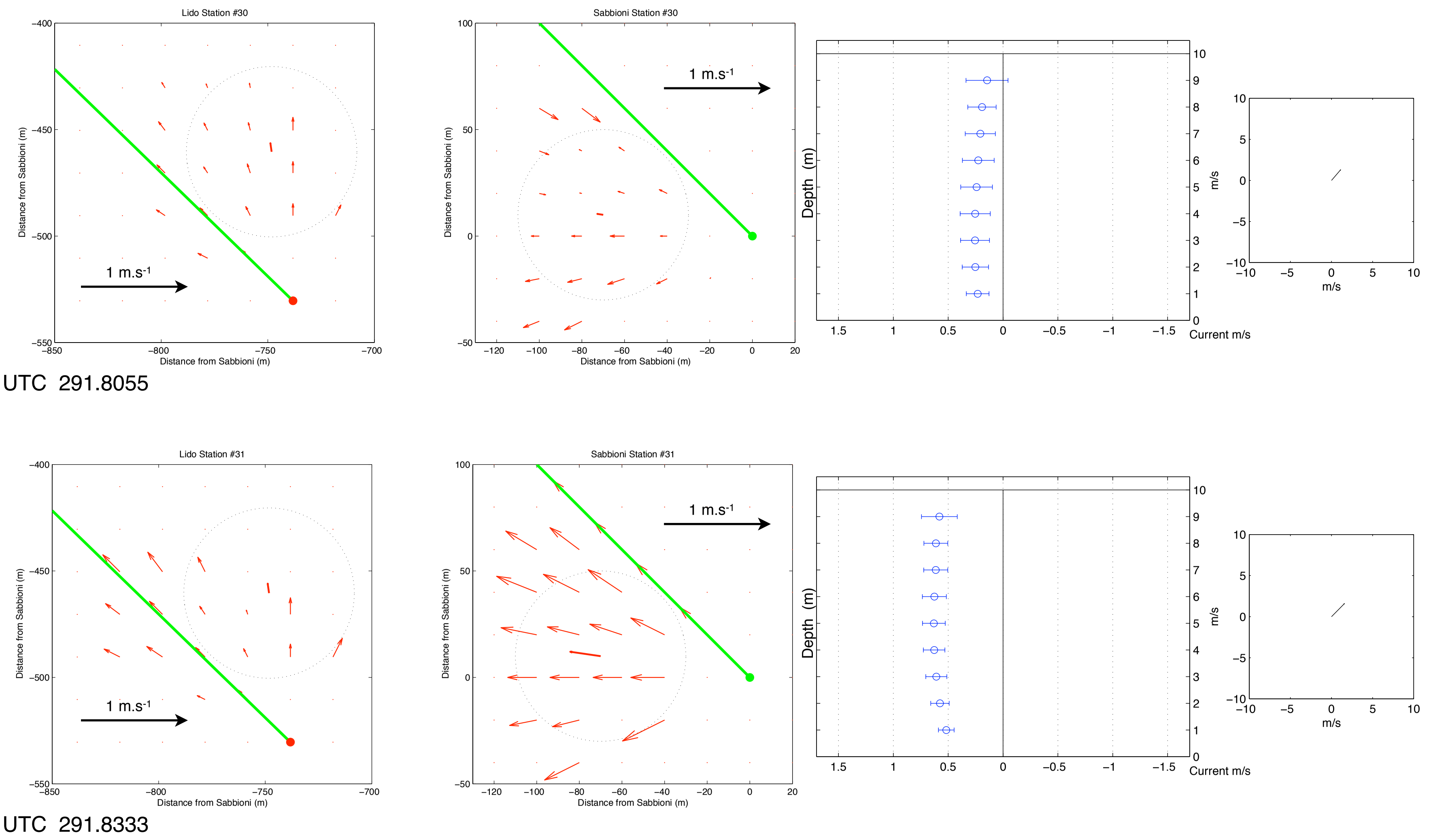

Figure 6.6 Current Vector Map Sequence, Vertical ADCP Profile and Wind Vector
Day 291.8055 - 291.8333

Another case study showing differing current regimes between the Sabbioni and Lido sides of the channel is observed in the average current time-series for Days 302 - 306 (Figure 6.7). A clear, consistent feature in the time-series from the middle of day 303 onwards is that the average current on the Sabbioni side changes from an ebb to a flood tide prior to the Lido side of the channel. The difference in tidal phase between the two sides of the channel is most pronounced on Days 305 and 306.

The current vector maps presented in Figures 6.8, 6.9, 6.10 and 6.11 are used to examine the turn of tide at the beginning of Day 306. The first plot in the sequence (Plot 306.0833) shows that the current has started to enter on the Sabbioni side of the channel, again with a front forming between the two current regimes. This front is seen to advance further up the channel in the subsequent plot (# 306.1111). From this point onwards, the current continues to flow in on the Sabbioni side of the channel yet the tidal stream continues to ebb on both the Lido side of the channel and at the ADCP location. As shown in plot 306.2500, it is not until 4 hours after the current started flowing in on the Sabbioni side of the channel that the tide reverses on the Lido side of the channel and at the ADCP. This is a very interesting current dynamic within a major shipping channel maintained by dredging, and one that has considerable implications for the transport of sediment from the neighbouring Sabbioni beach into the Venice Lagoon.

6.1.1 Conclusion

Although highly limited in range, the ability of the PortMap radar to observe these examples of fine current structure within the Lido Inlet clearly show the benefit of a high-resolution surface current radar. Of particular note is the observation of a front between the two current regimes as the inflow begins on the Sabbioni side of the channel. Observations of this kind are clearly not possible using conventional moored current meter technologies. With greater range and overlapping coverage from both stations, it would have been possible to identify the complete surface current movement of the water entering on the Sabbioni side of the inlet while the tide was still receding on the Lido side.

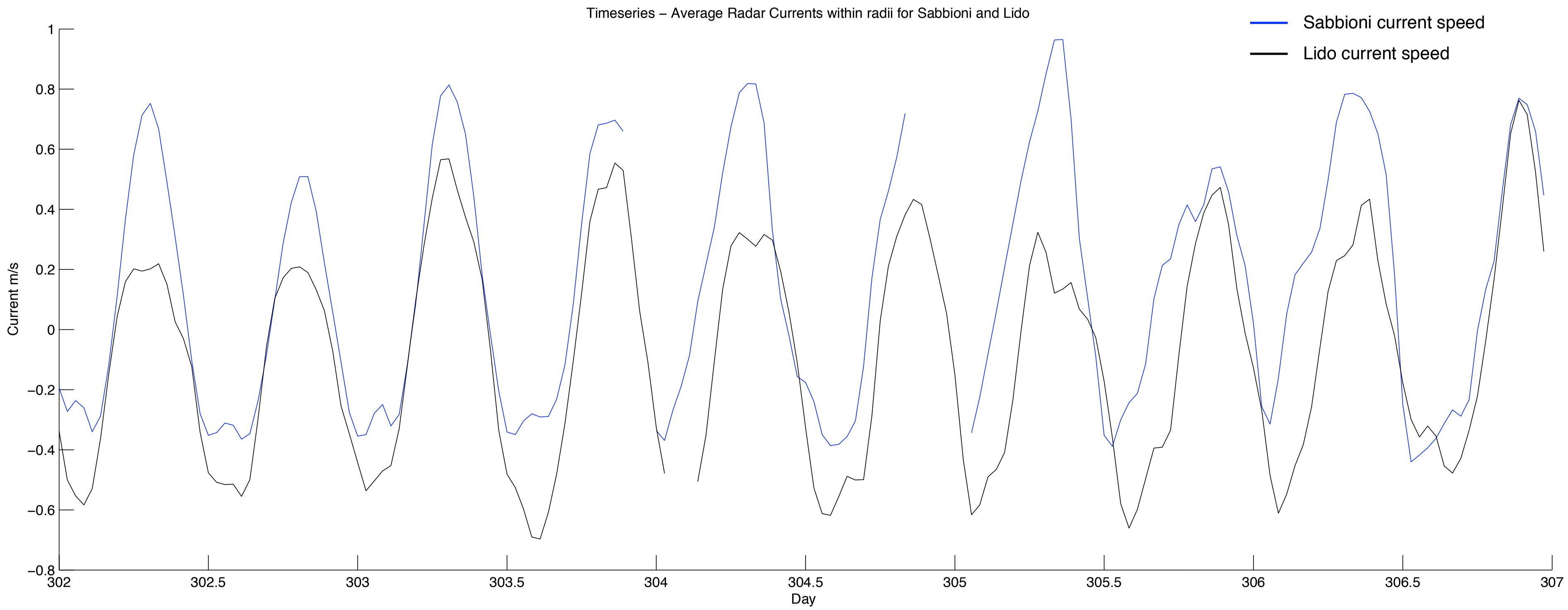

Figure 6.7 Breakwater Zone Time-series : Day 302 - 306

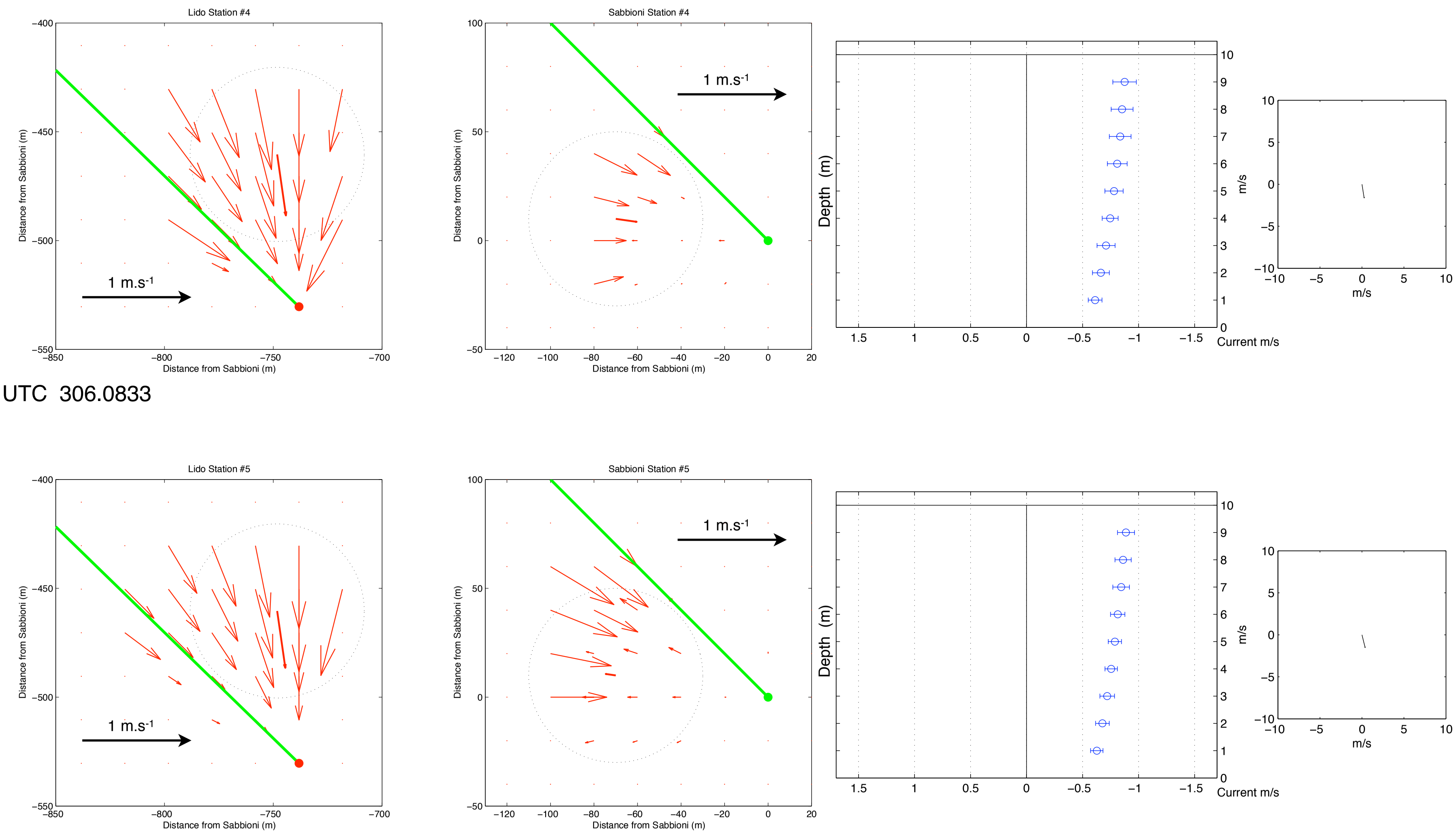

UTC 306.0833

UTC 306.1111

Figure 6.8 Current Vector Map Sequence, Vertical ADCP Profile and Wind Vector Day 306.0833 - 306.1111

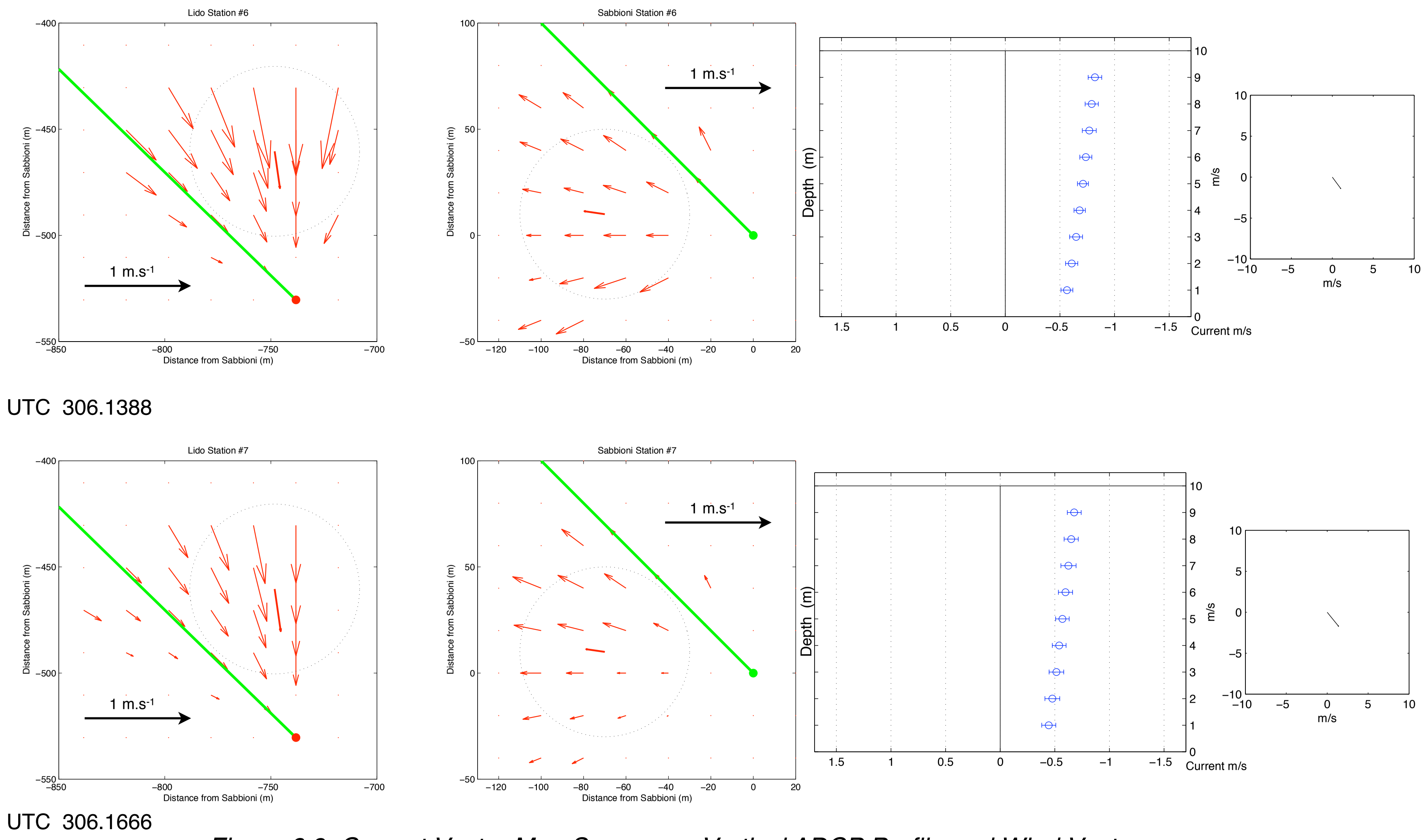

Figure 6.9 Current Vector Map Sequence, Vertical ADCP Profile and Wind Vector Day 306.1388 - 306.1666

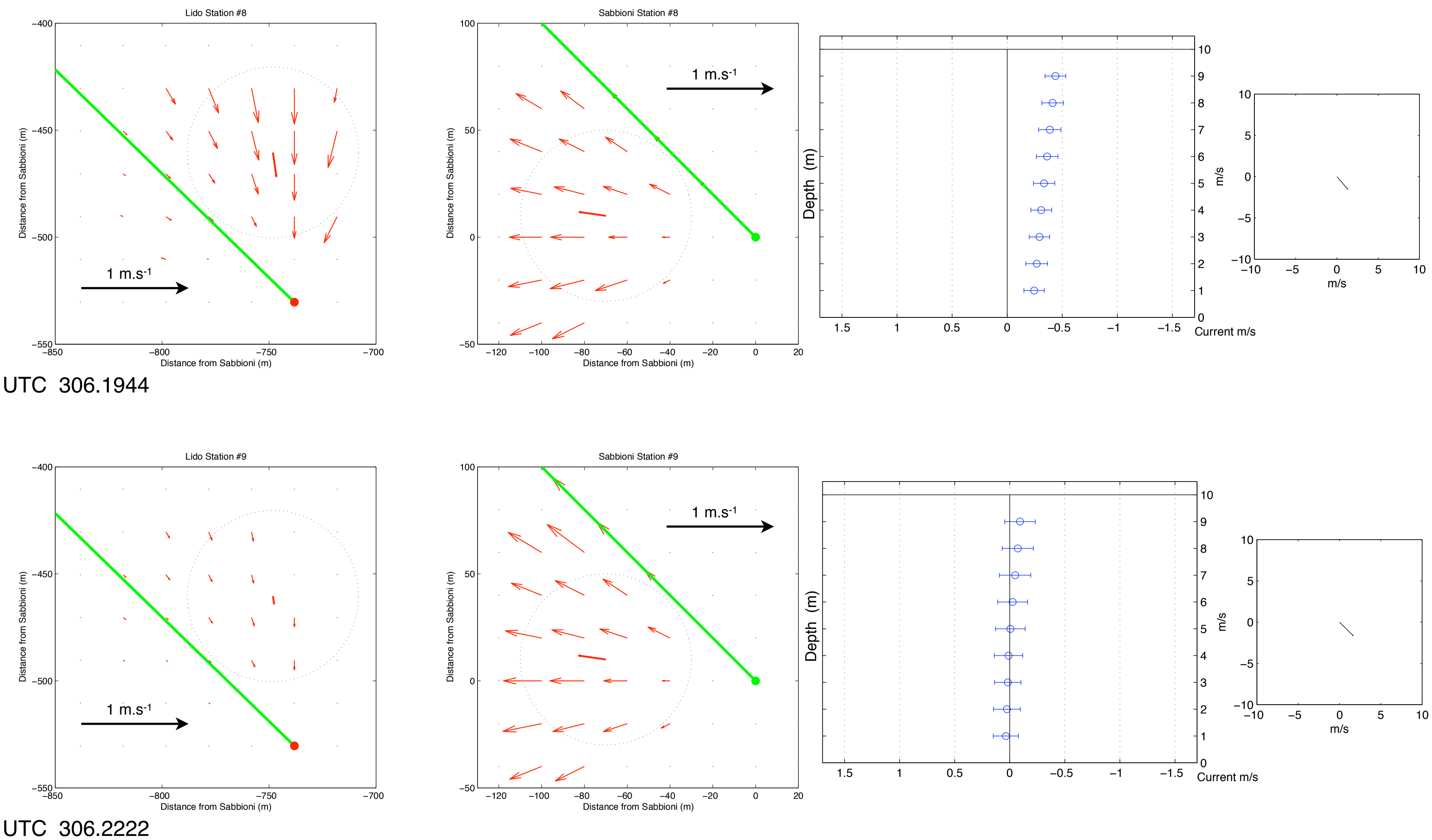

Figure 6.10 Current Vector Map Sequence, Vertical ADCP Profile and Wind Vector Day 306.1944 - 306.2222

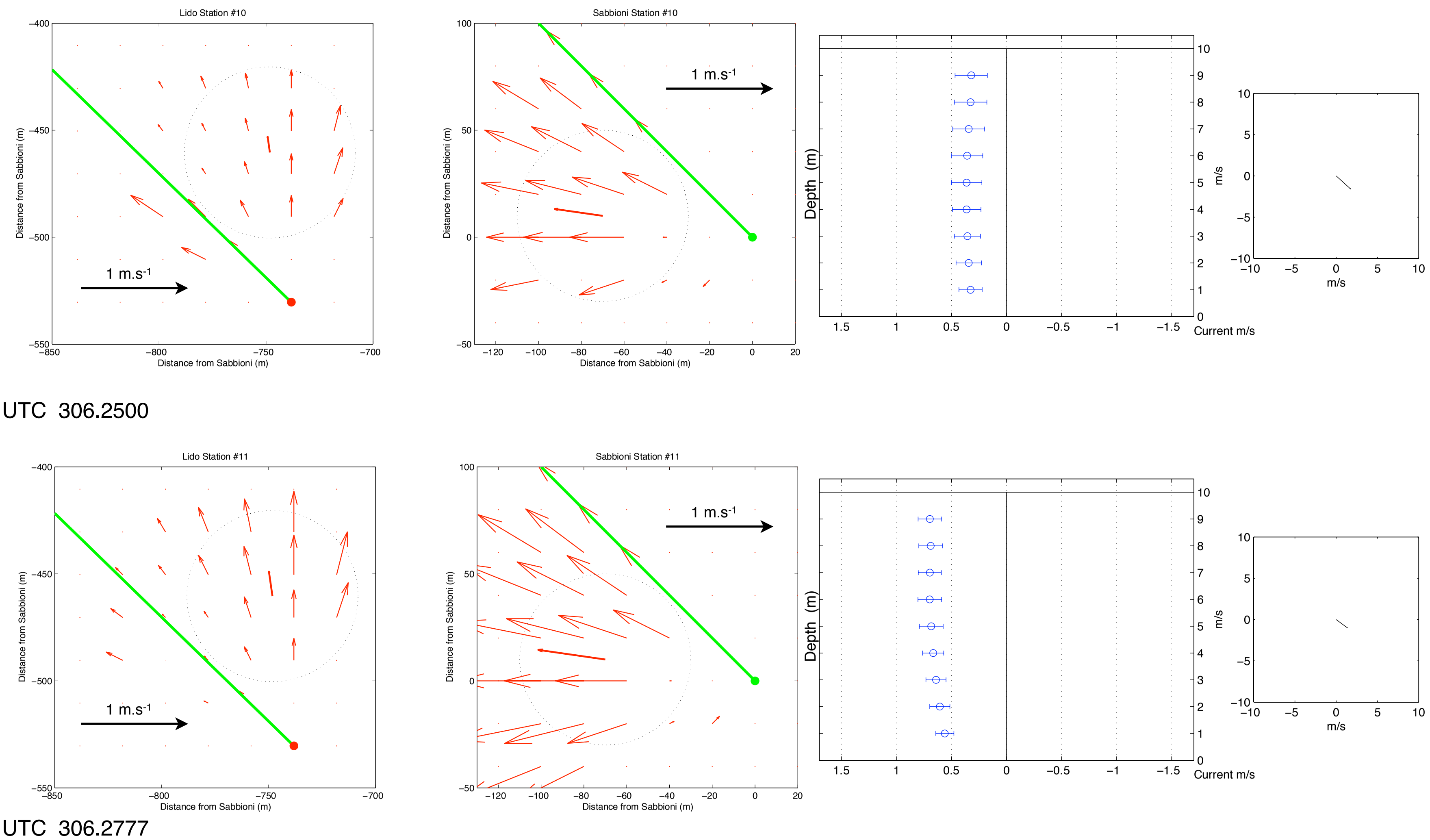

Figure 6.11 Current Vector Map Sequence, Vertical ADCP Profile and Wind Vector Day 306.2500 - 306.2777

6.2 Wave-breaking in the first range cell

During the short-range, manual direction finding process, an interesting effect was observed in the spectra and current measurements obtained from the first range cell. The spectra and measurements obtained for the first-range cell were often quite contrary to those obtained for further range cells. This is considered to be due to the effect of waves breaking against the breakwaters.

Throughout the deployment various sea-states were observed, depending on the strength and direction of the wind. If calm conditions were present (Figure 6.12 left), no waves were observed to impact on the breakwaters whereas windy and rough conditions resulted in small waves impacting on the breakwaters (Figure 6.12 right) and surging water movement around the lighthouses. Whitecaps were also present during rough conditions.

Figure 6.12 Calm and Rough conditions, as seen from Lido looking towards Sabbioni

Spectra and radial current measurements for the Lido station looking up the channel were examined at two different times on Day 294 (21-Oct-05) during outgoing tides of similar ebb tidal stream velocity. The first of these times (0205 UTC, 294.0833) corresponds to wind conditions of a moderate (12 kt / ~6 $m.s^{-1}$) breeze blowing from the North, while the latter time (1525 UTC, 294.6388) conditions were a light (4 kt / ~ 2 $m.s^{-1}$) breeze from South South-West. The tidal height and wind vector plots for these two times are highlighted in Figure 6.9 on the following page. The wind conditions for the earlier time resulted in the development of waves that impacted on the Lido breakwater.

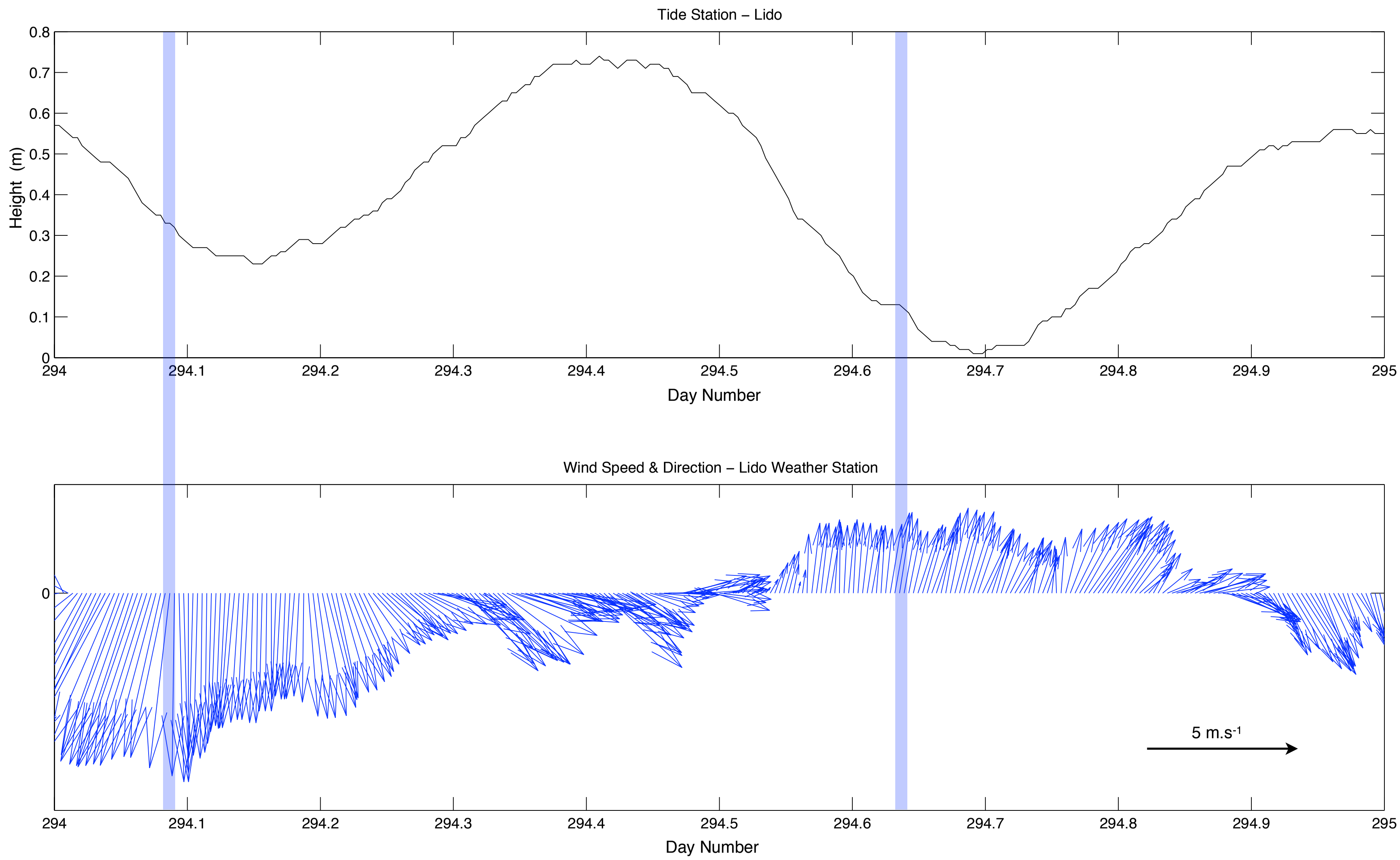

Figure 6.13 Tide and Wind - Day 294 (21-Oct-05)
(see text for highlighted times)

Looking at the spectra for the first range cell at 0205 UTC (Figure 6.14), we see that the Bragg waves are strongly Doppler shifted in the negative direction from the zero current Bragg wave positions indicated by the vertical red lines. This indicates an underlying current velocity away from the station. Also of note is the widely spread Bragg peaks. Direction finding analysis on the selected Bragg peak (enclosed box in the spectra plot) provided the radial current measurements as shown. The current direction measured is contrary to what would be expected, given the state of tide and that the ADCP record shows an outgoing channel current for Bin 9 (surface bin) of 0.68 ms^{-1} at this time.

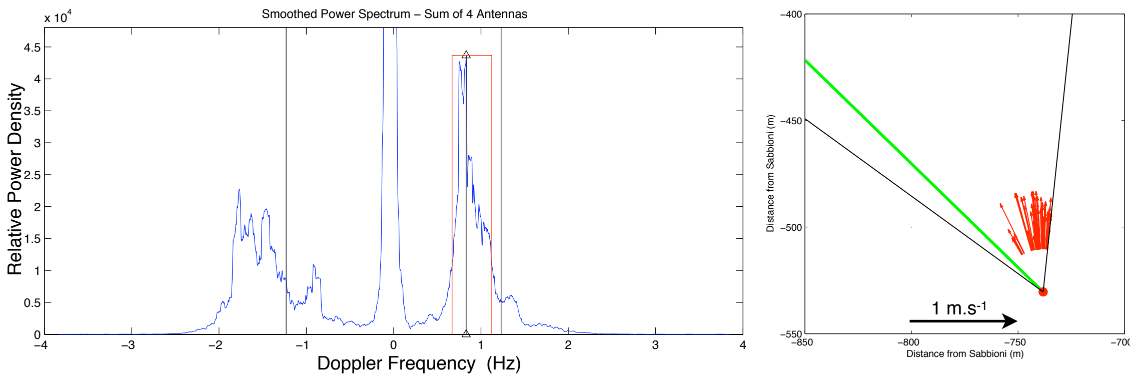

Figure 6.14 Spectra and Radials - 0205 UTC, Range 1 Lido

The spectra and radial plots for range cell 2 (Figure 6.15) shows an abrupt change to positively shifted Bragg peaks, and corresponding radial current measurements showing an outgoing tide in the channel. Given that the range resolution is 20 m, the current away from the station is only at the surrounding edge of the lighthouse breakwater.

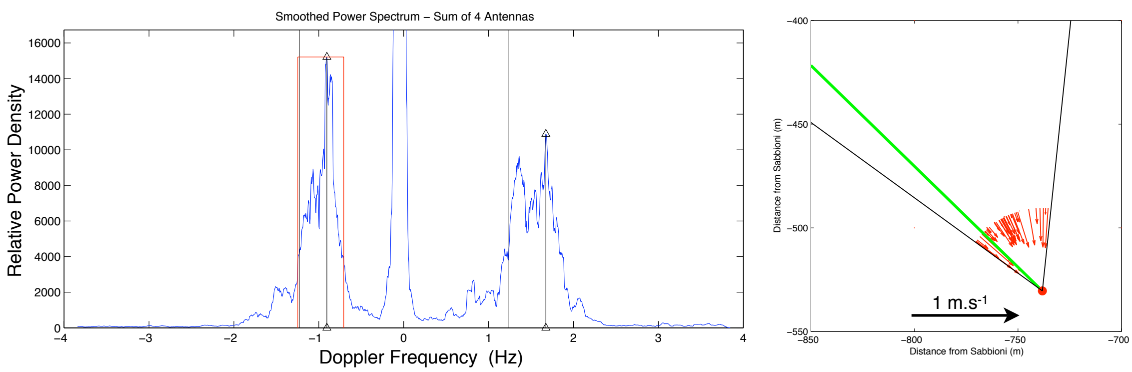

Figure 6.15 Spectra and Radial Current Measurements - 0205 UTC, Range 2 Lido

The spectra and radial plots shown in Figure 6.16 for range cell 4 further confirms that the dominant current in the channel is an outgoing tidal stream.

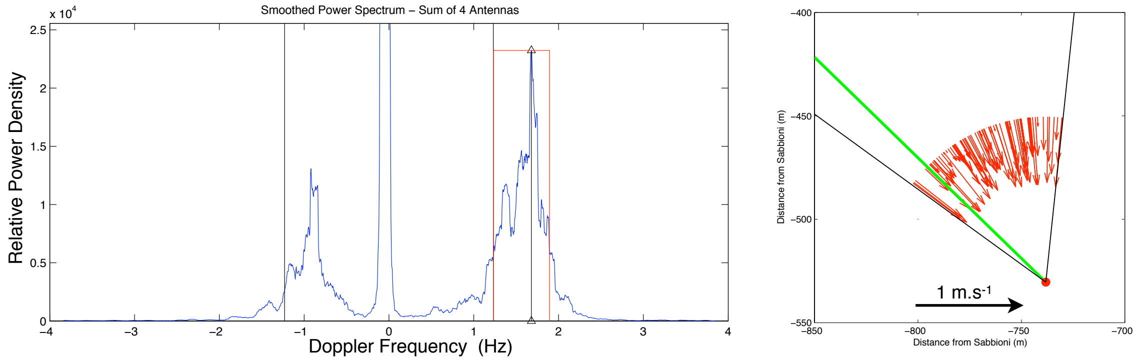

Figure 6.16 Spectra and Radial Current Measurements - 0205 UTC, Range 4

We now examine the spectra and radials obtained at 1525 UTC when a light breeze was blowing away from the Lido breakwater within the channel. Under these conditions breaking waves would not be expected to impact the northern edge of the Lido breakwater. Looking at the spectra and radials for range 1 (Figure 6.17) we see that there is much less spreading of the Bragg peak and minimal negative Doppler shift. This indicates that there is still some wave interaction with the breakwater. The spectra and radial current measurements indicate far less water movement around the breakwater though.

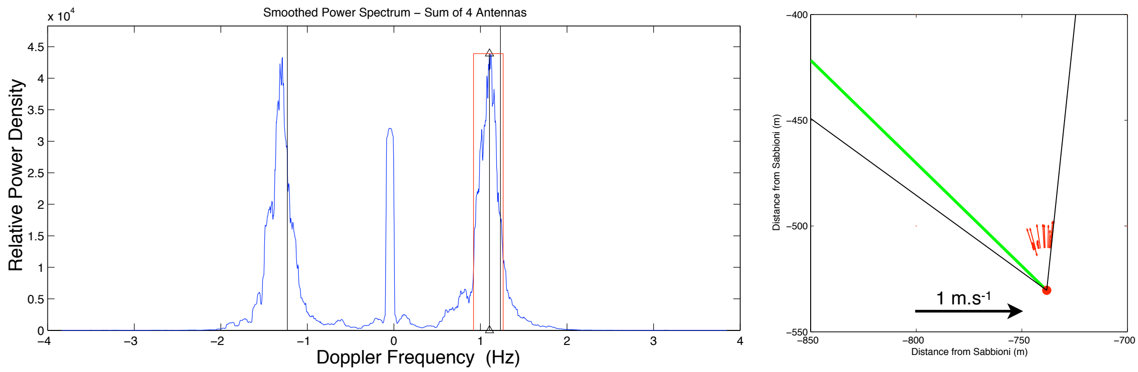

Figure 6.17 Spectra and Radial Current Measurements - 1525 UTC, Range 1

Looking at a further range also at 1525 UTC, we see that the channel current is again an outgoing tidal stream (Figure 6.18). This is confirmed by the ADCP recording (Bin 9) an outgoing 0.88 m.s^{-1} channel surface current at this time.

This effect of contrasting Doppler shift measurements between range 1 and subsequent range cells is observed depending on the prevailing wind and wave conditions in both the Sabbioni and Lido spectra and corresponding radial current measurements. It is seen most prominently during measurement periods where waves impact on the breakwaters.

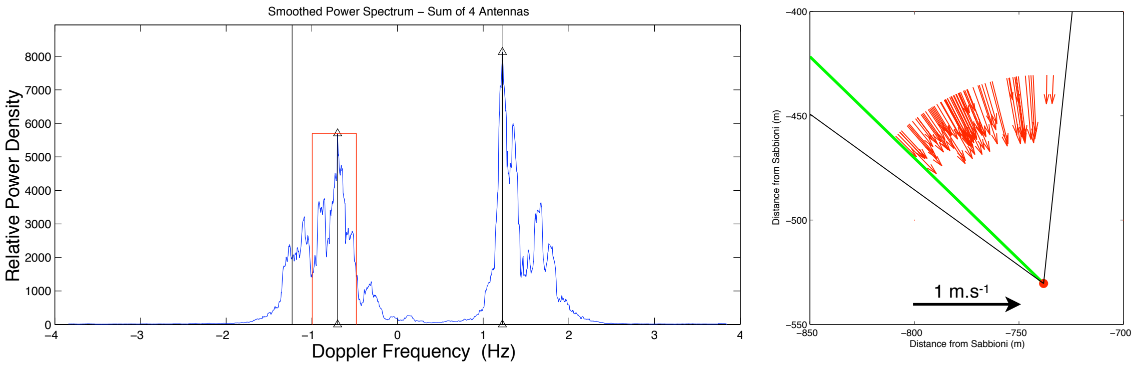

Figure 6.18 Spectra and Radial Current Measurements - 1525 UTC, Range 5

6.2.1 Conclusion

For situations with similar outgoing tidal currents, it has been shown that wind and wave conditions can strongly affect the measurements obtained at the breakwater boundary of the channel. Waves breaking on the breakwaters and subsequent backwash current is seen to strongly Doppler shift the Bragg waves. This also causes Bragg wave spreading. The Doppler shift exhibited and corresponding current measurements indicate that the current flow within this wave breaking zone to be against the general flow of the channel.

As there is such an abrupt change between the first range cell and subsequent range cells, this effect must be localised immediately at the edge of the breakwater. This is because the particularly high range resolution (20 m) exhibited by the PortMap Radar due to the system fault allows us to identify the first 20 m range cell as containing the breaking waves.

The continuous wave PortMap radar system in this instance has the advantage that there is no blind zone in front of the radar as is exhibited in pulsed radar systems. This allows the system to obtain measurements from the water immediately surrounding the lighthouse breakwater, where this breaking wave effect is observed. This observation may not have been possible with a pulsed radar system, depending on the distance that the station is from the water.

6.3 Maximum Current Velocity Limitation (0 Hz Boundary)

During the short-range, manual direction finding analysis (range resolution of 20 m), both the radar spectra and radial current measurements were seen to be adversely affected by high channel current velocities resulting in anomalous radial current readings. This effect was repeatedly observed during spring ebb tides, and was particularly prominent in the data obtained from the Lido station. Spectra and radial current measurements were analysed in detail for these conditions of high velocity flow in the channel.

The Bragg-peaks shown in Figure 6.19 were obtained at the turn of the tide and at a time of zero channel current, as recorded by the ADCP. The zero current Bragg wave positions are indicated by the black vertical lines, at +/- 1.2303 Hz.

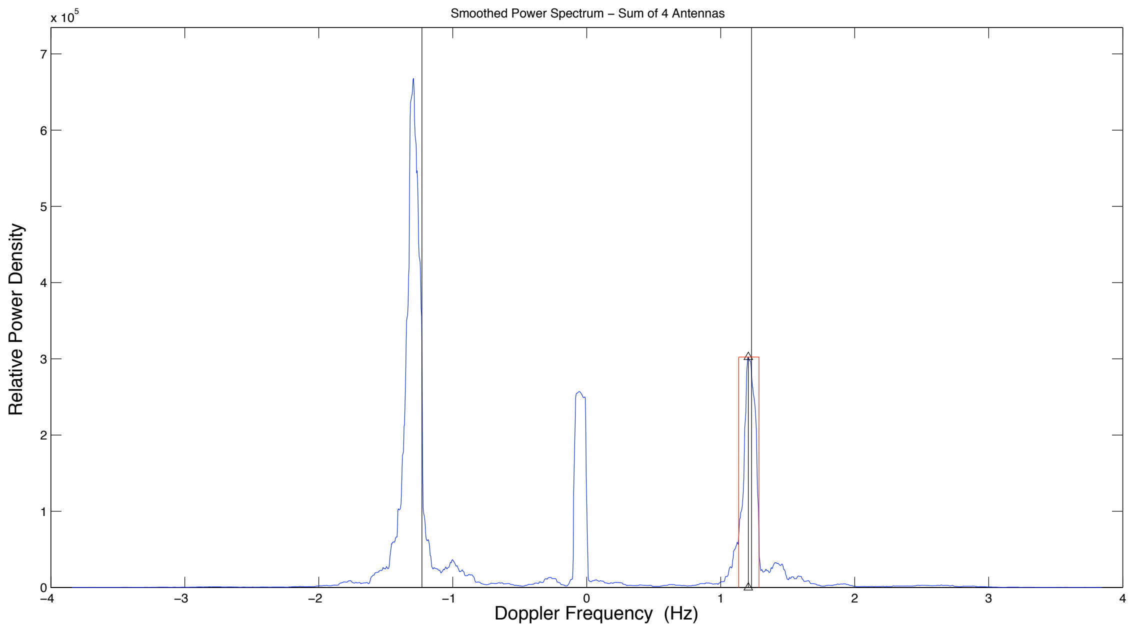

Figure 6.19 Bragg wave spectrum, Range 3 - Day 291 at 1205 h

As shown previously in Chapter 2, the Doppler shift frequency of the Bragg peaks is represented by Equation 2.7.

From this equation, the maximum surface current velocity that could be observed before one of the Bragg peaks would be theoretically Doppler shifted enough to 'cross' the 0 Hz point of the spectrum can be written as

$$v = \frac{c}{2f_0}\sqrt{\frac{gf_0}{\pi c}} \tag{6.1}$$

For the corrected operating frequency of 145.42 MHz, an absolute surface current velocity of 1.27 $m.s^{-1}$ would theoretically result in one of the Bragg peaks Doppler shifted to the 0 Hz point of the spectrum. Recorded spectra were analysed to determine the effect on the Bragg wave spectral peaks under conditions where the surface current velocity in the channel exceeds 1.27 $m.s^{-1}$.

On the 18th October, 2005 during the ebb tide from 1005 UTC until 1725 UTC local time, the ADCP surface (Bin 9) velocity measurements exceed 1.4 $m.s^{-1}$ for a period of 2 hours. A maximum 10 minute average velocity (Bin 9) of 1.602 $m.s^{-1}$ was recorded at 1302 UTC. Using the short-range direction finding analysis presented, radar spectra and corresponding radial current measurements obtained by the Lido station were analysed for this period. Spectra for range cell 3 were obtained every 40 minutes looking up the channel. Spectra with corresponding radial current maps, together with the average ADCP profile for each 40 minute period are plotted in Figures 6.20 through 6.25 on the following pages.

In Figures 6.20 and 6.21, we see that as the surface current velocity increases toward the station, the Bragg wave is increasingly Doppler shifted in the positive direction. Also of note is the increased spreading of the Bragg wave peaks with increasing current velocity. At zero current, the Bragg wave peaks are narrow and very well defined. At greater velocities, the Bragg waves are widely spread with multiple peaks. For these plots, we also note that the Bragg peaks on the negative half of the spectra are greater in magnitude than the positive Bragg peaks. The radial current measurements obtained using direction finding on these spectra also correspond well with the ADCP profile shown.

The ADCP profiles in Figures 6.22 and 6.23 show that the current in the channel continues to increase with the outgoing tide to a maximum Bin 9 average velocity of 1.5 ms^{-1}. Under these conditions of high channel current velocity, the spectra for plots 291.5278, 291.5556 and 291.5833 show the presence of a strong positive Bragg wave peak that is in close proximity to the zero current, Bragg wave position. As indicated by the enclosed red boxes, this strong peak is selected by the direction finding algorithm and used to obtain the radial current measurements. The resultant radial current plots are clearly anomalous to the results obtained by the ADCP.

In the sequence shown, when the channel current is below 1.4 $m.s^{-1}$ the dominant Bragg peak is in the negative half of the spectrum, corresponding to ocean Bragg waves travelling radially away from the radar station. In the presence of high channel current velocities, it is of particular interest that an energetic peak appears on the positive half of the spectrum. This strong positive Bragg peak corresponds to an ocean Bragg wave travelling toward the radar station. This is in the same direction as the outgoing tide, and corresponding radial current velocities. The cause of this effect on the spectra under these conditions is not yet understood. The presence of these energetic peaks is not attributable to noise sources, and re-occurs under similar conditions.

Once the ADCP measured current velocity decreases to 1.25 $m.s^{-1}$ the spectra and corresponding radial current measurements again depict reasonable measurement results. In Figure 6.25, Plot 291.7222 we see that once the current velocity returns to zero again, narrow, well-defined Bragg peaks are present in the spectra. This is in strong contrast to the spectra observed under conditions of high current velocity.

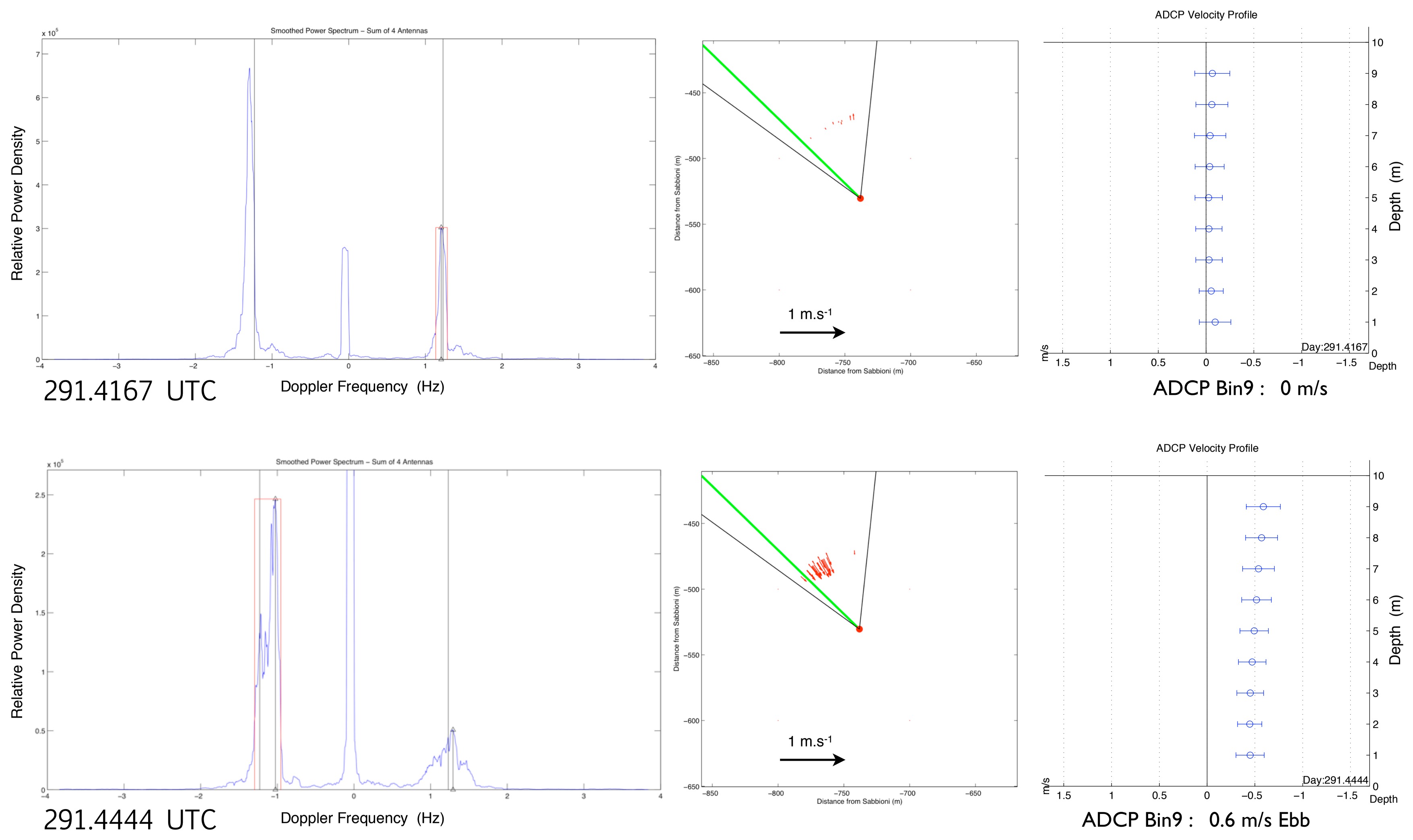

Figure 6.20 Radar Spectra, Radial Currents and ADCP Profiles Day 291.4167 - 291.4444 UTC

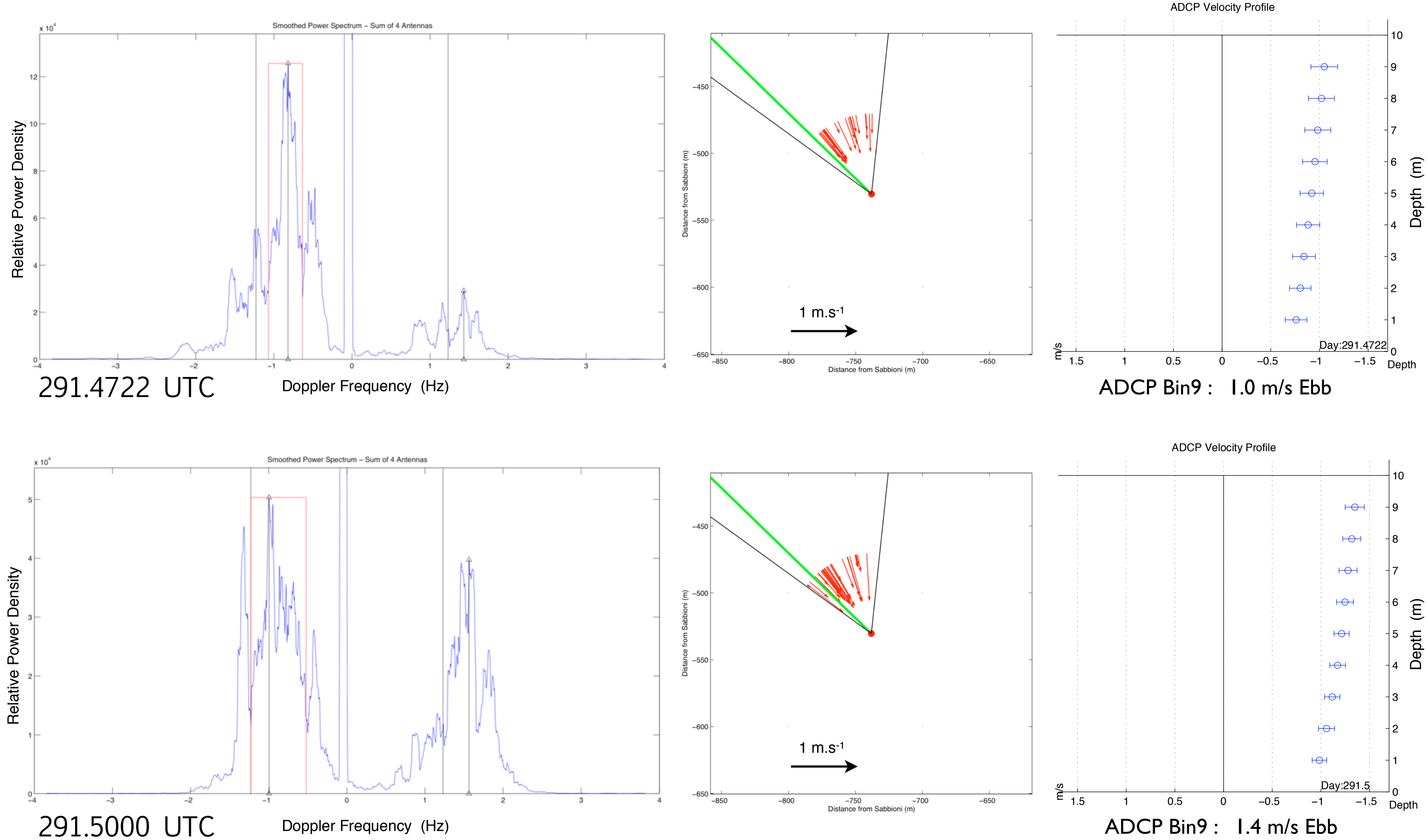

Figure 6.21 Radar Spectra, Radial Currents and ADCP Profiles Day 291.4722 - 291.5000 UTC

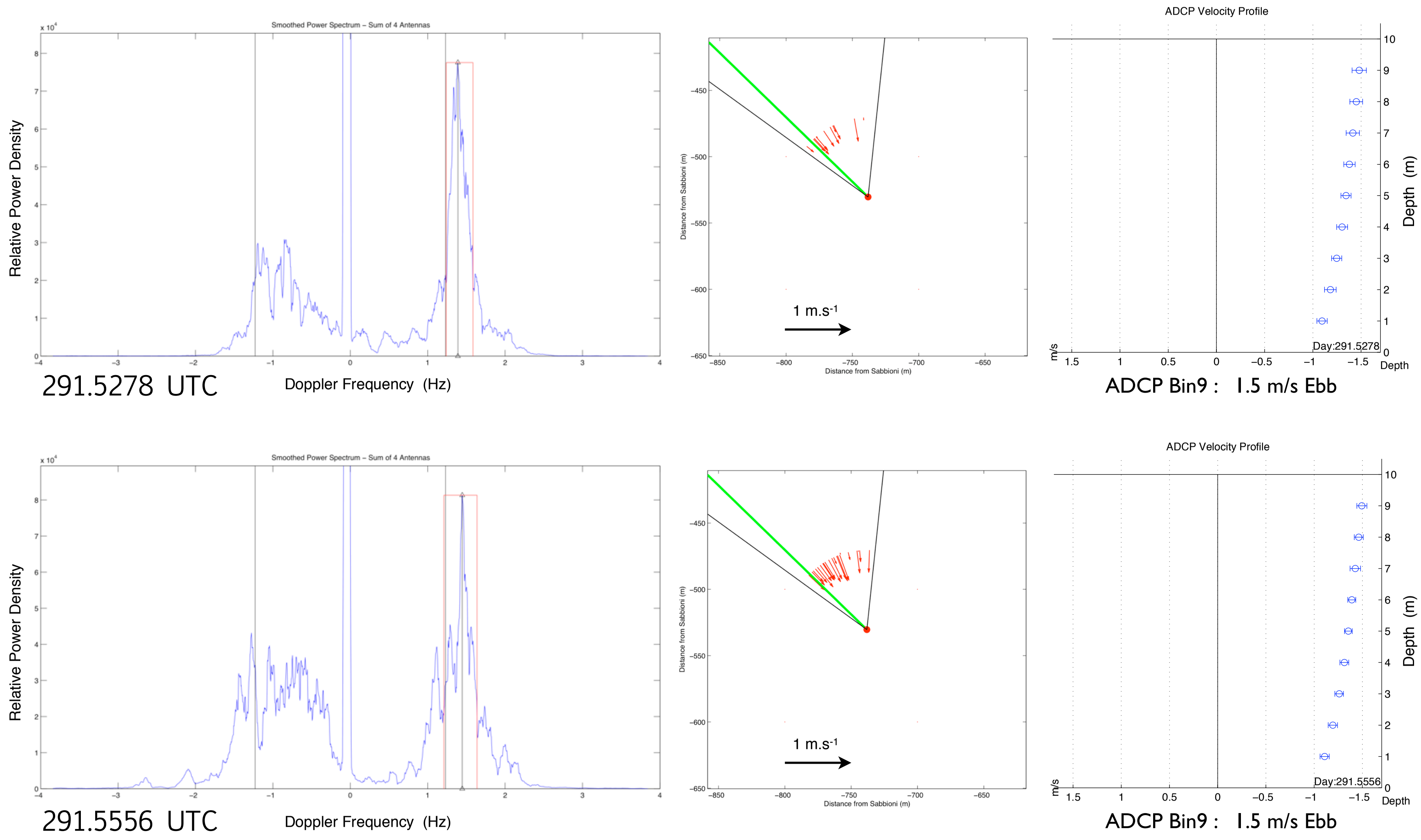

Figure 6.22 Radar Spectra, Radial Currents and ADCP Profiles Day 291.5278 - 291.5556 UTC

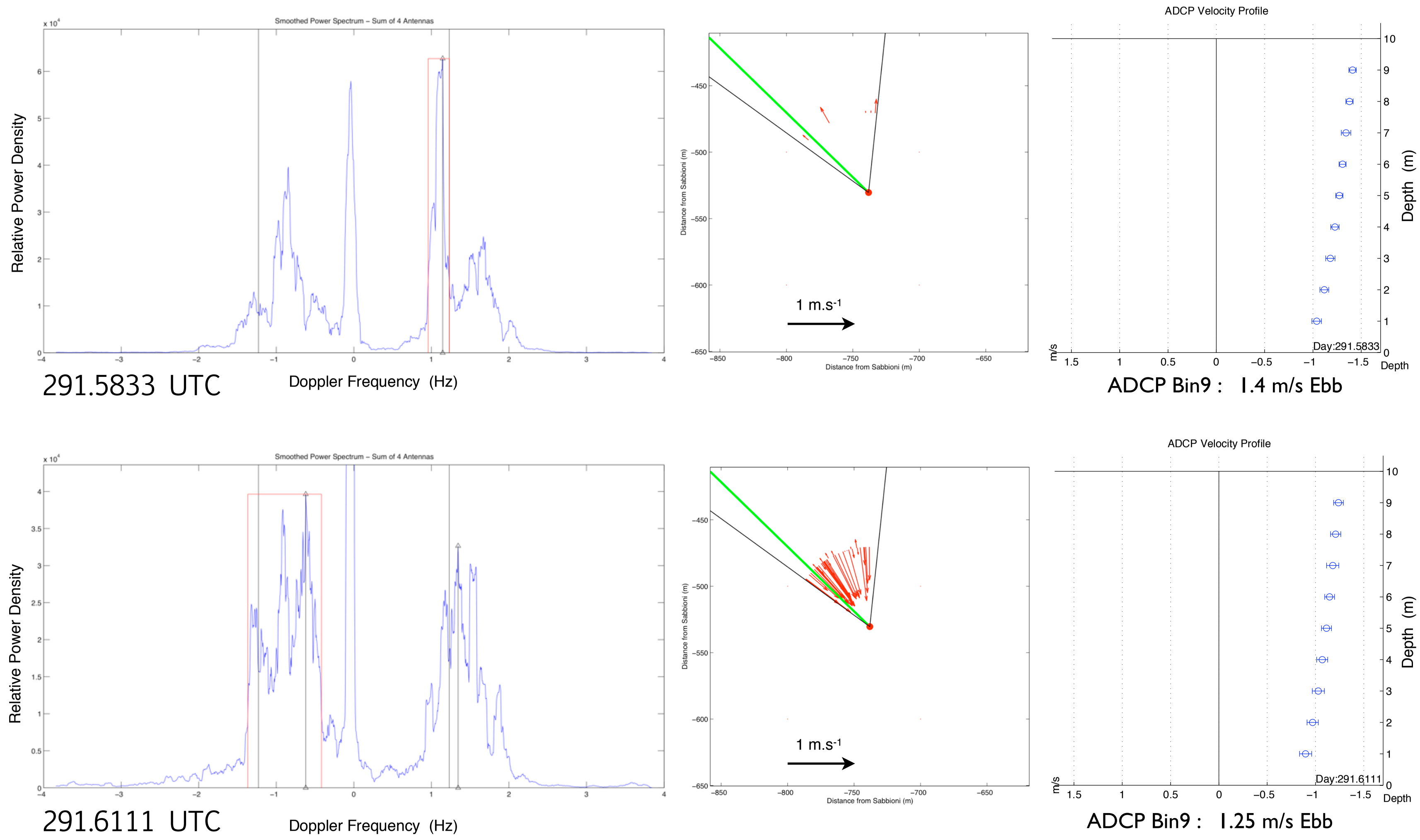

Figure 6.23 Radar Spectra, Radial Currents and ADCP Profiles
Day 291.5833 - 291.6111 UTC

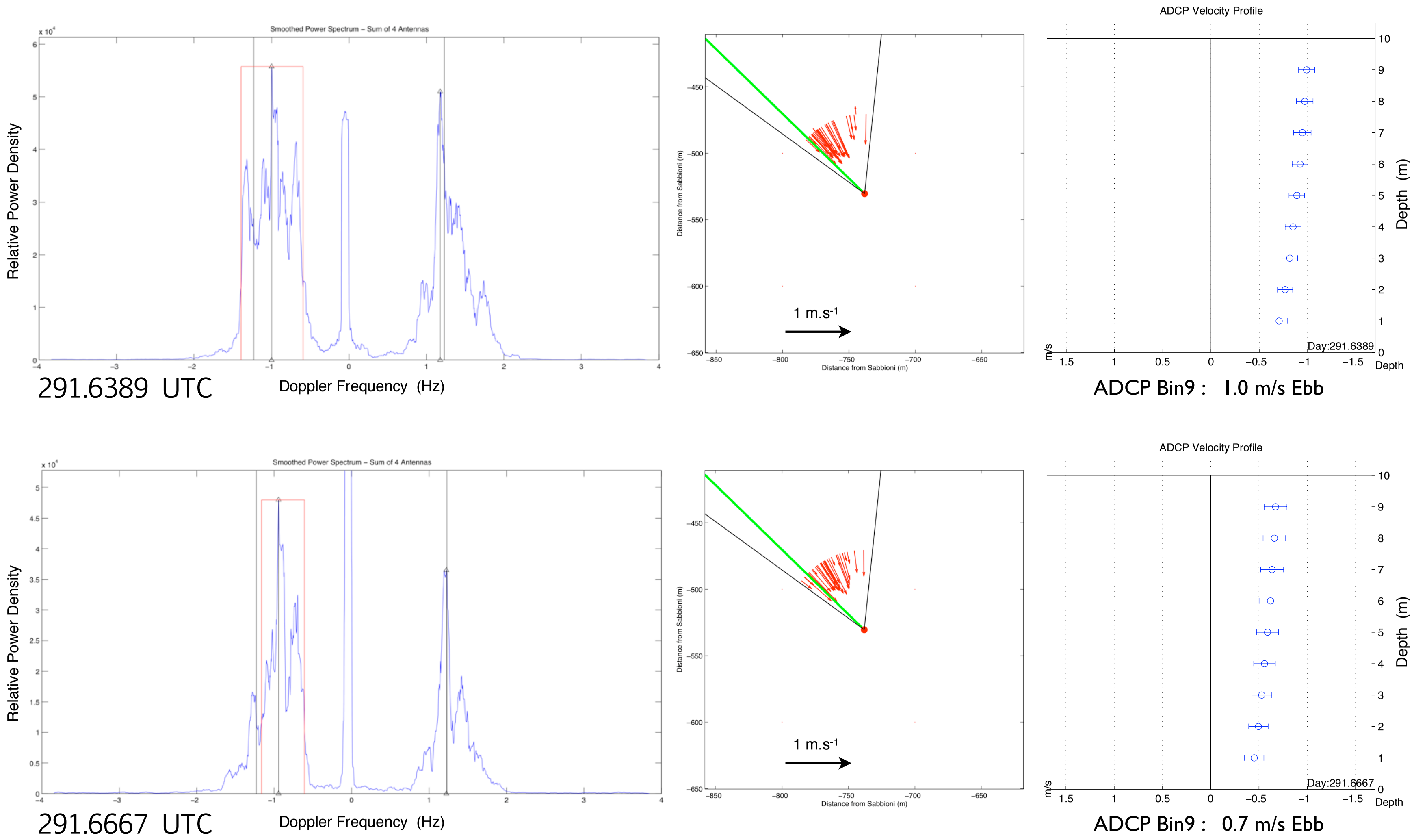

Figure 6.24 Radar Spectra, Radial Currents and ADCP Profiles
Day 291.6389 - 291.6667 UTC

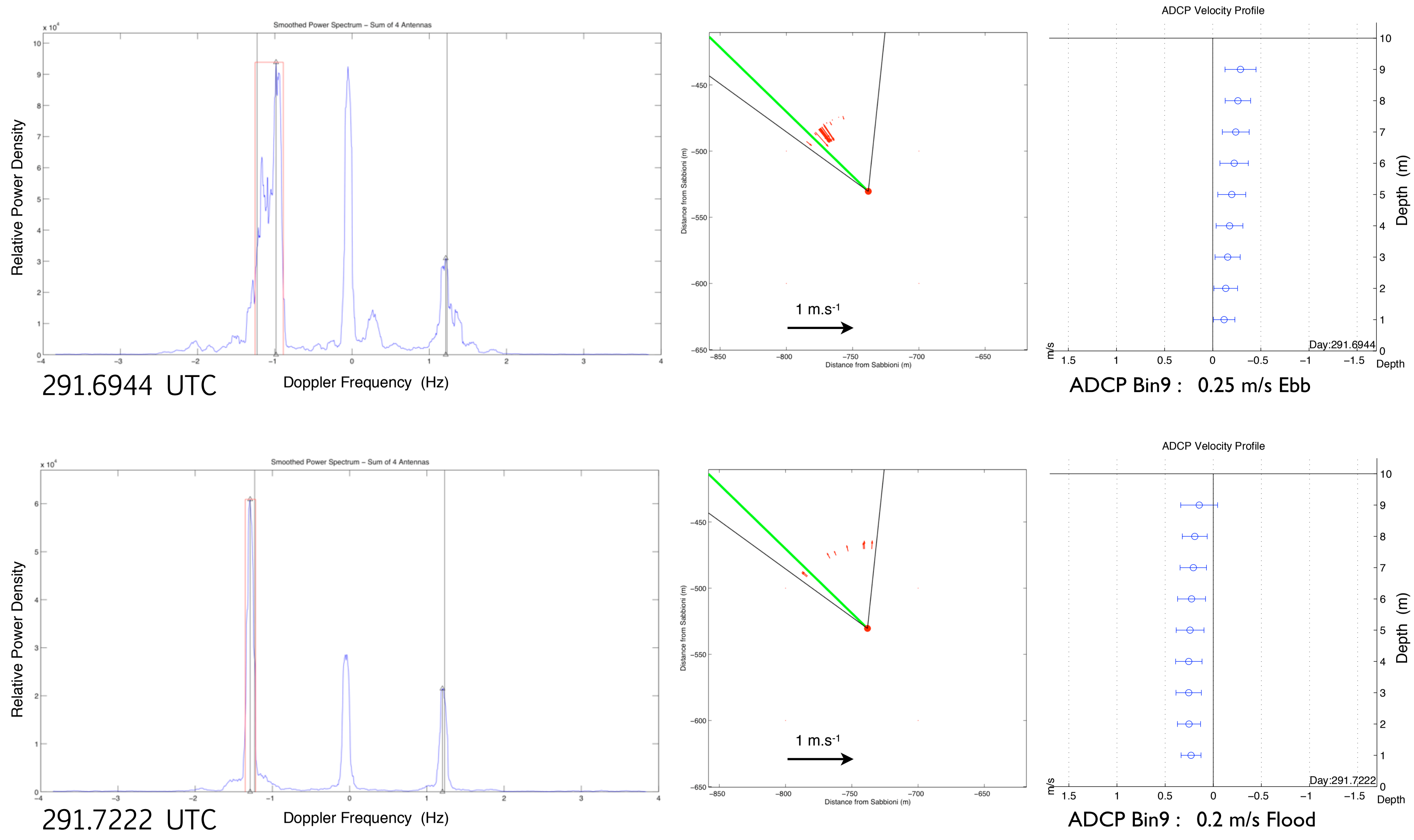

Figure 6.25 Radar Spectra, Radial Currents and ADCP Profiles
Day 291.6944 - 291.7222 UTC

6.3.1 Conclusion

This observation has obvious implications for the use of the PortMap radar and all VHF Ocean Surface Current Radars in situations where high current velocities are to be observed. It has been shown that PortMap system measurements become unreliable where the radial surface current velocity exceeds a velocity of 1.27 $m.s^{-1}$.

The effect on the PortMap radar of radial current velocities beyond 1.27 $m.s^{-1}$ certainly needs to observed and understood further. An analysis technique may also be needed to detect conditions that are beyond the measurable velocity range for the PortMap system.

7 Conclusions

The PortMap Ocean Surface Current Radar was deployed to monitor the current dynamics within the Lido Inlet to the Venice Lagoon, Italy. Data were also provided by the Italian partner organisations from a fixed ADCP within the channel, tide gauges, and weather stations. Techniques were developed to extract both primary current data from radar spectra, and to produce secondary current data that would be suitable for evaluating mass transport through the inlet.

7.1 Data Analysis Results

The PortMap radar systems used in Venice produced data that were generally of a very poor signal-to-noise ratio. Using a false range resolution of 100 m, the usable range of the system was indicated to be 300 - 500 m which was greatly reduced from the expected range of 2 km. The techniques to generate secondary current data for both a region surrounding the ADCP location, and for points along a transect of the channel were developed using data having a false range resolution of 100 m. The results obtained using these techniques were therefore invalid, although the techniques are sound.

The surface current measurements obtained using the radar were generally lower in velocity than those recorded by the fixed ADCP deployed in the channel, while the false radar spatial scale was used. Initially this under-reporting by the radar was thought to be a result of noisy spectral data, as spectral peaks caused by internal interference were observed in the recorded spectra. To improve the current measurement results, new analysis software, 'DFind' was developed to detect and ignore spectral peaks affected by this internal interference. This was effective in reducing the noise in the average current time-series and improved the correlation of the false radar measurements with ADCP measurements.

After the majority of data analysis had taken place with the range resolution of the system understood to be 100 m, the manufacturer of the PortMap system reported a fault that caused the effective range resolution to be 20 m. This resulted in a further decrease in the range of the system by a factor of 5. This meant that the currents thought to be measured at the ADCP site were in fact near to the side walls of the channel, and absolves us from having to explain the discrepancies between radar and ADCP measured currents. One would expect currents to be reduced by friction at the side walls. The 'DFind' algorithm was altered to use this modified range resolution. High resolution, short-range current vector maps were then successfully produced for the regions surrounding each radar station.

7.2 Discussion Highlights

During the deployment, a turbid water plume was observed entering on the Sabbioni side of the inlet while the tide continued to ebb on the Lido side of the inlet. Under certain conditions, the wave re-suspension zone along the Cavallino beach to the north of the inlet was seen to extend up to and beyond the Sabbioni lighthouse breakwater. Under these conditions, turbid water drawn from this region flows into the channel. High resolution vector current maps that were produced using radar measurements with a range resolution of 20 m were sufficient to observe this interesting current dynamic. These vector current maps show that during an outgoing tide with a strong ebb tidal stream on the Lido side of the channel, water begins to flow into the channel on the Sabbioni side of the channel. This current dynamic has obvious implications for the transport of sediment from the neighbouring Cavallino beach into the inlet, and into the Venice Lagoon.

Another interesting feature observed during the analysis of short-range vector current maps was the detection in the first range cell of backwash currents from impacting waves along the breakwater. It was shown that these currents were prominent in stronger wind conditions blowing waves onto the breakwater but minimal where wind conditions were more benign. This feature was only ever observed in the first 20 m range cell from the radar. This is a serendipitous outcome from the manufacturing fault because it would not have been observed with the design-condition of 100 m range cells.

While investigating the cause of the radar system consistently reporting lower surface currents, it was considered that velocities could exist that would theoretically result in a Bragg wave reaching or crossing the 0 Hz position in the Bragg spectrum. It was shown that for the system operating on 145.42 MHz, this would occur at radial surface current velocities greater than 1.27 $m.s^{-1}$. Radar spectra and corresponding surface current measurements were analysed during a period where the surface current in the Lido channel exceeded 1.4 $m.s^{-1}$ for a duration of 2 hours. Although the Bragg peaks are not seen to cross the 0 Hz point on the spectrum at high current velocities, a strong Bragg peak is seen to form close to the zero current Bragg peak locations. Under these conditions, this would appear as a valid Bragg peak from which incorrect current measurements would be obtained.

7.3 Further Investigation

The research presented has developed methods to produce the current measurements required to calculate mass transport through a coastal inlet. Techniques have been presented to overcome interference sources in radar data, to reduce the noise in time-series current velocity measurements and to produce average current measurements along an Inlet transect. Also developed is a method of producing three dimensional transect profiles using a combination of surface current measurements obtained by the PortMap radar and vertical current profiles produced by an ADCP deployed on the seabed.

The use of a PortMap radar system performing to specification is required to acquire surface current measurements that adequately cover a coastal inlet. The techniques presented in this research could be used and further developed to fully evaluate the mass transport through a coastal inlet using combined measurement technologies. These techniques are valid even though the data from the radar had a scaling fault, which makes conclusions from this part of the work invalid.

Further investigation is also required to determine the effect of high current velocities on the spectra and measurements obtained by the PortMap radar. Although it has been shown that an anomalous Bragg peak forms close to the zero current Bragg wave positions under high current conditions, this needs to be better understood. Although this event was seen a number of times in the data, additional data with stronger signals showing this effect would be of benefit.

Bibliography

Apell, G. F., Bass, P.D., and Metcalf, M.A. (1991) Acoustic Doppler Current Profiler Performance in Near Surface and Bottom Boundaries. *IEEE Journal of Oceanic Engineering,* 16**,** 390-396.

Barrick, D. E. (1972) Remote sensing of sea state by radar, in V. Derr (ed.). *Remote Sensing of the Troposphere,* Chapter 12.

Barrick, D. E. (1972) First-Order Theory and Analysis of MF/HF/VHF Scatter from the Sea. *IEEE Transactions on Antennas and Propagation,* AP-20**,** 2-10.

Barrick, D. E., Evans, M. W. and Weber, B. L. (1977) Ocean surface currents mapped by radar. *Science,* 198**,** 138-144.

Cheng, R. T. and Gartner, J. W. (2003) Complete velocity distribution in river cross-sections measured by acoustic instruments. *Current Measurement Technology, 2003. Proceedings of the IEEE/OES Seventh Working Conference on.*

Crombie, D. D. (1955) Doppler spectrum of sea echo at 13.56 Mc/s. *Nature,* 175**,** 681-682.

Dessurealt, J. G., Belliveau, D.J. and Young, S. W. (1991) Design and tests of a trawl-resistant package for an Acoustic Doppler Current Profiler. *IEEE Journal of Oceanic Engineering,* 16**,** 397-401.

Dyer, K. R. (1986) *Coastal and estuarine sediment dynamics,* New York, Wiley.

Emery, B. M., Washburn, L. and Harlan, J. A. (2004) Evaluating Radial Current Measurements from CODAR High-Frequency Radars with Moored Current Meters. *Journal of Atmospheric and Oceanic Technology,* 21**,** 1259-1272.

Fernandez, D. M., Vesecky, J. F. and Teague, C. C. (1996) Measurements of upper ocean surface current shear with high-frequency radar. *Journal of Geophysical Research,* 101**,** 28615-28625.

Gacic, M., Mosquer, I. M., Kovacevic, V., Mazzoldi, A., Cardin, V., Arena, F. and Gelsi, G. (2004) Temporal variations of water flow between the Venetian Lagoon and the open sea. *Journal of Marine Systems,* 51**,** 33-47.

Gacic, M., V. Kovacevic, I., Mancero Mosquer, Mazzoldi, A. and Cosoli., S. (2005) *Water Fluxes between the Venice Lagoon and the Adriatic Sea*.

Graber, H. C., Haus, B.K., Chapman, R.D. and Shay, L. K. (1997) HF Radar comparisons with moored estimates of current speed and direction: Expected differences and implications. *Journal of Geophysical Research,* 102**,** 18749-18766.

Gurgel, K. W., Essen, H.H. and Kingsley, S. P. (1999) High-frequency radars: physical limitations and recent developments. *Coastal Engineering,* 37**,** 201-218.

Gurgel, K. W., Antonischki, G., Essen, H. H., and Schlick, T. (1999) Wellen Radar (WERA): a new ground-wave HF radar for ocean remote sensing. *Coastal Engineering,* 37**,** 219-234.

Heron, M. L. (1985) Line Broadening of HF ocean surface radar backscatter spectra. *Journal of Oceanic Engineering,* 10**,** 397-401.

Heron, M. L., and Heron, S. F. (2001) Cumulative probability noise analysis in geophysical spectral records. *International Journal of Remote Sensing,* 22**,** 2537 - 2544.

Heron, M. L., and Prytz, A. (2003) Ocean Surface Radar Current Measurements in the surf break zone at Coffs Harbour. *Coasts & Ports Australiasian Conference 2003.*

Howarth, M. J., Harrison, A.J., Knight, P.J. and Player, R. J. J. (1995) Measurement of net flow through a channel. *Current Measurement, 1995. Proceedings of the IEEE Fifth Working Conference on.*

Knight, P. J. and Howarth, M. J. (1999) The flow through the North Channel of the Irish sea. *Continental Shelf Research,* 19**,** 693-716.

Kostaschuk, R., Best, J., Villard, P., Peakall, J. and Franklin, M. (2005) Measuring flow velocity and sediment transport with an acoustic doppler current profiler. *Geomorphology,* 68**,** 25-37.

Lane, A., Knight, P.J. and Player, R. J. (1999) Current measurement technology for near-shore waters. *Coastal Engineering,* 37**,** 343-368.

Lee, T. N., and Smith, N. (2002) Volume transport variability through the Florida Keys tidal channels. *Continental Shelf Research,* 22**,** 1361-1377.

Lu, Y., and Lueck, R. G. (1999) Using a broadband ADCP in a tidal channel. Part I: Mean flow and shear. *Journal of Atmospheric and Oceanic Technology,* 16**,** 1556-1568.

Lueck, R. G. and Lu, Y. (1997) The Logarithmic Layer in a Tidal Channel. *Continental Shelf Research,* 17**,** 1785-1801.

Muste, M., Yu, K., Pratt, T., A. and Abraham, D. (2004) Practical aspects of ADCP data use for quantification of mean river flow characteristics; Part II: fixed-vessel measurements. *Flow Measurement and Instrumentation,* 15**,** 17-28.

Paduan, J. D., and Rosenfeld, L. K. (1996) Remotely sensed surface currents in Monteray Bay from shore-based HF radar (CODAR). *Journal of Geophysical Research,* 101**,** 20669-20686.

Pickard, G. L., and Emery, W. J. (1990) *Descriptive physical oceanography : an introduction,* New York, Pergamon Press.

Rdinstruments (1996) ADCP: Principles of Operation - A Practical Primer. R.D. Instruments.

Rowe, F. and Young, J. (1979) An ocean current profiler using Doppler sonar. *Oceans '79 Proceedings*.

Rowsell, R. D., and Skafel, M. G. (2002) Comparison of current meters in a coastal environment. *Oceans 2002 MTS/IEEE Proceedings.*

Schott, E. (1989) Measuring winds from underneath the ocean surface by upward looking Acoustic Doppler Current Profilers. *Journal of Geophysical Research,* 94**,** 8313-8321.

Smith, N. P. (2002) Tidal, low-frequency and long-term mean transport through two channels in the Florida Keys. *Continental Shelf Research,* 22**,** 1643-1650.

Soulsby, R. L. (1983) *The bottom boundary layer in shelf seas,* Amsterdam, Elsevier.

Stewart, R. H., and Joy, J. W. (1974) HF Radio measurement of surface currents. *Deep Sea Research,* 21**,** 1039-1049.

Tang, C. L. and Belliveau, D. J. (1994) Vertical structure of currents on the northern Grand Bank - a view from a bottom mounted Acoustic Doppler Current Profiler. *Continental Shelf Research,* 14**,** 1331-1347.

Teague, C. C., J.F. Vesecky, A. and Hallock, Z. R. (2001) A comparison of multifrequency HF radar and ADCP measurements of near-surface currents during COPE-3. *IEEE Journal of Oceanic Engineering,* 26**,** 399-405.

Vesecky, J. F., Teague, C.C., Daida, J.M., Fernandez, D.M., Onstott, R.G., Hansen, P., Laws, K. and Plume, M. A. (1998) Observations of currents from the near-surface to 50 m depth using a new multifrequency HF radar and an ADCP located in the radar observational area. *Geoscience and Remote Sensing Symposium Proceedings, 1998. IGARSS '98, 1998 IEEE International.*

Visbeck, M., and Fischer, J. (1995) Sea Surface conditions remotely sensed by upward looking Acoustic Doppler Current Profilers. *Journal of Atmospheric and Oceanic Technology,* 12**,** 141-149.

Wewetzer, S. F. K., Duck, R.W. and Anderson, J. M. (1999) Acoustic Doppler Current Profiler measurements in coastal and estuarine environments: examples from the Tay Estuary, Scotland. *Geomorphology,* 29**,** 21-30.

Yanagi, T. (1999) *Coastal oceanography,* Boston, Kluwer Academic Publishers.

Zedel, L., Gordon, L., and Crawford, G. (1995) Wind direction from an upward looking ADCP. *Current Measurement, 1995. Proceedings of the IEEE Fifth Working Conference on.*